Progress in the ITER Physics Basis

Chapter 4. Power and Particle Control

A. Loarte (EFDA-CSU Garching), B. Lipschultz (MIT-PSFC), A.S. Kukushkin (ITER-IT), G.F. Matthews (UKAEA), P.C. Stangeby (UTIAS), N. Asakura (JAERI), G.F. Counsell (UKAEA), G. Federici (ITER-IT), A. Kallenbach (IPP-Garching), K. Krieger (IPP-Garching), A. Mahdavi (GA), V. Philipps (IPP-FZ Jülich), D. Reiter (IPP-FZ Jülich), J. Roth (IPP-Garching), J. Strachan (PPPL), D. Whyte (U. Wisconsin-Madison), R. Doerner (UCSD-PISCES-B), T. Eich (IPP-Garching), W. Fundamenski (UKAEA), A. Herrmann (IPP-Garching), M. Fenstermacher (LLNL), P. Ghendrih (CEA-Cadarache), M. Groth (LLNL), A. Kirschner (IPP-FZ Jülich), S. Konoshima (JAERI), B. LaBombard (MIT-PSFC), P. Lang (IPP-Garching), A.W. Leonard (GA), P. Monier-Garbet (CEA-Cadarache), R. Neu (IPP-Garching), H. Pacher (INRS-EMT), R. Pegourie (CEA-Cadarache), R.A. Pitts (CRPP), S. Takamura (U. Nagoya), J. Terry (MIT-PSFC), E. Tsitrone (CEA-Cadarache) and the ITPA Scrape-off Layer and Divertor Physics Topical Group

Abstract.

Progress, since the ITER Physics Basis publication, in understanding the processes that will determine the properties of the plasma edge and its interaction with material elements in ITER is described. Experimental areas where significant progress has taken place are : energy transport in the SOL in particular of the anomalous transport scaling, particle transport in the SOL that plays a major role in the interaction of diverted plasmas with the main chamber material elements, ELM energy deposition on material elements and the transport mechanism for the ELM energy from the main plasma to the plasma facing components, the physics of plasma detachment and neutral dynamics including the edge density profile structure and the control of plasma particle content and He removal, the erosion of low and high Z materials in fusion devices, their transport to the core plasma and their migration at the plasma edge including the formation of mixed materials, the processes determining the size and location of the retention of tritium in fusion devices and methods to remove it and the processes determining the efficiency of the various fuelling methods as well as their development towards the ITER requirements. This experimental progress has been accompanied by the development of modelling tools for the physical processes at the edge plasma and plasma-materials interaction and the further validation of these models by comparing their predictions with the new experimental results. Progress in the modelling development and validation has been mostly concentrated in the following areas : refinement of the predictions for ITER with plasma edge modelling codes by inclusion of detailed geometrical features of the divertor and the introduction of physical effects, which can play a

major role in determining the divertor parameters at the divertor for ITER conditions such as hydrogen radiation transport and neutral-neutral collisions, modelling of the ion orbits at the plasma edge, which can play a role in determining power deposition at the divertor target, models for plasma-materials and plasma dynamics interaction during ELMs and disruptions, models for the transport of impurities at the plasma edge to describe the core contamination by impurities and the migration of eroded materials at the edge plasma and its associated tritium retention and models for the turbulent processes that determine the anomalous transport of energy and particles across the SOL. The implications for the expected performance of the reference regimes in ITER, the operation of the ITER device and the lifetime of the plasma facing materials are discussed.

4.1. Introduction.

This chapter outlines the significant progress achieved since the ITER Physics Basis in understanding basic scrape-off layer (SOL) and divertor processes in a tokamak. The interaction of plasma with first-wall surfaces will have considerable impact on the performance of fusion plasmas, the lifetime of plasma facing components, and the retention of tritium in next step Burning Plasma Experiments (such as ITER).

Next BPX experiments, such as ITER, will have larger steady power fluxes onto divertor and main chamber surfaces. Together with the longer pulses, this can cause a significantly larger erosion of these components than in present experiments both during steady-state plasma conditions and, particularly, during ELMs and disruptions.

The steady state heat fluxes to divertor plates are now a commonplace measurement. The recognition and analysis of the effect of loosely-bound layers on the measurement has been a substantial accomplishment. The continued accumulation of data on the magnitude and profile of divertor power flow has allowed better cross-tokamak databases of such data to be accumulated and analyzed. The resulting scalings (Section 4.2.1) have improved along with the comparable modelling (Section 4.3.2).

At the time of the IPB, it was generally thought that the divertor was the primary area of concern for PFC erosion and, hence, lifetime. However, in the intervening period, it has been shown that time-averaged radial transport of particles can compete with parallel transport resulting in significant main chamber ion fluxes in current devices, which are linked to impurity sources. Studies of radial transport, both on macroscopic (time-averaged) and microscopic (turbulence) level (see Section 4.2.1) have been pursued. In general it is perceived that these steady state particle fluxes are not a significant concern for first-wall lifetime, although the database of information is still fairly limited. In parallel there has been significant progress in the modelling of the underlying processes (see Section 4.3.7).

It has been recognized that SOL flows play a central role in a number of transport processes (e.g. material migration and divertor asymmetries). In the period since the IPB the

range of measurements has been greatly expanded poloidally (see Section 4.2.1). The pattern of parallel flow has been shown to be similar across many tokamaks, with flow Mach number magnitudes in the range 0.5-1 well away from the divertor target. The models of such flows (See Section 4.3.3) have improved significantly, coming much closer to matching experimental measurements. The inclusion of drifts and poloidal variations in radial transport appear to be the key to this match.

Energy deposition during transient events (ELMs and disruptions) is an even more important threat to the lifetime of PFC components. The magnitude, time and spatial characteristics of the energy flux to the plasma facing components are much better characterized since the IPB (see Section 4.2.2). The transport mechanisms that deliver energy from the core plasma to the plasma facing components during these events have been studied both experimentally (Section 4.2.2) and through modelling (Section 4.3.3) with models for the process appearing to be reasonably successful. In particular, some analogies between the transient fluxes of energy to the main chamber walls during ELMs and that of particles during steady phases (turbulent bursts) have been identified, not foreseen in the IPB, which are now being modelled with the same sophisticated codes described in Section 4.3.7.

A potentially significant restriction to next step BPXs operability could be caused by the long-term retention of tritium inside the vacuum vessel exceeding site limits. Summarised in Section 4.2.6 are the results of new studies on this subject. The retention of tritium has been shown to be linked with co-deposition of carbon, which occurs preferentially at the inner divertor. The magnitude and location of the retained tritium is influenced by the mode of operation of the device (plasma regime, background wall temperature), divertor geometry characteristics and fine details of the divertor target construction (gaps, shadows, etc.) and plasma flows. Tritium cleaning techniques (Section 4.2.6) have been developed based on photonic illumination of the tritium co-deposits, oxidation of the co-deposits, and various RF conditioning techniques.

The problem of tritium retention is, hence, closely linked to that of global material migration in tokamaks, which has been the subject of intense experimental and modelling research since the IPB both in devices with low-Z and high-Z plasma facing components. The main wall and in most cases, the outer divertor (for ion $B \times \nabla B$ drift towards the dominant divertor), have been identified as zones of erosion while net deposition occurs at the inner divertor. Two major effects have been identified to play a major role in determining the observed migration pattern: strong SOL flows, which can preferentially direct the main chamber eroded material towards the inner or outer divertor (depending on the direction of the field) and local divertor conditions which affect the local erosion/redeposition balance. This is still a very active field of research, as quantitative extrapolation of present results to ITER is very complex. Section 4.2.4 thus summarises the recent and on-going attempts to determine the migration of material in tokamaks in a quantitative way, while Section 4.3.6 describes the

improvements in the modelling of impurity transport at the plasma edge, which has been carried out to describe the experimental measurements.

The issue of tritium retention and maintaining high purity core plasmas over a large range of experimental conditions led to the current choice of plasma facing materials covering the PFCs in ITER as described in the IPB. Since this choice was made, a number of new physics phenomena have been identified/quantified (e.g. main chamber fluxes, co-deposition…). This knowledge has engendered a substantial research effort to explore the implications of these phenomena for the ITER material choice and on the device operability (see Section 4.2.5). Significant progress has been achieved in understanding the erosion rates of carbon PFCs in the conditions expected at the ITER divertor plasma, indicating that it may be significantly smaller than that observed in present devices, with the associated decrease in expected tritium retention. The interaction of the plasma with the main chamber walls in steady-state and transient conditions, which has been found to be significant in present devices, has triggered a re-evaluation of the consequences for main chamber PFC lifetime and operability of ITER with a Be wall, which is still on-going. The formation of mixed materials in ITER (C/Be/W) and the consequences for T retention and machine operability have been studied in a quantitative way, with indication of both positive (Be coverage of the C target, decreasing the retention of tritium) and negative implications (retention of tritium in C/O Be layers, etc.) for ITER operation. These are all described in Section 4.2.5 and remain to be precisely quantified for ITER conditions. Finally, there has been a positive experience in the operation of divertor devices with high Z PFCs while maintaining an acceptable level of core plasma purity. In particular it has been shown that ECRH and ICRH can be used as control actuators to avoid such accumulation under particular conditions (Section 4.2.5).

Last but not least, the control of neutral species in tokamaks and the development of fuelling methods have experienced significant advances since the IPB, as described in Sections 4.2.3 and 4.2.7. The geometry of the divertor has proven a very effective tool for the control of the neutral pressure at the divertor and the control of the hydrogenic and helium content of the main plasma. Present estimates indicate that the requirements for particle control and helium removal for successful operation can very likely be achieved in ITER. Furthermore, achievement of neutral densities and collisionalities near that predicted for ITER has allowed the initial steps to validate edge plasma-neutral modelling codes (see Sections 4.2.3 and 4.3.2.5) with respect to physical phenomena such as recombination, Ly_α radiation trapping and neutral-neutral collisions. Such processes are expected to play a major role in determining the neutral and plasma conditions at the ITER divertor. The importance of the SOL opacity to neutral ionisation has been identified as a major player in determining the efficiency of the fuelling methods in tokamak devices and the value of plasma density at the separatrix (which in turn influences the divertor conditions) as described in Section 4.2.7. This has led to the development of fuelling methods which can be effective in the plasma

edge conditions expected in ITER; of which the injection of frozen pellets from the inner side of the torus seems to be the most promising one. These studies have provided the physics basis on which to carry out the studies for the fuelling required to achieve ITER reference performance, which are described in Section 4.3.2.

4.2. Experimental Basis.

4.2.1 Steady state transport in the scrape-off layer and its implications for divertor and wall interactions.

4.2.1.1. Steady state divertor power deposition profiles.

A significant part of the heating power in divertor tokamaks is lost by conductive and convective heat transport across the separatrix, into the scrape-off layer (SOL). Having crossed the separatrix, this power is primarily transported along field lines in the SOL to the divertor. In present machines, the parallel heat flux in the SOL can reach above 500 MW/m^2 [1] and in ITER it is expected to be ~ 1 GW/m^2. At the divertor surfaces this must be reduced below the technologically feasible, maximum perpendicular heat flux for actively cooled structures, typically 10 MW/m^2 normal to the surface in steady-state or up to 20 MW/m^2 during transients. Several strategies are employed in present machines to reduce the peak divertor heat flux; poloidally inclining the divertor tiles, increasing the magnetic flux expansion and broadening the SOL heat flux width through increased perpendicular transport all act to maximise the area over which power is deposited. In addition optimising the divertor geometry can increase the capability of the divertor to radiate power [2, 3] and good tile alignment or tile imbrication ('fish-scales') can minimize toroidal peaking at leading edges. The aim of these strategies is to achieve the conditions for partially detached divertor operation [4], the reference regime for ITER, for which modelling predicts tolerable peak heat fluxes [4].

The dependence of the steady state divertor heat flux profiles on both global and local parameters has been measured in many tokamaks and for a variety of divertor configurations [5, 6]. Heat fluxes are typically derived using data from infra-red cameras (IR), Langmuir probe arrays (LP) and thermocouples (TC), all of which have interpretation issues (e.g. IR thermography is subject to the effect of surface layers and localised hot-spots [7, 8; 9, 10], Langmuir probes only measure the electron component of the heat flux [11] and thermocouples rely on slow sweeping of the strike point [12] or shot repetition [13]). A comparison of IR, LP and TC time-averaged heat flux profiles for a typical ELMy H-mode on JET is shown in Fig.4.2.1-1. Profiles are usually time-averaged in ELMy H-mode (in part because few diagnostics have the necessary time resolution to distinguish ELMs) but observations from fast diagnostics indicate that ELMs either do not significantly modify the

inter-ELM profile (outer divertor) [14, 15, 16] or dominate it (typical of the inner divertor) [2, 8]. The outer target receives the majority of the divertor heat load, concentrated in a narrower profile than at the inner target (typical out:in power asymmetry ~ 2.5:1 and out:in peak heat flux asymmetry ~ 5:1) [17].

Scalings for the dependence of the peak heat flux, q_{max}, and heat flux profile width, λ_q, with key discharge parameters have been developed on a number of experiments. The dependence on total target heat load, P_{target} or the closely related power to the divertor, P_{div} are summarised in Table 4.2.1.1 for a number of these scalings. P_{target} (and P_{div}) will increase by more than an order of magnitude from current experiments to ITER, much larger than the extrapolation in other parameters such as toroidal magnetic field or density. The scatter in the power dependence from the various studies is large, even for different studies on a single device, and indeed both positive and negative dependencies are reported for the λ_q scalings. Several of the scalings are more pessimistic than that assumed in the ITER physics basis [18]. Even the most extreme scaling, however, yields λ_q for ITER of 3.7 mm ± 1.1 mm [19], not dissimilar to the value of λ_q ~ 5 mm obtained from fluid modelling of the ITER SOL [20], which is consistent with currently envisaged ITER operation. The scatter in the scalings may result from the difficulties of diagnostic interpretation referred to earlier, from poorly constrained data sets (e.g. inclusion of partially detached plasmas or ELM averaging over both type I and type III ELMy periods) or from subtleties in the profile shape (e.g. the width is ill-defined for a non-exponential fall-off). All that can be strongly concluded from Table 4.2.1.1 is that there is a need for improved experimental measurements and a theory-oriented approach to making extrapolations for the target heat flux in ITER (see section 4.2.1.2).

A change in the profile shapes was indicated on JET by measurements at low densities. For low ion collisionality, $\nu_i^* \leq 5$ ($\nu_i^* \equiv L_{//}/\lambda_{ii}$, where $L_{//}$ is the connection length and λ_{ii} is the ion-ion collisional mean free path), TC measurements of q_{max} at the outer target greatly exceed the inter-ELM LP value, Fig. 4.2.1-1 [21]. Interpreting this as a contribution from hot ions, it was inferred [22, 23] that the energy of D$^+$ ions striking the outer target was ~ 300 eV at ν_i^* ~ 1, consistent with CXRS measurement of separatrix ion temperature. The ion heat flux (derived from the difference in the TC and LP profiles) was closely correlated with a narrow peak in the outer profile [24]. This narrow peak was absent at the inner target although the ion component still dominated q_{max}. This asymmetry cannot be explained by toroidal geometry and ballooning-like transport alone. Classical drifts and/or neo-classical ion orbit loss (IOL) may play a role [25, 17, 26].
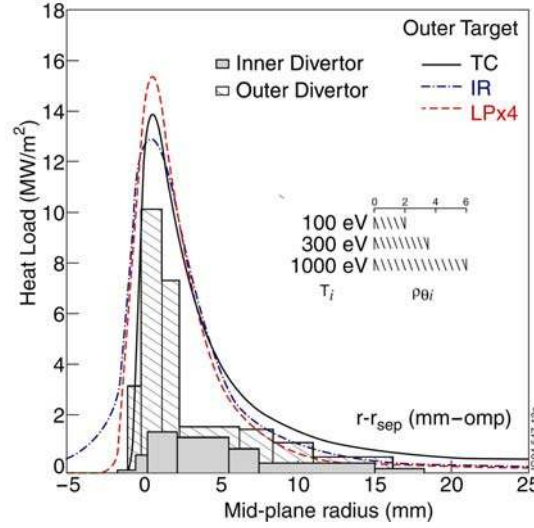
Figure 4.2.1-1. Comparison of ELM-averaged IR, LP (inter-ELM) and TC (histograms, ELM-averaged) derived heat flux profiles on the JET outer divertor target for a plasma with 16 MW NBI, 2.5 MA/2.4 T and ion B×∇B towards the X-point. The scale of the electron heat flux (LP) is four times smaller in the high power case. Also shown are the profiles obtained for a 12 MW Type-I H-mode (same field and current), using the shot-by-shot TC method (solid line). For comparison the poloidal gyro-radius at the outer mid-plane is shown for three values of the ion energy. [21].

The dominant role of classical (mainly E×B) drifts in SOL energy transport was confirmed in analysis of matched forward (fwd-B) and reversed (rev-B) JET discharges (ion B×∇B drift towards vs. away from the X-point) [19, 27]. Detailed modelling of direct ion orbit loss on JET using the ASCOT code (see section 4.3.3) correctly predicts ν_i^* as the governing parameter and can generally reproduce the fwd-B profiles on both targets but also predicts a strong modification of these profiles with field reversal, which was not observed in the experiment [19].

The outer mid-plane heat flux width predicted for ITER by extrapolation from JET TC analysis is $\lambda_q^{TC} \sim 3.7 \pm 1.1$ mm [17]. Taking the lowest value of ASDEX-Upgrade, DIII-D, JT-60 data from the multi-machine scaling ([28], Fig.5) and the ASDEX-Upgrade scaling for DIV II from IR-measurements, a lower limit of 5 mm is predicted. In ITER, the target power load must not exceed the allowable limit: $P_{SOL} f_{div} / 2\pi R_t \lambda_q f_{amp} \leq q_{acc}$ (derived from [11]), where q_{acc} is the maximum acceptable peak heat flux, R_t the major radius of the outer target, P_{SOL} the power entering the SOL, f_{div} the fraction of P_{SOL} delivered to the outer target, λ_q the mid-plane heat flux width and f_{amp} the ratio of target to mid-plane heat flux width. The design values for ITER [20] are $q_{acc} = 10$ MW/m^2, $R_t = 5.5$ m, $P_{SOL} \sim 80$ MW and $f_{amp} \sim 10$ (4 from magnetic flux expansion and 2.5 from target inclination). Then the requirement is $f_{div} \sim 0.04\lambda_q$ [mm], resulting in $f_{div} \sim 0.2$ for $\lambda_q = 5$ mm, consistent with fluid modelling results (which indicate that power loading can be controlled by the divertor density) [29]. The TC predicted value of $\lambda_q = 3.7$ mm results in a somewhat more constraining value of $f_{div} \sim 0.15$.

	λ_q	q_{max}	Comment
Multi-machine JT60-U, DIII-D and ASDEX-Upgrade (DIVI) [28]	$P_{div}^{0.44\pm0.04}$	-	Scaling for λ_q mapped to outer mid-plane
Multi-machine JT60-U, ASDEX-Upgrade [18]	$P_{t\,\arg et}^{0.35\pm0.05}$	-	
ASDEX-Upgrade (DIVI) (IR data) [2]	$P_{t\,\arg et}^{0.52\pm0.05}$	$P_{t\,\arg et}^{0.5\pm0.05}$	Type I and III ELMs included and partially detached plasmas
ASDEX-Upgrade (DIVII) (IR data) [2]	$P_{t\,\arg et}^{-0.1}$	$P_{t\,\arg et}^{1.1\pm0.06}$	Type I ELMs and attached plasmas only
DIII-D [30]	-	P_{div}^{1}	
JET (IR data) [31]	$P_{t\,\arg et}^{-0.13\pm0.08}$	$P_{t\,\arg et}^{1}$	Inter-ELM. λ_q from FWHM of profile at outer target
JET (TC data) [17]	$P_{t\,\arg et}^{-0.48\pm0.09}$	-	ELM averaged. D (Type I ELMs) and He (Type III ELMs) discharges included. λ_q from integral width of profile at outer target.

Table 4.2.1.1 Scalings for dependence of SOL heat flux width and peak target heat flux with total target (or divertor) power load for a number of machines and multi-machine databases.

4.2.1.2. Steady state energy transport in the near SOL.

The width of the near-SOL, within 1-2 λ_q beyond the separatrix, is governed by competition between poloidal transport, which results from parallel (to the magnetic field lines) and diamagnetic (tangential to the magnetic surfaces and normal to the field lines) components, and the much slower perpendicular transport (normal to the magnetic flux surfaces). Parallel energy transport is determined by classical conduction and convection, with kinetic corrections to heat diffusivities $\chi_{//i,e}$ at low (separatrix) collisionalities $\nu_{i,e}^{*}$, whilst diamagnetic transport is governed by a mix of classical (E×B, B×∇B, curvature, diamagnetic, etc.) and anomalous drifts [11, 25, 32, 33]. Perpendicular, or radial, energy transport is turbulent in nature, with typical heat diffusivities in the range $\chi_{\perp}^{SOL} \sim$ 0.1-1 m^2/s, well in excess of classical diffusion ($<10^{-3}$ m^2/s). The development of a credible theory for $\chi_{\perp}^{SOL}$ is key to reliable predictions for near-SOL energy transport in future devices such as ITER.
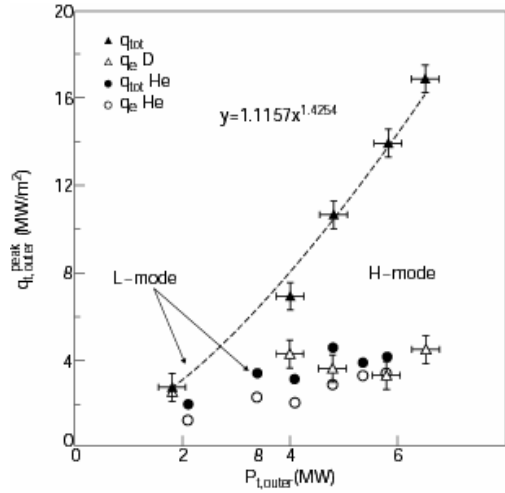
Figure 4.2.1-2. Peak total (TC), q_{tot} and electron (LP), q_e heat fluxes to the outer target for deuterium (D) and helium (He) plasmas as a function of power entering the SOL, $P_{t,outer}$. The ion contribution becomes more pronounced in D at higher power. Also shown is the peak inter-ELM heat flux to the outer divertor for an H-mode power scan in JET as measured by IR-measurements (dotted line) [17]

Transport coefficients in the near-SOL can be reconstructed using divertor target profiles of heat flux, density n_e and temperature $T_{e,i}$ (see section 4.2.1.1) together with upstream (e.g. mid-plane) n_e and T_e profiles from high spatial resolution Thomson scattering or reciprocating probes. Unfortunately, target profiles can be decoupled from the SOL transport by recycling neutrals and impurity radiation near the divertor and X-point [34], although these effects are generally less important in the high power, low density attached plasma regimes discussed in section 4.2.1.1. Given this problem and the general scarcity of data, attempts to extract transport coefficients often assume radially constant $\chi_\perp$ values in the edge, sometimes with a prescribed poloidal variation, in the hope of determining scalings for the dependence of $\chi_\perp$ on plasma and device parameters. An interpretive version of the 2-D fluid code B2-SOLPS5.0 [35] has been used ([36]) to develop a multi-variable, power law regression scaling for $D_\perp$ and $\chi_\perp$ in ASDEX-Upgrade by fitting the inter-ELM experimental data, whilst adjusting constant $D_\perp$ and $\chi_\perp$ values separately. A similar approach was employed for JET data [22] using the EDGE2D/NIMBUS package [37] to match target profiles. In this study, radially piece-wise constant $D_\perp$ and $\chi_\perp$ were assumed; for the outer core, the edge transport barrier (ETB) and the SOL, with a radial pinch velocity being invoked (typically, inward in the ETB region and outward in the SOL) to match the upstream n_e and T_e profiles. The results from both studies imply a stronger $\chi_\perp$ dependence on β than ν^* (note that because of the paucity of the T_i data, $\chi_{\perp i} = \chi_{\perp e}$ was assumed). Unfortunately, the 2D fluid code approach is computationally expensive, limiting the parameter space resolution, and has only been attempted separately for different machines, so no size scaling has be derived. Thus no extrapolation to ITER has been proposed.

Another, less computationally demanding approach was initially proposed by [38] and expanded by [39]. Analytical expressions for λ_q, developed using the two-point SOL model [40] from published theories of SOL radial transport combined with limiting cases of parallel transport (pure conduction vs. pure convection), are evaluated against a wide range of experimental data for λ_q and the key plasma parameters. The normalised RMS error of the predicted vs. measured scaling is used as the figure of merit to assess the credibility of the theoretical models for $\chi_\perp$ involved. Initial studies [39, 41, 42] examined the target heat flux width measured by LP (thus dominated by the electron heat flux), λ_q^e from COMPASS-D (Ohmic and L-mode, $\nu_e^* \sim 0.2\text{-}3$), Alcator C-mod (Ohmic, $\nu_e^* \sim 20\text{-}370$), and JET (Ohmic, L- and H-mode, $\nu_e^* \sim 10\text{-}100$) and focused on scalings with respect to n_e, P_{SOL}, q_{95} and B_ϕ. For $\nu_e^* > 10$ (i.e. for both JET and Alcator C-mod), five different theories emerged as noticeably better than the rest and all these exhibit a $\chi_\perp^{SOL} \propto T_e^{1/2} n_e^{-1}$ scaling leading to a negative power dependence, $\lambda_q^e \propto P_{SOL}^{-2/5}$. For $\nu_e^* < 3$ (COMPASS-D), the three best theories exhibit the same scaling $\chi_\perp^{SOL} \propto T_e^{1/2} n_e^{-1}$, although ten other theories, yielding different scalings, could not be statistically rejected. More recent statistical studies [17] of λ_q relied solely on JET data for IR or TC measured target total power profiles, obtained over a wide range of powers, densities, fields and currents (L- and H-mode, $\nu_e^* \sim 8\text{-}15$), and including both deuterium and helium plasmas (see section 4.2.1.1). The list of the applied theories was extended with collisional (classical or neoclassical) and direct ion orbit loss radial transport mechanisms. Comparison with experiment, Fig. 4.2.1-3, suggests that either Pfirsh-Schlueter-regime ion heat conduction or collisional ion orbit loss may play an important role in SOL power exhaust. The c*ollisional* ion orbit loss heat flux width $\lambda_q^{X\text{-}\nu^*} = \lambda_q^X \nu_i^{*1/2}$, where the *direct* ion orbit loss width, λ_q^X was calculated for JET using the ASCOT guiding centre code.

Comparing the results of the earlier and more recent studies suggests that different mechanisms may be involved in electron and ion transport in the SOL, possibly the former being linked with drift wave turbulence and the latter with collisional heat diffusion. Extrapolation of the results, however, to a next-step device such as ITER (section 4.2.1.1) should be taken with care (see also section 4.3.2). Further experiments are clearly required to resolve this issue, including higher resolution diagnostics and advances in transport modelling. In particular, development of diagnostics capable of measuring the ion temperature profiles at different locations in the SOL is a high priority.

4.2.1.3. Particle transport in the SOL.

Particle transport in the edge plasma and scrape-off layer plays a key role in the performance and operation of a fusion reactor: setting the width of the scrape-off layer density profile and its impurity screening characteristics, regulating the energetic particle fluxes onto first-wall components and associated impurity generation rates, and determining the

effectiveness of the divertor in receiving particle exhaust and controlling neutral pressures in the main-chamber. Here we focus on transport physics that occurs in the absence of ELMs, which is based on data from L-mode discharges and from H-mode discharges at time intervals without ELMs.

Observations and analysis of profiles, plasma fluctuation phenomena, and scalings of particle transport within and across a number of experimental devices have pointed towards a few key elements which are illustrated in Fig. 4.2.1-4: (1) tendency for strong variation in the profile gradients and transport parameters (and physics) from the separatrix to the first-wall, dividing the SOL into *near* and *far* regions, (2) bursty transport dynamics in the far SOL (reminiscent of 'avalanches' in a self-organized critical system), carrying significant cross-field particle flux towards the first-wall, and (3) dependence of near SOL transport on the local collisionality. While a first-principles, quantitative description of the phenomena is not yet in hand, the experimental observations have important implications in the areas of main-chamber recycling and impurity sources, threshold conditions for divertor detachment, and the tokamak density limit.
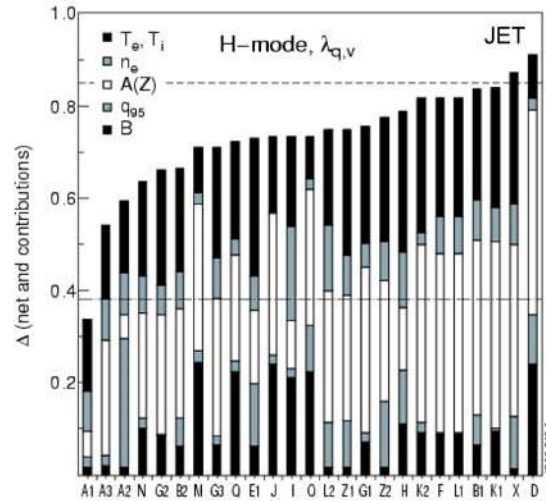

Figure 4.2.1-3. RMS error between theoretical and experimental λ_q exponents, assuming dominant parallel convection and showing contributions from (T_e, T_i), n_e, $A(Z)$, q_{95} and B_ϕ exponents. Dot-dashed line represents estimated measurement error, while the dashed line is the average over all theories [17].

Scrape-off layer profiles in many devices are often found to exhibit a two-zone structure: a steep gradient region in density and temperature near the separatrix (*near* SOL) and a flatter profile region (*far* SOL). Characterized as a 'shoulder', extending from approximately one steep-gradient scale length outside the separatrix to the wall (e.g., ASDEX [43, 44], ASDEX-Upgrade [45, 46], TEXT-U [47], DIII-D [48, 49], C-Mod [50, 51], JT-60U [52], JET [53], TEXTOR [54], TCV [55]). The earliest hints that cross-field particle transport in the far SOL toward the main-chamber walls could be important for a tokamak reactor, competing with, or even exceeding, the parallel loss into the divertor, came from ASDEX-Upgrade [45, 46]. Subsequently, Alcator C-Mod focused attention on this behaviour as it was reported to

operate predominately in a 'main-chamber recycling regime' with much of the plasma efflux recycling on main-chamber surfaces rather than on divertor targets [56, 57, 58]. The primary cause was linked to a strong increase in the effective cross-field particle diffusivity (D_{eff} = -$\Gamma/\nabla n$) with distance into the SOL, a result consistent with earlier heat diffusivity analyses [59, 60, 42], and particle transport analysis [43, 45, 46, 61].

In related work it was shown that divertor neutral bypass leaks and/or open versus closed divertor structures showed little effect on the midplane pressure in Alcator C-mod [59, 62, 63, 64], an indication that rapid cross-field particle transport was the dominant source of main chamber neutrals. These observations paralleled and confirmed those made in ASDEX-Upgrade [65, 66] where the main-chamber neutral pressure was found to be insensitive to divertor geometry at medium and high densities and that the level of main-chamber recycling and the density in the far SOL region were strongly correlated [67]. In DIII-D, the ion flux to the wall is typically of the order of the ion flux received at the divertor plate, increases with plasma density, and dominates in detached divertor regimes [68]. The contribution of main-chamber recycling to midplane neutral pressures is not uniformly reported to be important, suggesting a sensitivity to divertor/first-wall geometry and/or operational regime [69]. For example, DIII-D [70], JET [71], and JT-60U [52] have reported a reduction in main chamber ionization sources and neutral pressures when the divertor was changed to a more closed geometry.

It is generally accepted that the level of plasma flux that reaches a given wall surface depends on its wall-plasma gap – perhaps explaining some of the variability that is reported across different experiments. However, because of practical limitations, the main-chamber wall cannot be placed arbitrarily far from the plasma. Moreover, the main-chamber wall includes the neutral baffles at the entrance to the divertor, structures which are fixed at locations to optimise divertor neutral retention. These structures, in conjunction with the inner-most magnetic flux surface that passes through them, may be thought as defining a 'window frame' [72, 68]. Since the particle flux crossing this window frame depends only on plasma transport processes, it is largely independent of the details of the first wall. Thus, while first-wall geometry and placement may affect the poloidal distribution of main-chamber recycling, it is not expected to significantly influence the overall level.

Scaling studies of gradient lengths, effective diffusivities and/or time-averaged particle transport velocities have revealed important dependencies which serve to constrain physics-based descriptions. For example, a number of experiments have identified a steepening of gradients (inferred as a reduction in diffusivity) as the local electron temperature increased [59, 52, 42, 73, 74] as well as little sensitivity to the value of the magnetic field strength [59, 42, 39, 75]. These observations are clearly incompatible with a Bohm-like diffusion model and more in-line with a critical-beta model combined with a collisionality dependence [76], perhaps further constrained by a relationship between density and temperature gradients, η_e =

d(Log T_e)/d(Log n) ~ 2 [67, 77]. Recently, particle diffusion coefficients and cross-field transport velocities ($v_{eff} = \Gamma/n$) in the near SOL have been correlated with parallel collisionality which also correlates with discharge density normalized to Greenwald density (n/n_G) [51, 78]. As collisionality increases, fluctuation amplitudes, particle transport and associated heat convection increases dramatically across the SOL, impacting the SOL/divertor power balance at moderate n/n_G (promoting divertor detachment) and impacting discharge power balance at high n/n_G (promoting thermal collapse and density-limit disruption). A strong variation of cross-field heat diffusivity with n/n_G has also been noted on ASDEX-Upgrade [79]. At a basic plasma physics level, the latter observations suggest that SOL turbulence and resultant cross-field transport may set a fundamental density limit for tokamaks even in the absence of impurity radiation [80]. In practice, the operational density limit for a reactor will also involve the limitations of impurity peaking and radiation as well as requirements to remain in an H-mode regime.

The underlying physics of cross-field transport involves plasma turbulence. Data from a number of experiments have demonstrated a clear correspondence between the character of edge plasma fluctuation phenomena in the near and far SOL regions and particle transport levels [49, 51, 81, 77, 82, 83]. Fluctuations in the far SOL are found to exhibit a 'bursty' character, with intermittent 'transport events' carrying plasma towards the main-chamber wall with velocities well exceeding 100 m s^{-1}. Turbulence imaging systems record 'blobs' or plasma 'filaments' aligned with respect to the local B-field and propagating poloidally and radially-outward [84, 85, 86]. The probability distribution functions (PDFs) of the fluctuations exhibit a non-Gaussian tail, such that large-amplitude but rare outward-going transport events account for a large fraction of the total particle flux. A statistical link between bursty transport behaviour and the departure from the most probable gradient has been recently identified [87]. These characteristics appear to be independent of confinement mode (L- vs. H-mode) [85, 86], although the time-averaged fluxes tend to be lower in H-mode discharges, consistent with a global increase in particle confinement. It should be noted that while non-Gaussian PDFs, intermittency, and motion of coherent structures has been well documented over a number of years [88, 89, 90, 91, 92, 93, 94, 95, 96, 97], clear connections to a rapid cross-field transport mechanism in the far SOL and the potential impact on tokamak reactor operation have only recently been widely recognized.

In contrast to the far SOL, fluctuations in the near SOL region are found to exhibit a near-Gaussian PDF. Moreover, at locations inside the separatrix there is evidence of reversed skewness or the formation of plasma 'holes' [86]. Folded into this picture are the observations that transport and fluctuation levels on the high-field side SOL are significantly reduced relative to the low-field side [85, 89, 98, 99], consistent with the expectation of higher turbulence and transport levels in regions of 'bad' field-line curvature. In summary, fluctuation statistics combined with data from turbulence imaging 'movies' indicate that

plasma structures intermittently 'peel away' from the edge of the steep-gradient near SOL region and freely propagate towards the wall, independent of L- or H-mode confinement. Magnetic curvature and/or variation in |B| appear to play a role. These observations suggest that the overall level of cross-field particle transport in the SOL may ultimately be set by conditions near the separatrix.

While the appearance of shoulders in the far SOL aided in the discovery of a rapid transport phenomena in this zone, particle balance analysis suggests that the same underlying transport physics is active in discharges without a shoulder. For example, although only a weak shoulder is normally observed in JET, the cross-field convection velocity profiles inferred from particle balance are found to be remarkably similar to that inferred in discharges from C-Mod [100] where the dimensionless plasma physics parameters were similar. Comparisons between DIII-D and C-Mod yield the same trends [101]. The opacity of the far SOL to neutral penetration may offer part of the explanation for the appearance of a shoulder [101]; if wall-recycled neutrals ionise in the far SOL, they are rapidly transported back to the wall as ions. Thus, depending on the opacity to neutrals and the underlying cross-field plasma transport, the far SOL can exhibit a 'perpendicular recycling' regime with flattened density profiles [58, 102, 103, 101]. In tokamak plasmas with the same dimensionless plasma physics parameters, the SOL would tend to be less opaque to neutrals as the machine gets larger, consistent with JET – C-Mod comparisons [100]. However, the ITER SOL is expected to be dimensionlessly dissimilar to any current tokamak and opaque to neutrals [20], which may lead to the appearance of a shoulder in the far SOL for gas-fuelled discharges.

In light of the transport physics in the far SOL, the level of plasma interaction with main chamber surfaces is a concern. Relative to target-produced impurities, main chamber impurities are poorly screened by the SOL, can impact the core plasma [104, 105, 106], and may affect co-deposition of carbon and tritium in the divertor [107]. Moreover, the rapid transport mechanism sets a minimum level of recycling and neutral pressure surrounding the confined plasma, which is largely independent of divertor geometry and neutral bypass leakage.

Clearly, more research is required to develop quantitatively accurate models for particle transport in the tokamak edge. The development and testing of physics-based descriptions is particularly important since we need to understand how the behaviour seen in present devices scales to reactor-size machines. Cross-machine comparisons are particularly valuable to explore the universality of the transport phenomena and the dependence on dimensionless parameters, and hopefully allow, at a minimum, an empirical projection to reactor devices. The abovementioned comparisons between C-Mod, DIII-D, and JET shows SOL profiles (including D_{eff} and v_{eff}) that are similar in shape and magnitude when scaled according to dimensionless plasma physics parameters [100, 101]. In particular, v_{eff} is found to have a weak dependence on those dimensionless parameters. These results give an initial guide and

suggest that the total plasma flux onto main-chamber surfaces may be roughly independent of machine size in dimensionlessly identical discharges, confirming observations in [72]. However, the scaling of these results to ITER is complicated by the lack of a complete set of matching dimensionless parameters in present tokamaks plus the lack of surety regarding the importance of SOL opacity to neutrals.

4.2.1.4. SOL flow and classical drifts effects.

SOL mass transport along or parallel to the magnetic field lines (SOL flow) is of direct relevance to divertor pumping efficiency and impurity screening properties of the SOL. The primary measurement of such flows in the SOL is by Mach probes [108, 109, 59, 6, 110, 111, 51, 112, 113, 114]. In Fig. 4.2.1-5, parallel Mach number ($M_{//}$) results are compared for L-mode plasmas in JT-60U [112], JET [115] and C-Mod (inner wall probe only) [114]. These measurements show that there is a stagnation point in the SOL flow between the outer midplane and the lower divertor x-point for the normal field direction (ion grad-B drift direction down). In the remainder of the SOL there are subsonic flows towards the inner divertor ($M_{//}\sim 0.3$-1.0) peaking at the inner midplane SOL [114] and dropping towards the inner divertor. For reversed field, the stagnation point appears to be at the top of the plasma for lower single-null plasmas; there are SOL flows towards both the inner and outer divertors. The change in flows with reversal of magnetic field is not symmetric about zero flow [108, 109, 59, 6, 113, 111, 51].

The dependence of SOL flows on main plasma parameters has also been investigated. The most common tendency for the SOL flow is a reduction in $M_{//}$ at the outer midplane SOL [59, 6, 115], and $M_{//}$ enhancement at the inner midplane SOL [112, 114] with increasing n_e. This tendency is common for the two toroidal field directions. The flow in the private flux region is considered another possible mechanism for producing in-out asymmetry in the divertor ion flux (as described below).

The accuracy of flow measurements based on probes [116] is the subject of concern given the high Mach numbers inferred, the suspicion that the probe perturbs the measurement [115] and the difficulty modellers have had matching experimental measurements (covered later in this section). Other, less perturbing methods have been attempted to give further information. One such method is to observe directly the effect of drifts on the transport of impurities. In Alcator C-MOD, 2-D measurements, using CCD cameras, of impurity plumes (HeII, NII, NIII) from local gas puffs [117, 118] from both the HFS and LFS of the machine were analysed. Unfortunately, this method is very complex and gives only qualitative support to probe measurements (e.g. sign but not magnitude) with the caveat that it can only be used when the ion-impurity collision time of the charge state measured is shorter than the ionisation time.

Spectroscopic measurements of parallel flow velocities of low charge state impurity ions (CII, CIII, BII, HeII) is another alternative flow measurement [119, 120]. Such measurements are roughly consistent with expectations for flow patterns in the divertor but direct comparisons with probes have not been made.

There are several contributing physics processes that have been implemented in 2-D edge transport codes to model flows. In neo-classical theory of plasma transport in toroidal geometry, $E \times B$ and $B \times \nabla B$ (or diamagnetic for fluid model) drifts play an essential role in determining parallel flows and currents, e.g. the Pfirsch-Schlüter return current is a direct consequence of these effects. In the scrape-off layer parallel SOL flow can be produced due to the poloidal asymmetry of $E_r \times B_t$ and $\nabla p_i \times B_t$ drifts [121, 122, 11].

When implemented in 2-D edge transport codes with realistic magnetic geometries (fluid codes such as UEDGE [33, 123], B2-Eirene [35, 124, 125], EDGE2D[126]), drift effects lead to qualitatively similar SOL flow patterns to those observed in experiments [123, 126, 108]. In other words, they are consistent with the measured SOL flow direction (in particular, near separatrix), but underestimate the SOL Mach numbers by factors of 2-5.

Modelling SOL flows is an active area of research, with several avenues being explored. These include: a) torque generation due to surface averaged $\langle j_r \rangle$, b) coupling between turbulence and SOL flow via the Reynold's stress [87], c) global circulation of particles due to outward movement of plasma filaments (blobs) and enhanced turbulence on the bad curvature (outer) side of the torus [114, 127] and d) problems with Mach probe interpretation itself, e.g. the effect of impurity cooling on the $M_\parallel$ magnitude [115] or difficulty in distinguishing between the parallel and toroidal components of the SOL flow [128].

(a) *Near/Far* SOL and Fluctuations

(c) Regression Analysis of D_{eff}, in *Near* SOL (ρ = 2 mm)

(b) Density and D_{eff} Profile Evolution
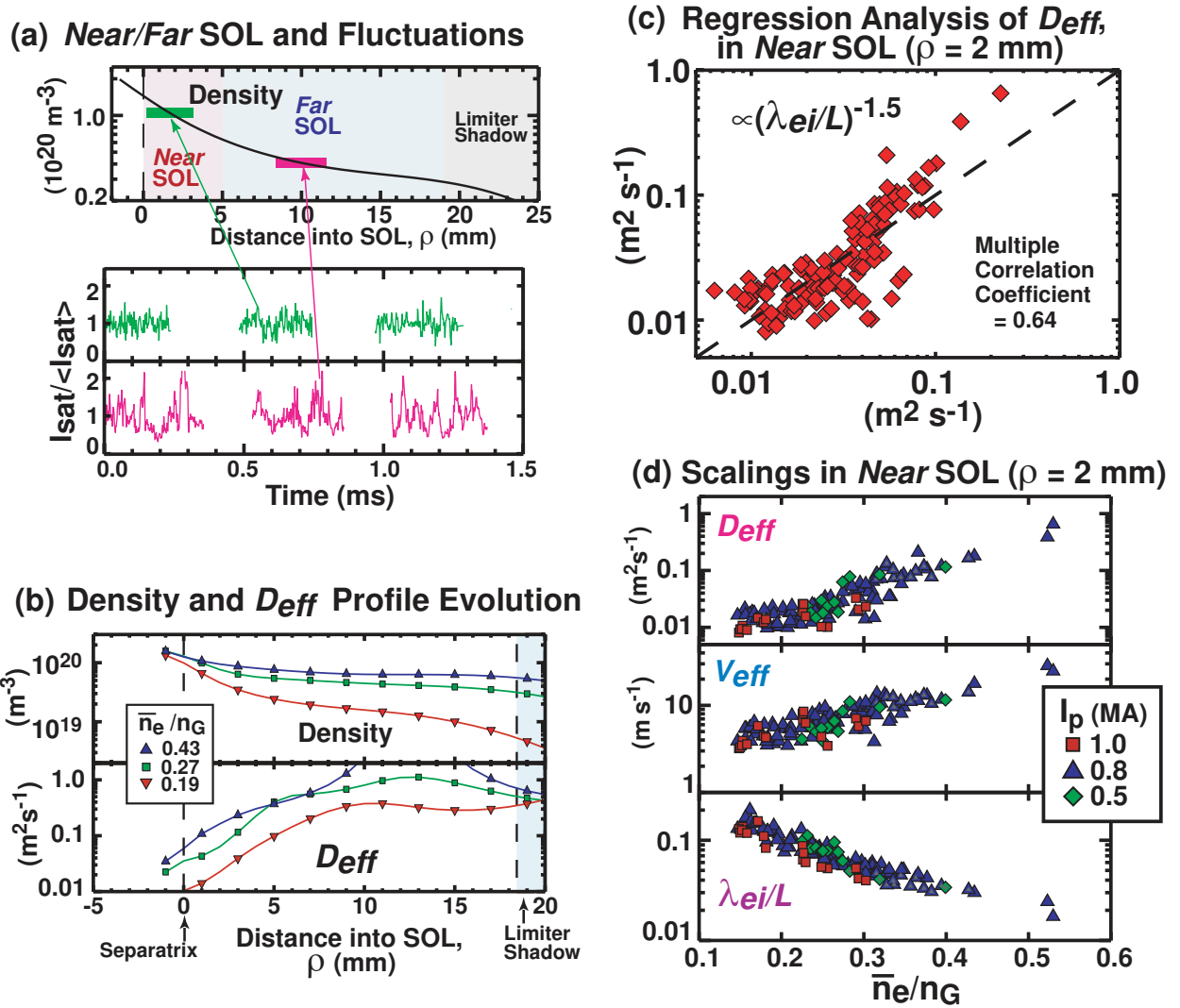
(d) Scalings in *Near* SOL (ρ = 2 mm)

Figure 4.2.1-4. SOL profiles and plasma transport characteristics in ohmic L-Mode discharges on Alcator C-Mod (from Refs. [51, 78]) which illustrates key features seen in many devices: (a) near and far SOL zones with change in fluctuation character, (b) strong variation in D_{eff} across the SOL and flattening of the SOL with increasing core density, (c) correlation of near SOL D_{eff} with parallel collisionality, (d) trend of increased particle transport coefficients with increased discharge density (collisionality).

The situation is complicated further in the divertor. That is because of the existence of strong ionization sources as well as strong parallel and radial gradients of the plasma temperature and density near the separatrix. The latter lead to $E_{\theta} \times B_t$ and $E_r \times B_t$ drifts with resultant cross-field and poloidal particle fluxes, respectively [129]. Direct measurements of the private flux region $E_r \sim 3T_e/\lambda_q \sim$ 5-20 kV/m [54, 130, 131] suggests that E×B fluxes are comparable to the parallel fluxes under attached conditions, but are substantially smaller following detachment [131]. Enhancement of the divertor parallel flows upon detachment have been both measured [130, 6] and simulated using UEDGE and B2 [132, 133].

Simulations of the divertor flows using the UEDGE code [130, 123, 131] are in qualitative agreement with the above findings, suggesting a link between drifts, divertor

plasma flows and in-out divertor asymmetries. UEDGE predicts the formation of a plasma potential and pressure maximum at the X-point which drives a clockwise circulation (for normal B direction) of E×B flux around the X-point [123]. Divertor asymmetries in JET have similarly been reproduced by both EDGE2D and SOLPS including drift effects [27]. Such a circulation pattern, if of significant strength, could also affect the x-point region and radiation there, thereby affecting aspects of H-modes (transitions, cooling the pedestal).

4.2.1.5. Use of extrinsic impurity radiation to reduce divertor heat loads.

Extrinsic impurity injection is considered necessary to achieve and control the desired radiated power fraction (> 50%) for the reduction of the divertor heat load in ITER to an acceptable level [134]. The challenge is to find a robust regime with sufficiently high radiated power fraction and acceptable effects on the core (Z_{eff}, cooling of the pedestal). The ability to disperse the short ELM energy pulse using divertor radiation is discussed in section 4.2.2.6. In this section we concentrate on using radiation to reduce the power flowing to the divertor in a more general sense, not limited to the divertor or to ELMs.

While Type I ELMs are considered the primary operational regime for ITER it is generally found that radiation cannot be used to affect the ELM energy pulse itself (section 4.2.2.6). Still, averaging over ELM and between-ELM periods, large radiated fractions have been achieved through addition of Ar. As an example, JET has demonstrated high δ discharges with radiated power fraction f_R = 0.7, $H_{H98(y,2)}$ = 0.9 at β_N= 2.1 and Greenwald density fraction, f_G = 1.15 [135]. The use of Ar to disperse divertor power flux has also been applied in JT-60U with initial results similar to that of JET - 0.5 % of argon made it possible to create plasmas having f_R =0.8, f_G = 0.65 and $H_{H98(y,2)}$ =1. Even though a half of the radiated power was dissipated in a mantle inside the separatrix, electron and ion temperatures remained high in the centre and also in the pedestal [136, 137, 138, 139]. Good confinement ($H_{H98(y,2)}$ =0.96) at high density ($\overline{n}_e/n_{GW}$=0.92) with high radiation loss fraction (f_R~1) has been demonstrated more recently in JT-60U high β_p H-mode plasmas by utilizing high-field-side pellets and Ar injection. Argon accumulation was found to be modest and well within acceptable levels [140].
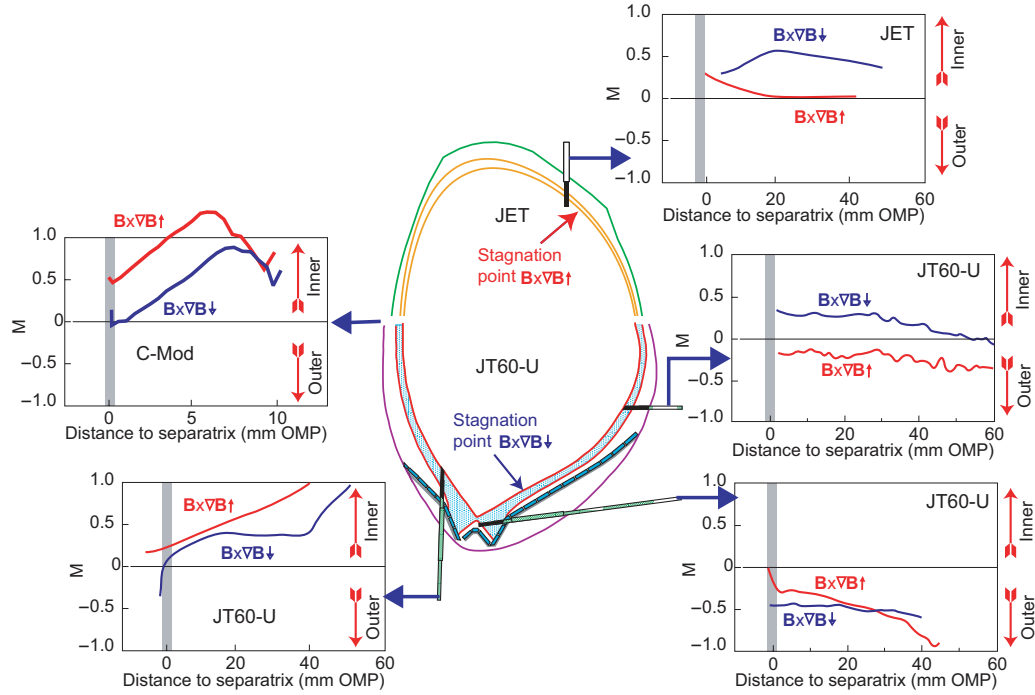
Figure 4.2.1-5. Parallel Mach number measurements are compared for L-mode plasmas in JT-60U [141], JET [115] and C-Mod (inner wall probe only) [114], (after [142]).

Type III ELMs have been observed in all divertor tokamaks and are small enough to be easily compatible with the transient power limits for the divertor targets (see section 4.2.2.1), although energy confinement is typically 25% lower than with Type I ELMs, due to the loss of pedestal energy. Both JET and ASDEX Upgrade have achieved radiated power fractions approaching 80% [143, 144]. In ASDEX Upgrade, it was found that the reduction in confinement associated with Type III ELMs could be compensated by core density peaking in the so-called completely detached H-mode (CDH) [143]. Unfortunately, in larger tokamaks such as JET, this compensating enhancement of core confinement has not been found [145]. However, dependent on certain scaling assumptions, low q_{95} ($\sim$ 2.6), nitrogen seeded, Type III ELMy H-mode discharges have been demonstrated in JET with normalised confinement and density sufficient for Q=10 inductive operation in ITER, whilst the steady state and transient power loads are comfortably within acceptable limits (Fig. 4.2.1-6) [144].

Radiation dissipation of power efflux has also been applied to Internal Transport Barrier (ITB) plasmas. One of the few machines to address this issue has been JT-60U where neon seeding was used in reversed shear plasmas to achieve a radiated power fraction of more than 80 % without losing confinement at high density [146]. However, this strongly radiating ITB plasma regime remains fragile and there are still issues related to scaling, accessibility and control, which will need to be investigated before it can be adopted for ITER.
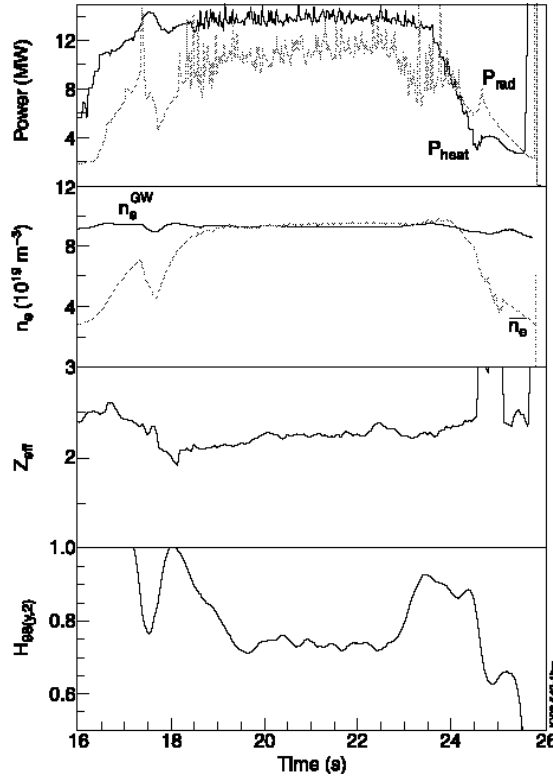
Figure 4.2.1-6. Overview of JET nitrogen seeded type-III ELMy H-mode #59029. Key parameters for this shot are: I_p=2.5(17)MA, B_T=2(5.3)T, q_{95}=2.6(2.6), triangularity δ=0.44(0.5), β_N=1.7(1.5), H_{98}=0.73(0.75), f_{GDL}=1.0(1.0), f_{rad}=0.8(0.75), Z_{eff}=2.2(1.7), $\Delta W_{ELM}/W_{Total}$<0.015(0.03) [144] where the required values for low q_{95} operation of ITER at Q=10 are given in brackets.

Real-time control of radiating scenarios is essential for maintaining optimal conditions in long pulses. The JET Type-I ELM regime described above is an example of simultaneous feedback control of the H-factor and fraction of the radiated power using Ar. Good performance was maintained for 5 seconds with constant neutron yield, formation of a radiating belt and reduction of target plate temperature [135], although, the resulting core argon concentration in such discharges is higher than required for ITER. In ASDEX Upgrade, a new control technique has recently beendeveloped in which simultaneous feedback on the divertor neutral particle flux and electron temperature are combined with external ELM triggering via high field side pellet injection (e.g. [147, 148], to maintain power flux control and prevent impurity accumulation caused by ELM-free operation. The `effective` divertor temperature is obtained from real-time measurements of the thermoelectric currents flowing between the inner and outer divertor targets [149]. The applicability of such scheme to ITER will thus depend on the feasibility of thermoelectric current measurements in ITER or their replacement by an alternative control parameter.

Accumulation of impurity in the core plasma is a potential problem associated with impurity seeding [150, 140]. It has recently been shown that under specific conditions, the addition of central power deposition using wave heating such as ICRH and ECRH has being

identified as an effective tool for core impurity control [151, 152]. Analysis of these discharges indicates that increased central diffusion, due to additional power flux, counteracts the neo-classical inward pinch for impurities and/or that flattened central electron density profiles with increased central heating reduce the inward part of the neo-classical drift [153, 154]. The α-heating in a burning reactor might be expected to provide a centrally peaked power deposition profile favourable for impurity transport [153].

4.2.2. Transient ELM Transport.

4.2.2.1. Materials limits for ELMs and disruptions energy loads on plasma facing components.

Erosion during thermal transient events such Type I ELMs and disruptions plays a major role in the choice of plasma-facing materials for the ITER divertor and first wall. Since a large number of ELMs (of the order of several hundred) are expected in each ITER discharge, it is crucial that the surface temperature rise due to an individual ELM remains below the threshold for sublimation or melting (for carbon or metals respectively). Otherwise significant target plate erosion due to vaporisation or loss of the melt layer (only for metals) can occur. Details of the calculated vaporization (for CFC and W) and melting (only for W) occurring at the ITER divertor under Type I ELM-like energy loads for a range of assumptions are given in [155].

In contrast to ELMs, disruptions are not very frequent events (1-10% of discharges are expected to disrupt in ITER) but the expected energy fluxes are typically one order of magnitude larger than for ELMs. The major concern in the case of disruptions is the resulting damage to, and erosion of, plasma facing components (PFCs), including possible formation of melt droplets.

Using a simple 1-D semi-infinite solid approximation, the various PFC damage thresholds for ITER can be roughly estimated as $\Delta E/\sqrt{t} \sim$ 35-40 MJ m^{-2} s$^{-1/2}$ for sublimation of C, $\sim$ 45-50 MJ m^{-2} s$^{-1/2}$ for sublimation of W and about $\sim$ 40 MJ m^{-2} s$^{-1/2}$ for melting of W [15, 2], where ΔE is the energy density deposited in a time interval, t. Recent calculations, assuming a short ELM pulse-width, show that a large number of ELMs with energy densities much larger than 1MJ m^{-2} would lead to an intolerably short divertor target lifetime due to erosion, as shown in Fig. 4.2.2-1 for a 2 cm thick CFC target in ITER [155].

More precise estimates of the expected lifetime of PFCs under transient loads and of the effects of the ensuing impurity fluxes on ITER plasmas require more sophisticated models [156, 157, 158, 159, 160]. These models are being validated at present with experiments in ELM simulation facilities [161] and tokamaks in order to use them for quantitative estimates of the relevant effects in ITER.

Such estimates for ITER are, however, subject to large uncertainties both in terms of ELM-physics and materials characteristics : the expected divertor ELM energy load, its spatial and temporal distribution (subjects of this section), characteristics of the redeposition of ELM-eroded material, behaviour of shallow melt layers (for W), CFC thermo-mechanical behaviour at high temperatures, etc. In addition to evaporation and melting, larger scale erosion mechanisms could arise after repetitive high thermal loads. Local stresses in the near surface could lead to deterioration of material properties and subsequent ejection of chunks/droplets of material [161].
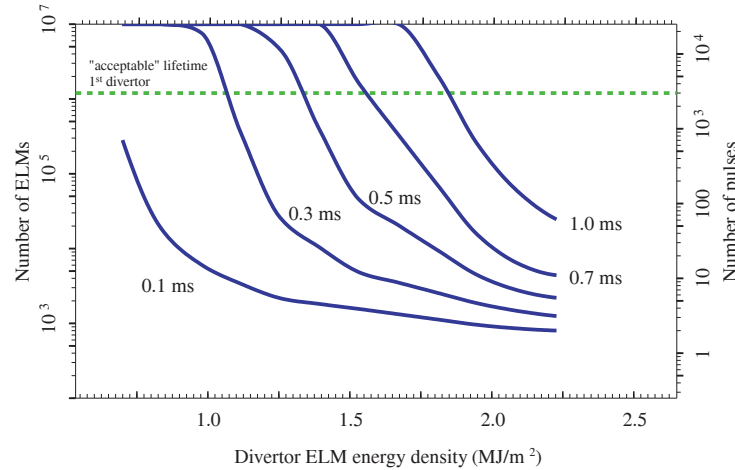

Fig. 4.2.2-1 Erosion lifetime (in number of ELMs or corresponding ITER full power pulses) of an ITER CFC target (2 cm thick) as a function of the ELM energy density on the divertor target for various timescales of the ELM energy pulses [155].

4.2.2.2. Transport of ELM energy and particles from the confined plasma to PFCs.

A major concern about the proposed Type I ELMy H-Mode scenario for ITER is the magnitude of the energy release from the pedestal region towards the divertor & first wall during Type I ELMs and the resultant surface effects described in the previous section. To estimate the ELM energy arriving at the divertor we rely on the characterisation of several aspects of Type I ELMs: time scales for the ELM energy flux to divertor PFCs, the area of the divertor subject to ELM transient loads and the asymmetry between the inner and outer divertor ELM energy fluxes. These are determined mostly by infrared measurements with high spatial (~ mm) and time (~100 μs) resolution of the surface temperature of PFCs in present experiments.

4.2.2.2.1. Temporal evolution of the ELM divertor power deposition.

An example of the time evolution of the derived power flux during a Type I ELM at the JET Mk IIGB divertor is shown in Figure 4.2.2-2 [162]. These measurements are typical of experimental results for Type I ELMs in all divertor tokamaks. τ_{IR} is defined as the time required for the surface temperature to rise from 10% to 100% of the total increase during the ELM [162] (390 μs in Fig. 4.2.2-2) which typically lasts ~ 0.1 − 1 ms in present experiments.

A small, pre-ELM, increase of the power flux to the divertor is frequently observed over relatively long time scales (larger than 1 – 2 ms) in JET and DIII-D [162, 163] and not discussed here, being not very relevant to the issues discussed in 4.2.2.1 for ITER. The total duration of the ELM power flux is indeed much longer than τ_{IR}, with significant power fluxes arriving at the divertor during time intervals of several ms after the maximum power flux has been reached (i.e., after τ_{IR}).

The total amount of deposited energy due to the ELM, ΔW_{ELM}^{target}, can be estimated by integrating the power during an ELM that exceeds the inter-ELM value, as shown in Figure 4.2.2-2. Using this procedure the divertor ELM energy flux can be separated into two parts : a) the ELM energy that reaches the divertor in short timescales (i.e., $[0, \tau_{IR}]$), which is most important for evaluating divertor erosion by ELMs in ITER and b) the ELM energy which reaches the divertor in longer time scales (i.e., $\sim [\tau_{IR}, \sim \tau_{IR} + 3ms]$), which contributes to the total energy loading of the divertor by ELMs but not to the peak surface temperature rise and, thus, proximity to the threshold for material damage (section 4.2.2.1). The ratio of the divertor ELM energy flux in short timescales to the total divertor ELM energy flux estimated in this way is typically in the range 15 - 40% for a series of JET Type I ELMy H-modes [31, 164], as shown in Fig. 4.2.2-3. This ratio is seen to depend on pedestal plasma collisionality, which is correlated with the total ELM energy loss from the bulk plasma and the dominant transport mechanism for ELM energy flux out of the confined plasma (convection versus conduction) as discussed in Sects. 4.2.2.4 and 4.2.2.5.

The characteristic timescale τ_{IR} of the ELM power deposition at the (outer) divertor target is well correlated with the transient time of fast ions to flow along the field line from the pedestal to the divertor target ($\tau_{\parallel}^{conv} = 2\pi R q_{95}/c_{s,ped}$, where $c_{s,ped}$ is the sound speed calculated with pedestal plasma parameters). This is shown for Type I ELM measurements from JET, ASDEX Upgrade, JT-60U and MAST in Figure 4.2.2-4 [165, 14, 166, 167, 31].
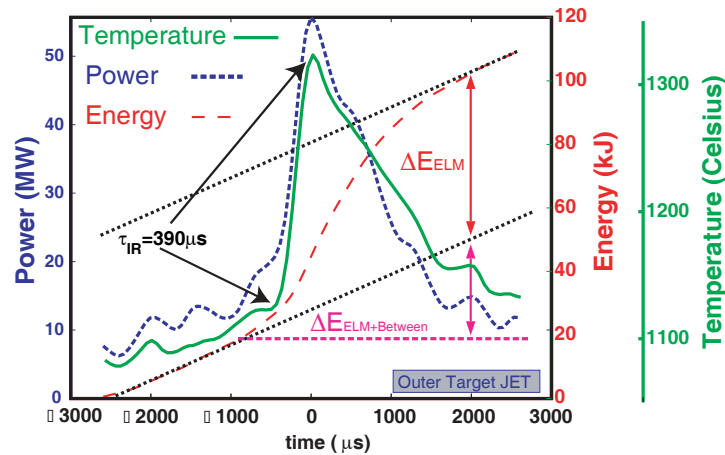

Figure 4.2.2-2. Temporal evolution of the divertor surface temperature, deposited ELM power and energy onto the JET outboard divertor target for a typical Type 1 ELM [162].
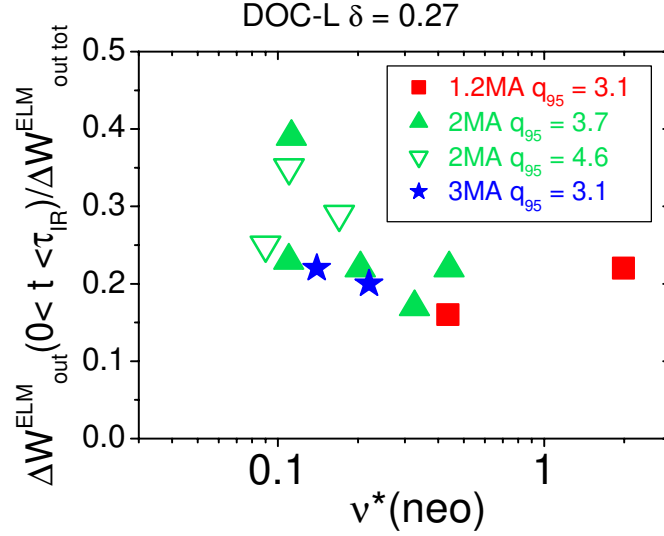
Figure 4.2.2-3. Proportion of the ELM energy arriving at the outer divertor in the time interval $[0, \tau_{IR}]$ (i.e., ELM start to the time of maximum surface temperature) with respect to the total ELM outer divertor energy versus pedestal collisionality for a range of Type I ELMy H-modes at JET [164].

The good correlation between τ_{IR} and $\tau_{\parallel}^{conv}$ is in agreement with PIC-simulations [168, 169], in which the sheath plays a major role in limiting the energy flux from the pedestal plasma to the divertor during the ELM power pulse. This physics picture has been further documented by ELM-resolved Langmuir probe measurements in various divertor tokamaks [170, 2, 171, 163] and by measurements of the soft X-ray emission from the JET divertor target [172], which can resolve the different response and timescales for the impact of hot electrons and ions at the divertor target.

Despite the above evidence, it is not possible to rule out an alternative explanation to the sheath model for the correlation shown in Figure 4.2.2-4. The observed correlation may be associated with the change of the main plasma ELM energy loss from being dominated by conduction to being dominated by convection. As discussed in Section 4.2.2.4, with decreasing temperature and increasing density (and $\tau_{\parallel}^{conv}$) the dominant mechanism for the loss of energy from the main plasma due to Type I ELMs changes from conduction (decrease of pedestal temperature) to convection (decrease of pedestal density) [173, 172, 174].
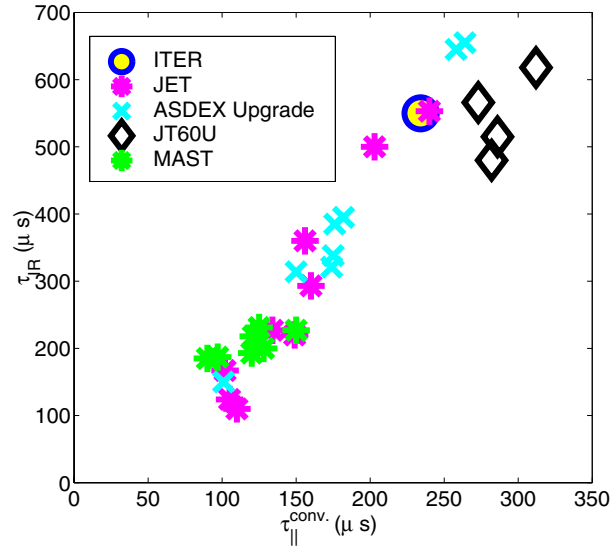
Figure 4.2.2-4. Characteristic timescale of the Type I ELM divertor power deposition τ_{IR} on the (outer) divertor target versus transit time, $\tau_{\parallel}^{conv}$, for various divertor tokamak experiments operating in a range of conditions, calculated for the pedestal plasma parameters [166, 31].

4.2.2.2.2. Spatial characteristics of the divertor target heat flux profiles during ELMs.

Recent experimental results indicate that the ejection of ELM energy from the main plasma is toroidally asymmetric. This toroidal asymmetry is only retained in the divertor target ELM energy flux profile for areas in the far SOL [175]. The maximum ELM energy flux, near the separatrix strike point, remains toroidally symmetric due to the smearing out of the midplane toroidal asymmetries associated with the long connection length of the field lines close to the separatrix [175, 176, 177]. As a consequence, only a small toroidal peaking factor of the divertor ELM power flux of less than 1.5 has been observed in present experiments [178, 166] and a similar range is expected in ITER.

Despite the large increase in radial transport associated with the ELM event, the poloidal footprint of the ELM power flux at the outer divertor does not show a significant broadening when compared to the inter-ELM power flux profile at the divertor [179, 2, 31, 180]. A histogram summarising the results of a statistical analysis of the ELM power width (characterised by the full width at half maximum) at the outer divertor during the ELM is shown in Fig. 4.2.2-5 for JET and ASDEX Upgrade [31]. Therefore, the large increase of radial transport at the ELM is accompanied by a large increase of the transport along the field line. For attached conditions, the inter-ELM width of the divertor power flux is simply correlated with the SOL power e-folding length at the midplane. Therefore, the lack of broadening of the power flux during the ELM at the outer divertor can be directly correlated with a lack of broadening of the ELM power flux at the midplane of the device. For the inner divertor, which is usually detached in most experiments, the above description breaks down and large differences in the shape of the inter-ELM/ELM power deposition profiles are observed. Because the inter-ELM power flux width at the divertor changes dramatically with

the state of the divertor (attached/detached), it is best to extrapolate from present experiments to ITER using the ratio of the ELM SOL power flux width to the inter-ELM SOL power e-folding length. Both can be obtained from divertor measurements provided that the divertor plasma is in attached conditions.
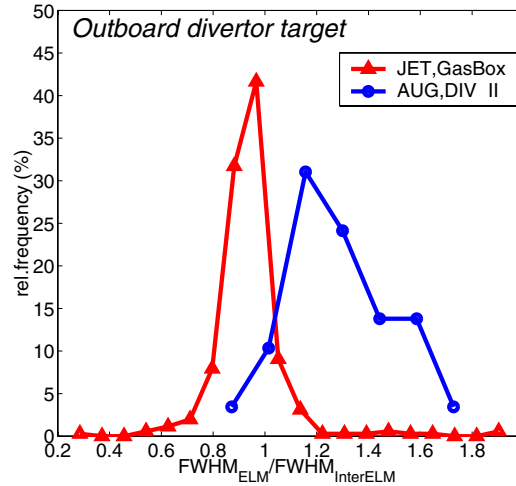

Figure 4.2.2-5. Histogram of the full width half maximum (FWHM) ratio of the target heat flux profiles during and between ELMs for a range JET and ASDEX Upgrade Type I ELMs [31].

4.2.2.2.3. In/out ELM energy flux asymmetries and total divertor ELM energy flux.

The asymmetry of heat deposition during ELMs between the inner and outer divertors is dependent on a number of plasma characteristics. For double null diverted plasmas the ELM energy predominantly flows to the outer divertor [181, 182], demonstrating that the ELM energy preferentially crosses the separatrix at the outer section of the plasma. This is in agreement with the peeling-ballooning picture for the ELM trigger [183, 184]. On the other hand, for single-null plasmas, most experiments show that Type I ELMs tend to deposit their energy preferentially at the inner divertor [178], although variations of this asymmetry with experimental conditions can be large. For single null discharges, recent experimental evidence [31] indicates that the in/out ELM energy deposition asymmetry depends on the size of the ELMs and/or divertor plasma conditions, with the asymmetry being largest for the smallest ELMs and the higher densities [2, 185, 31] where the degree of detachment of the inner divertor is increased. These measurements thus indicate that the conditions of the divertor between ELMs play an important role in determining the energy flux to each divertor during ELMs, as expected if the plasma sheath plays a major role in determining this flux. However, we cannot again rule out that the change of the in/out ELM energy deposition asymmetry is influenced by the ELM energy loss from the main plasma changing from being dominated by conduction to convection (see Sec. 4.2.2.4), or by changes in the peeling-ballooning nature of the ELM trigger [184, 186].

Analysis of divertor ELM energy flux measurements in JET and ASDEX Upgrade shows that not all of the energy lost by the main plasma during ELMs reaches the divertor [2, 162]. Up to ~ 50% of the main plasma ELM energy loss is transported outside the divertor region (or flows to the divertor in time scales much longer than ~ 3 ms), as shown in Figure 4.2.2-6 for a series of JET Type I ELMy H-modes [31]. For the larger ELMs, which can lead to a loss of energy from the main plasma that amounts to up to 15% of the pedestal energy, the missing ELM energy at the divertor can be up to ~ 50% of the total main plasma ELM energy loss, with the proportion of missing energy decreasing as the normalised ELM size decreases. From these experimental measurements it is not possible to determine where the missing ELM energy is deposited, but evidence from other diagnostics, which is reviewed in the next section, indicates that this energy is deposited on plasma facing components in the main chamber of tokamak devices.

4.2.2.3. Interaction of Type I ELMs with the Main Chamber Plasma Facing Components.

Results from fast diagnostics near the outer midplane of most current tokamak experiments indicate that particles ejected from the pedestal during ELMs propagate in the SOL to large radial distances from the pre-ELM separatrix location. Such behaviour during Type I ELMs has been reported by DIII-D [187, 83], ASDEX Upgrade [188, 189], JET [190, 191, 192], and JT-60U [193]. Similar behaviour may be occurring for Type-III ELMs in MAST [181] and TCV [171]. An example of the SOL density profile evolution during Type I ELMs in DIII-D is shown in Fig. 4.2.2-7 [187]. The spatial characteristics of the ELM density perturbation seem to retain those of the ELM trigger, as determined by the peeling-ballooning ELM model [183, 184]: the perturbation has a ballooning character as determined by reflectometry measurements in ASDEX Upgrade [189] and it interacts with the main wall in a poloidally/toroidally asymmetric way with an approximate n-number ~ $10 - 15$ [190, 175].

The typical radial propagation velocity of the plasma ELM density perturbation in the SOL is of the order of v_r ~ 1 km/s in all divertor experiments/ELM types [83, 191, 180, 194]. This leads to an ELM radial propagation timescale of ~ 100 μs, which is similar to the timescale for parallel transport in the SOL during ELMs, as discussed in Sec. 4.2.2.2.1. The observed ELM radial propagation velocities are of a size compatible with those expected from a model for the propagation of "blobs" [195, 196] in the SOL [194, 83] but no detailed quantitative comparisons, with this or other model, nor a systematic study of the dependence of the radial velocity on experimental conditions has been established so far.
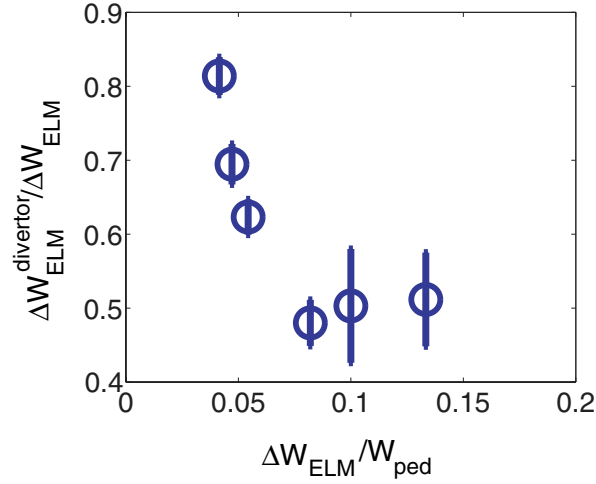
Figure 4.2.2-6. Ratio of the ELM energy deposited on the divertor to the energy loss from the main plasma versus normalised main plasma ELM energy loss (to the total pedestal plasma energy) [31].
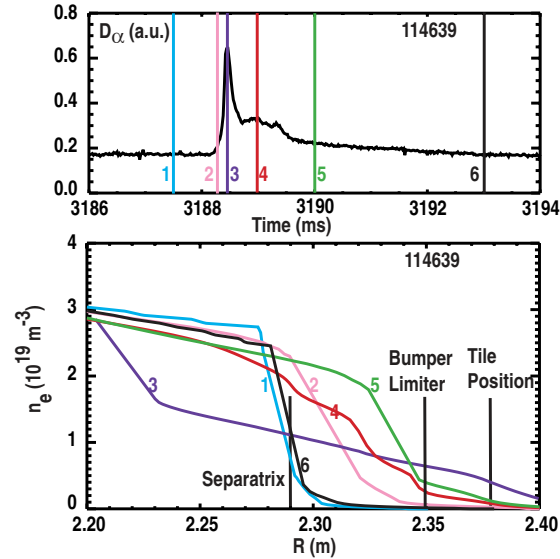

Figure 4.2.2-7. (a) Evolution of the divertor D_α signal during a Type-I ELM in DIII-D and (b) the corresponding profiles of electron density at the outer midplane. The steep pre-ELM density gradient (curve 1) is lost at the time of peak D_α emission (curve 3) and substantial density is observed in the far SOL up to the limiter surfaces [187].

Associated with the large particle fluxes to the main chamber during ELMs, a significant energy flux on the main chamber plasma facing components has been measured in ASDEX Upgrade [188] during Type I ELMs, as shown in Figure 4.2.2-8. Measurements of power flux to PFCs in the main chamber and of the electron temperature and density in the far SOL during ELMs [188, 83, 194, 197] are consistent with the energy flux onto main chamber PFCs being associated with the convective radial transport of ion energy. Pedestal ions reaching first wall surfaces do not appear to lose much of their energy either to electrons or to the divertor target [194, 188].

Simple extrapolations of experimental data indicate that significant ion energy fluxes could be deposited during ELMs in the main chamber PFCs of ITER, in a similar range to

those seen in present experiments (i.e., 20 – 50% of the main plasma ELM energy loss) [188, 194]. This result is tentative at present. However, the implications for the lifetime of main chamber components could be considerable. As a consequence, the experimental determination of the Type I ELM energy and particle fluxes on the main chamber of divertor tokamaks and their dependence on plasma parameters are presently areas of active research in all divertor devices.
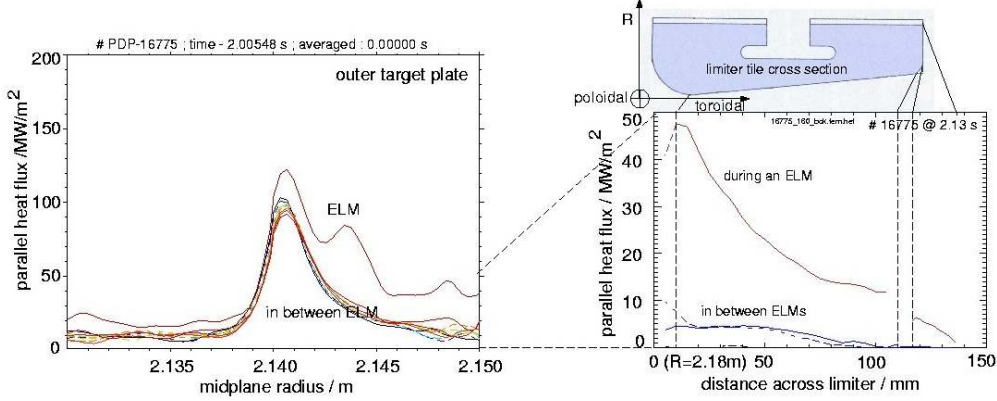

Figure 4.2.2-8. Parallel heat flux profiles on the ASDEX Upgrade outer divertor target (a) and on an outer midplane limiter tile (b) between and during ELMs. The heat flux during ELMs on the limiter at R=2.18 m (~2.5 $\lambda_{ne}^{pre-ELM}$) is comparable to that in the far SOL region of the targets (R=2.145 - 2.150 m or 0.4 - 0.6 $\lambda_{ne}^{pre-ELM}$). The peak midplane heat flux during ELMs is within a factor of 3 of the peak target heat flux [188].

4.2.2.4. Mechanism of Type I ELM Energy Transport to PFCs.

The loss of energy from the main plasma during Type I ELMs can be divided into two components: conductive losses (due to the decrease of the electron and ion temperatures in the pedestal region) and convective (due to the decrease of the plasma density). These two mechanisms depend on the characteristics of the pedestal plasma in different ways. With increasing pedestal plasma density and collisionality, the normalised conductive losses decrease strongly, while the convective losses remain largely unchanged [172, 198], as shown in Figure 4.2.2-9. The different transport mechanisms that affect the main plasma energy losses are also involved in the transport of energy from the core plasma to the PFCs during the ELMs.

The phase of a Type I ELM during which the decrease of density and temperature in the pedestal region takes place is characterised by strong broadband MHD activity. During this phase a large flux of electrons with energies typical of the pedestal plasma reach the divertor target, as measured by their Bremsstrahlung emission on impact at the target [192]. This indicates that the pedestal plasma comes into direct contact with the target along the field lines. The flow of particles to the divertor target takes place on a different time scale, dominated by the ion transport, which governs the convection of energy from the main plasma to the divertor target. This separation of timescales and mechanisms for energy transport has

been confirmed experimentally in several divertor tokamak experiments [172, 199, 166, 163, 171]. An example of such timescale separation is shown in Fig. 4.2.2-10 [164] for experiments in JET, and is reflected in the lack of correlation between the duration of the Type I ELM energy flux pulse at the divertor target and the duration of the strong MHD broadband ELM phase [172, 2, 162].

Observations in existing experiments are consistent with the following transport mechanisms playing a major role during Type I ELMs, although a quantitative evaluation of their importance and their overlap in time remains to be done:

a) In the initial phase, due to the strong MHD activity, the plasma in the pedestal region becomes connected with the divertor target through some unknown mechanism. Due to their large velocity, high-energy electrons from the pedestal arrive almost instantaneously [172, 163, 164]. During this phase electron conduction is expected to play a major role in the transport of electron energy from the pedestal to the divertor target possibly being limited by the formation of a high energy sheath [168]. The duration of the large ELM energy flux to the divertor (τ_{IR}, Section 4.2.2.2.1) is usually longer than the MHD phase indicating that either the high energy sheath is effective at limiting the plasma losses along the field [199], or that the ion power flux to the divertor in the initial ELM phase is comparable in magnitude to the electron ELM energy flux.

b) The second phase of the ELM energy flux to the divertor is dominated by an increased particle flux, and occurs over timescales much longer than that of the MHD phase, extending after the collapse of the pedestal region during the ELM. During this phase no high energy electrons are observed to reach the divertor target. The transport mechanism which dominates this phase is thought to be plasma convection associated with the ELM-enhanced particle flux to the divertor [166, 163, 164].

As seen from figures 4.2.2-9 and 4.2.2-10, the relative importance of the above two phases and of the transport mechanisms which determine the ELM energy flux to the divertor and its time scale seem to be dependent on the pedestal plasma parameters before the ELM. As the pedestal density/collisionality is increased, the energy deposited in the divertor varies from short timescales, dominated by conduction, to longer timescales, dominated by convection [165, 163, 31].

The transport mechanisms carrying the ELM energy to main chamber PFCs are more uncertain. Present experimental evidence indicates that the dominant mechanism is convection of ion energy associated with the fast radial propagation of the plasma density perturbation caused by the ELM [194]. In order to confirm this hypothesis, more detailed measurements of the convective ion energy flux are needed.
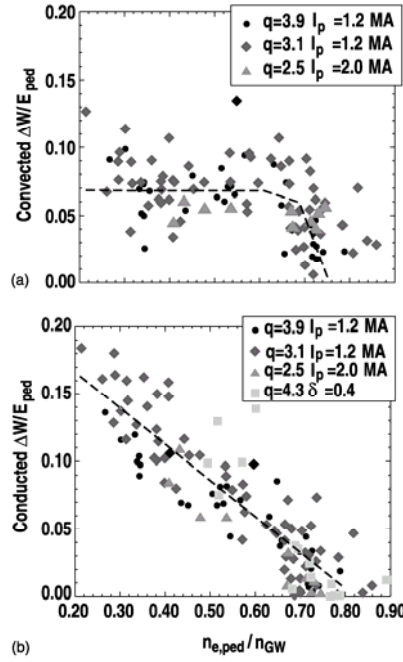
Figure 4.2.2-9. a) The normalized convected ELM energy as measured by Thomson scattering versus the pedestal density normalised by the Greenwald parameter, n_{ped}/n_{GW} in DIII-D. b) The normalised conducted ELM energy versus the normalised pedestal density in DIII-D. A dashed line has been added to guide the eye [198].

4.2.2.5. ELM energy losses in present experiments and potential physics for scaling to ITER.

The previous sections provide a description of the temporal and spatial characteristics of the ELM energy pulses on PFCs and of the transport mechanisms that are involved in carrying the energy from the confined plasma to the PFCs during an ELM. This physics basis allows the extrapolation of these characteristics to ITER, namely the area of the PFCs over which the ELM energy flows and its temporal waveform, but not of the absolute magnitude of the ELM energy flux itself. This extrapolation requires the comparison of absolute ELM energy losses from the main plasma in relevant divertor tokamaks in order to identify the size scaling of these losses and the physics basis for their extrapolation to ITER. The pedestal requirements (see Sec. 2.5.2), combined with the ELM transport in the SOL and divertor (Sec. 4.2.2.2) and the material limits of the divertor PFCs (Sec. 4.2.2.1) lead to a maximum ELM size that a tokamak divertor target can tolerate. For ITER this limit is 5-10% of the pedestal energy [155]. The uncertainty of this limit is due to the SOL and divertor ELM transport issues described in the previous sections.

Initial studies of ELM energy losses [15] concluded that, in order to compare ELM size across devices and configurations and to project to future tokamaks, the energy lost at an ELM should be normalised to an estimate of the bulk plasma energy which is potentially accessible to expulsion by ELMs. This is usually characterised by the pedestal plasma energy,

which is the total pedestal pressure, ions plus electrons, times the plasma volume [15]. These initial studies have been further pursued by enlarging the original database and including ITER-relevant Type I ELM energy loss data from a number of tokamaks [166]. The normalized ELM energy from this data set is plotted versus the pedestal collisionality in Fig. 4.2.2-11. This figure illustrates the generally observed trend that ELM size decreases with increasing pedestal density and decreasing pedestal temperature [172, 173]. The present database also suggests that at the low pedestal collisionality required for ITER, current tokamaks would project an ELM size that is 2-3 times the tolerable limit for the divertor. Although pedestal collisionality is a good ordering parameter for the ELM energy losses across devices, it is not clear at present whether the pedestal collisionality is the relevant parameter to extrapolate ELM energy losses to ITER or not, as the detailed physics mechanisms which lead to these losses have not been precisely identified. For example, measurements from JT-60U [200], ASDEX-Upgrade [174] and JET [164] indicate that Type I ELMs with significantly less energy than the trend shown in Fig. 4.2.2-11 and similar pedestal collisionality are seen in present devices in some experimental conditions.
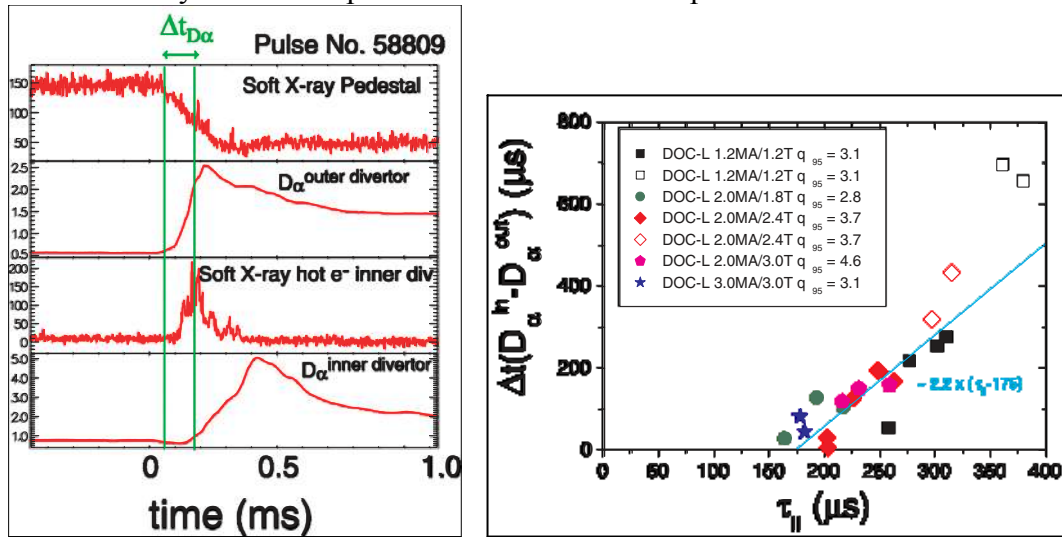

Figure 4.2.2-10. a) Measurements with high time resolution (~ 4 μs) of the soft X-ray emission pedestal collapse, outer divertor D_α emission, inner divertor X-ray Bremsstrahlung (from hot electron impact) and inner divertor D_α emission during a Type I ELM in JET showing the delay between the rise of the D_α emission at both divertors ($\Delta t_{D\alpha}$) and between the hot electron pulse and D_α emission at the inner divertor. b) Delay between the D_α rise at the inner divertor (with respect to the outer one) versus parallel ion transit time calculated with pedestal plasma parameters for a large range of H-modes in JET [164].

There is some evidence that Type I ELM regimes which are compatible with a reasonable lifetime of ITER PFCs may be possible. These are the Type I ELMs that exhibit only convective losses, which have been denominated "Minimum Energy Type I ELMs". These minimum energy ELMs are of a size, < 5%-10% of the pedestal energy, that may be tolerable in an ITER-size tokamak but are generally found at too high pedestal collisionalities for

successful ITER Q_{DT} =10 operation. More recently, experiments at JET have demonstrated that the reduction of ELM energy loss is correlated to the reduction of the conductive losses in Type I ELMs at any collisionality by achieving small convective ELMs in conditions of low pedestal collisionality as well [164]. Unfortunately, it has not yet been possible to unambiguously determine which parameters are responsible for these small ELMs in order to predict their operational space in a large tokamak such as ITER.
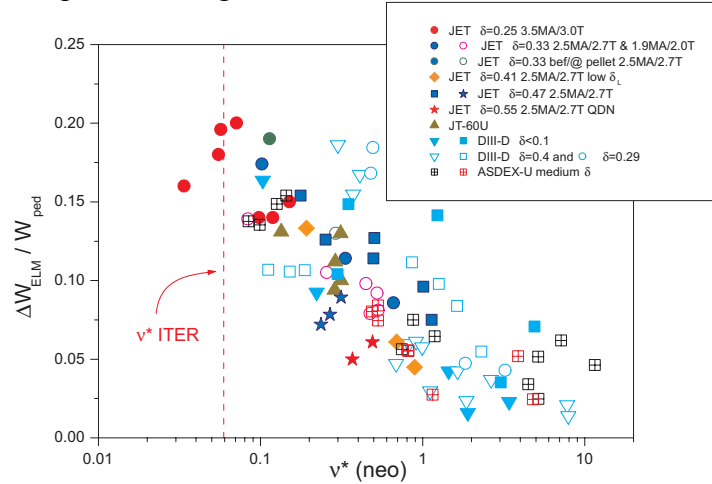

Fig 4.2.2-11. ELM energy normalized to the pedestal energy versus pedestal collisionality. The multi-machine data collected by the ITPA Divertor Group includes density scans as well as varying configurations [166].

The physics of how the ELM energy reaches the divertor and wall is still too uncertain to predict the time dependence of the heat pulse reaching those surfaces. Further work is needed in acquiring a detailed model that can follow the evolution of the ELM instability into its non-linear phase, where transport is expected to occur (e.g. [201]) and thus explain how energy crosses the separatrix. Experiments to discriminate whether the plasma physics or the atomic physics, through recycling, determines the scaling of the pedestal and ELM size should provide significant insight for operation in future tokamaks. If plasma physics sets the pedestal and ELM size then it is likely that the low collisionality of ITER will result in very large Type I ELMs. However, if atomic physics is playing a significant role, such as narrowing the pedestal width, then smaller, tolerable Type I ELMs in ITER may be possible.

In addition to the Type I ELM regime, several other operational modes that exhibit a robust edge pedestal with no, or small, ELMs have been identified in current tokamaks (See Sec. 2.4.8). It is unclear if any of these regimes will prove applicable at the parameters and constraints envisioned for a future large tokamak such as ITER. It is important, however, to continue investigating these regimes as an alternative in case the Type I ELM regime proves to be incompatible with the ITER divertor.

4.2.2.6. Ability of radiating plasmas to buffer ELMs.

Ideally, radiation can be used to remove energy from an ELM before it reaches first wall surfaces. Our present understanding of so-called ELM "buffering" is that it is fairly limited in usage, primarily effective with small, Type III ELMs. For example, recent experiments with nitrogen seeding and deuterium puffing in JET [144] have demonstrated full detachment between Type III ELMs, in agreement with previous JET results [202]. For these conditions, radiative dissipation of the ELM energy is observed for radiative power fractions above 80%, in agreement with observations in CD-H mode experiments in ASDEX Upgrade [203].

Radiative dissipation of the more ITER-relevant, Type I ELMs, in present experiments has not been as successful. Nitrogen or argon impurities have been injected into such JET plasmas, with ΔW_{dia} up to 500 kJ, achieving radiative fractions of ~ 55% [204]. However, the energy delivered to the target plate ($\Delta W_{target}/\Delta W_{dia}$) is only marginally reduced (by 18 - 24%) compared to non-seeded operation [204]. Plasma edge modelling of ELM transient radiation is in agreement with the small effect of buffering the JET Type I ELMs [204]. Previous calculations with B2-Eirene for ITER [205] also predicted that a significant effect could only be obtained for very small ELMs in ITER ($\Delta W_{dia} < 0.6MJ$).

An additional effect providing buffering of Type I ELMs could take place through the modification of the ionisation processes occurring during the ELM burst. This leads to a decrease of the D_α divertor emission at the ELMs (so-called "negative" ELMs) [202, 206]. The effect has been studied in linear divertor simulators [207, 208, 209, 210]. Unfortunately, no significant energy loss is expected due to this process, both because of the small potential for radiation of the hydrogen atom and because re-ionisation of a recombining plasma would tend to increase the power flux to the divertor, as the energy of hydrogen recombination would be deposited on the divertor target surface rather than being radiated away by the recombination radiation.

4.2.3. Neutral Processes and implications for the divertor and SOL.

The control of neutrals in fusion devices is important for the plasma performance in these devices. Significant divertor pumping must be achieved both for control of core fuelling and of He ash removal. This favours maximizing the divertor pressures for those species. In addition, one wants to minimize neutral densities in the main chamber in order to minimize the erosion of the main chamber plasma facing components (by charge-exchange sputtering, chemical erosion, etc.). Such eroded impurities lead to a reduction of the lifetime of in-vessel components and to core plasma contamination, as impurities produced in this interaction have a higher probability of penetrating to the main plasma than those generated at the divertor (see Section 4.2.4).

The understanding and prediction of neutral densities in the divertor and main chamber requires a mixture of physics understanding (e.g. recombination, neutral-neutral collisions)

and understanding of the role of mechanical structures, whose progress is reviewed in this section. The results herein refer to single-null diverted plasmas unless otherwise noted.

4.2.3.1. Neutral Pressure Control.

Divertor geometries and openings have been modified on a number of tokamaks to enhance divertor closure and thus reduce the leakage of neutrals out of the divertor. Divertor closure is influenced by the divertor plasma parameters through their effects on the ionisation mean free paths but also by the conductance of neutrals through and past the divertor structure to the main plasma chamber [69]. Experiments in many divertor tokamaks have shown that increasing the divertor closure has led to larger divertor neutral pressures [211, 212, 179, 62, 213], as shown in Fig. 4.2.3-1.a and 4.2.3-1.b for the JET divertors.

In general, the predictions with respect to the behaviour of deuterium neutral and recycling impurity exhaust by edge modelling codes have been confirmed by the experiments in tokamaks. In particular, the dependences of the neutral particle and impurity exhaust on the details of the divertor geometry and on the local magnetic flux surfaces have been confirmed [214, 69, 215, 65, 216, 217]. The neutral pressure in the pumping plenum can be very sensitive to the exact location of the divertor strike point [69, 215, 216] when the neutral transport is kinetic (termed 'ballistic'). For conditions in which the neutral collisional mean free path (C-X and elastic collisions), λ_{MFP}, is short compared to the divertor dimensions (d) and ionisation length, λ_{IONIS} ($\lambda_{MFP}/d < 1$, $\lambda_{MFP}/\lambda_{IONIS} < 1$), the neutral transport is diffusive and the dependence of divertor pumping on strike point position is much weaker [69, 214, 65, 218]. Next-step tokamaks, such as ITER, will have much smaller λ_{MFP}/d compared to current experiments. Therefore, the research in this field is focused on validating the modelling codes with experiments in present devices in conditions, as close as possible, to these ITER divertor conditions. The effect of double-null operation on pumping has received much less attention (e.g. [219]).

The major uncertainty remaining in modelling the neutral pressure in ITER-like devices concerns processes, which occur to a much lesser extent in present experiments but are likely to dominate the neutral dynamics in ITER. These include neutral-neutral collisions (viscosity), trapping of Lyman series radiation (of which Ly_α is the principal component), and neutral elastic collisions (friction). These processes were all shown to play an important role in modelling the Alcator C-Mod experimental divertor pressures [220]. The Alcator C-Mod divertor plasma is closest in λ_{MFP}/d and n_e of all tokamaks to ITER neutral collisionality and absolute plasma density. Including a proper modelling of these effects, the modelled pressures were (lower than but) within a factor of 2 of the experimental measurements. Previous modelling, which did not include any of the processes important in the ITER divertor described above, showed a disagreement by more than an order of magnitude between the modelled pressure (too low) and experimental measurements [221]. Further work is in

progress to improve the modelling of neutral interactions and evaluating their effect on ITER divertor performance [222] and of the radiation transport in these conditions (including Ly_α trapping) [223].

a)

b)

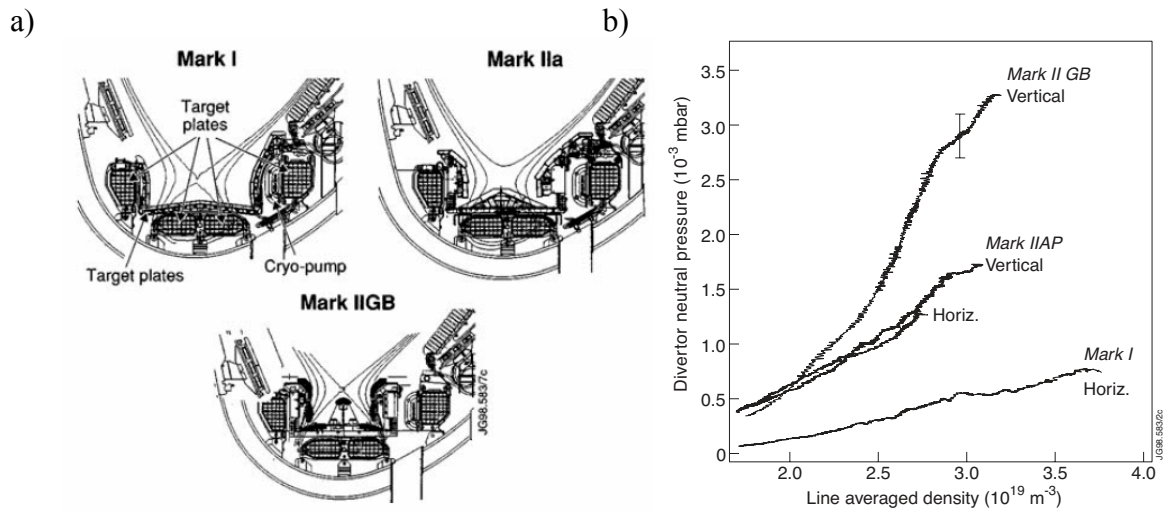*Figure 4.2.3-1. (a) Diagram of the three divertor geometries explored in JET. Divertor closure was increased in going from Mk I → Mk IIA → Mk II Gas Box. During the exploration of Mk IIA, the conductance of the by-pass leaks was reduced (these divertor experiments are referred to as Mk IIAP which stands for Mk IIA with plugged divertor leaks). (b) Measured neutral pressure at the divertor cryo-pump for similar JET L-mode discharges in the divertor geometries in (a) [211].*

Detachment of the divertor leads to a saturation or slower increase of the divertor deuterium neutral pressure with increasing density [202, 214]. This saturation/slower increase of the deuterium neutral pressure is associated with changes in the neutral source and transport caused by plasma detachment [69, 214]. For conditions in which the neutral mean free path is larger/comparable to the dimensions of the divertor plasma in detached conditions, neutrals escape is favoured by plasma detachment and a saturation of the neutral pressure with detachment is observed [69]. For conditions in which the neutral mean free path is smaller than the dimensions of the divertor plasma in detached conditions, such as in Alcator C-mod, detachment is associated with a reduced neutral mean free path. Therefore, in those conditions, the escape of neutrals from the divertor is similar to or smaller than in high recycling conditions and the divertor neutral pressure increases with plasma detachment [214]. This last behaviour is the one expected for next step devices because the divertor plasma will be opaque enough to neutrals even in partially detached conditions.

The control of main chamber neutral pressure by divertor geometry remains an area of active research and no quantitative conclusion on the extrapolation from present results to ITER has been reached so far. Several experiments have shown [69, 211, 70, 215] that decreasing the divertor chamber conductance to the main chamber can decrease the main chamber neutral pressure, while others have found little or no effect [212, 64]. One explanation, gaining support, is that the source of neutrals in the main chamber is a

combination of divertor leakage and neutral recycling occurring locally [69], the latter due to anomalous radial transport (see section 4.2.1.3). This is supported by Alcator C-Mod experiments varying the conductance between the divertor and main chamber (within one shot) [62], as well as by the de-correlation between main chamber and divertor neutral pressures once the mechanical leakage of the divertor is reduced to sufficiently low values as seen at JET (Mk IIA → Mk IIA/p → Mk IIGB) [211]. Thus the main chamber neutral density has some irreducible minimum determined by anomalous radial transport.

Another effect that remains to be clarified is the effect on neutral control played by the existence of a dome (preventing neutral escape from the divertor through the private flux region) and a septum (preventing direct neutral transport between inner and outer divertors) in the divertor. Modelling for ASDEX Upgrade has shown that the presence of the dome is essential for explaining the increase of the neutral divertor pressure in the modification from the Div I to the Div II divertors [65]. However, recent experiments at JET have shown that the effects of the dome and septum on the divertor neutral pressure distribution and the control of in/out asymmetries are much smaller than initial experiments with dome and septum had anticipated, at least for plasma configurations with the x-point close to the dome [224, 69, 225, 226]. The reason for this unexpected result is being presently studied.

The findings described so far in this section are "ELM averaged" when they concern ELMy H-modes. ELMs are seen to modulate the divertor pressure noticeably, particularly at low plasma densities/low ELM frequencies [227]. At higher plasma densities, which are associated with the higher frequency Type I ELMs, the modulations of the neutral pressure at the main chamber and divertor due to ELMs are smaller (see Fig. 14 in [228]) and, thus, the "ELM averaged" neutral densities are adequate to describe the neutral pressure in these conditions. With increasing machine size, the time constants associated with the size of the divertor and associated pumping plenum become longer. When the ELM frequency becomes high enough (time constant shorter than the divertor pumping time constant) it may lead to a smoothing out of the effects of ELMs [227]. Due to divertor lifetime considerations (see Sect. 4.2.2), ELMs in full performance regimes to be explored in next step devices, such as ITER, must lead to small main plasma losses (in relation to the total energy/particle content of the plasma), which are typically in the lower range of today's experiments [166]. Therefore, the perturbation of divertor neutral parameters by ELMs is expected to be lower in next step device than in present experiments and the "average" ELM modelling thus reasonably realistic for those.

4.2.3.2. Helium exhaust and noble gas impurity enrichment.
A significant expansion of the database for helium transport and exhaust has been made in recent years for tokamak scenarios with improved confinement, i.e., both for H-modes and discharges with internal transport barriers (ITBs).

The transport of helium from the core to the pumping plenum is commonly characterized by two figures of merit : a) the ratio of helium particle residence time to the energy confinement time, τ^*_{He}/τ_E [229], and b) the ratio of the helium fraction in the exhaust gas to the main plasma helium fraction or helium enrichment factor, $\eta_{He,exh}$. The requirements for reliable ITER fusion performance as well as results showing values of τ^*_{He}/τ_E within that needed for the reference ITER ELMy H-mode regime ($\tau^*_{He}/\tau_E < 5\text{-}10$), are included in the ITER Physics Basis [18]. Recent results from several experiments [230, 231, 232, 233, 234] for the ITER reference H-mode scenario have increased the confidence on the previous extrapolations of experimental results to ITER. As previously reported, the helium exhaust does not appear to be constrained by core transport in ELMy H-modes [235], but is limited by the efficiency of helium transport in the SOL and pumping [231]. More recently, the study of He transport has been expanded beyond the ELMy H-mode to other scenarios. In JT-60U, helium beams were injected into reversed shear plasmas with ITBs, while simultaneously pumping both legs of the divertor region [233]. In plasmas with strong ITBs and, therefore, good core confinement ($H_{ITER-89P} \sim 2.4$), the residence time of helium inside the ITB is about 1.7 times longer than outside the barrier and $\tau^*_{He}/\tau_E \sim 15$. Weakening the ITB by increasing the core density and divertor recycling led to better helium exhaust, $\tau^*_{He}/\tau_E \sim 8$, at the cost of poorer performance ($H_{ITER-89P} \sim 1.2$). A similar result was obtained for a weak ITB at JET, $\tau^*_{He}/\tau_E \sim 5$ [231, 234, 236] with $\eta_{He,exh} \sim 0.4\text{-}0.6$ [237], well within the ITER requirements [18].

The recent improvement in helium removal rates has been obtained both by optimisation of the divertor plasma configuration and by increasing the divertor closure. Helium partial pressures above 0.01Pa were measured following divertor modifications in JT-60U with inner-leg pumping [230] and in diverted corner configurations in the JET MkII-GB divertor [238]. Minimizing the gap between the plasma strike zones and the entrance to the pumping plenum enhances ballistic scattering of He neutrals into the pump [239, 218, 212, 240] and minimises the neutral backflow from the pumping plenum into the divertor [233]. Better closure of divertor mechanical leaks enhances compression of deuterium, helium [232, 240] and argon [241] but appears to have no effect on helium or argon enrichment. Induced scrape-off layer flow by the 'puff and pump' technique did not significantly alter the enrichment of helium [242, 212, 240] but enhanced the neon and argon enrichment in DIII-D [242] and JT-60U [243], although not in ASDEX-U [212] or JET [240]. The reasons for this discrepancy are not yet understood.

The different enrichment behaviour of the noble gases helium, neon, and argon can be understood by the differences in impurity neutral ionisation mean free path, λ_{IONIS}, and the effect of friction and thermal forces (impurity ions). Due to its large ionisation potential, helium is more likely to escape the divertor as a neutral than hydrogenic species or other neutrals (e.g. Ne or Ar) leading to a relatively low compression ratio. This effect is enhanced

under detached divertor conditions and the He/D ratio in the divertor is seen to decrease for such conditions [232, 233, 240]. Neon and argon, are ionised much closer to the divertor target and, therefore, experience the frictional drag force as ions, driving them back toward the target. As a consequence, the enrichment (and compression) increases with increasing noble gas mass and it is usually larger than unity for the heavier species in all divertor conditions [242, 244, 240]. The enrichment of neon and argon increases with increasing density up to detachment [242, 244, 240] after which it drops. However, such an effect is less likely to occur in next step devices because the ratio of λ_{IONIS} to divertor size will be much smaller than in present experiments for all regimes (including detached divertor plasmas).

Integrated modelling of helium transport in the core, edge and pumping plenum using the COCONUT [245], B2-EIRENE [246, 247, 248], EDGE2D [217], and DIVIMP/NIMBUS [240, 249] codes has shown qualitative agreement with experimental observations, which gives some confidence in the modelling predictions for ITER, although further work in this area to refine the predictions is on-going.

Earlier calculations suggested that elastic scattering of helium neutrals by hydrogenic ions could enhance helium atom transport towards the divertor [250, 251]. Experimental measurements have shown that this process mainly heats the helium atoms in the divertor, thus increasing their mean free path [252]. This results in two competing effects : more He atoms can reach the pumping plenum duct and more He atoms can reach the confined plasma. Inclusion of this process in the divertor modelling codes has shown that the efficiency of helium exhaust can be improved by a factor of 3-5 in ITER [253].

4.2.3.3. The role of recombination in divertor processes.

If detached plasma conditions are appropriate, recombination can occur in significant amounts and strongly affect divertor operation. The effects are two-fold: a) recombination reduces plasma flux to the plates. This lowers power flux by removing the internal energy (13.6 eV + 2.2 eV dissociation potential) of each ion-electron pair, thus further reducing divertor power deposition, beyond the drop in T_e associated with detachment, and reducing physical sputtering and b) volume recombination affects divertor performance by strongly changing the ionisation balance across the divertor region. Deuterium recombination has been observed on most diverted tokamaks [254, 255, 256, 257, 206].

The most well-documented recombination process in the experiments has been 3-body recombination, indicative of electron temperatures ≤ 1 eV and electron densities greater than 10^{20} m^{-3} (in some cases $>> 10^{20}$ m^{-3}). For these conditions, radiative recombination rates are relatively small. Another important recombination process, Molecular Assisted Recombination (MAR), has also been identified. Although difficult to study in a tokamak, MAR continues to be of interest because of its potential to increase the recombination rate by orders of magnitude and occur at higher T_e [18]. Estimates of its magnitude, relative to the 3-

body rate, range from 20-30 [258] to ~ 2 for $n_e = 10\, n_{H2}$ [259]. Whereas in linear devices n_{H2} is usually fixed as an external control parameter, in a divertor it is self-sustained and determined by recycling fluxes and molecular transport. In particular the MAR process itself reduces n_{H2} and, thus, the role of this mechanism on divertor dynamics cannot be understood by simply comparing the rate coefficients alone. Indeed recent modelling for ITER, including all relevant neutral/molecular processes, has shown that the effect of MAR is negligible compared to 3-body recombination, for typical divertor conditions [222].

Experimentally, it appears that the role of recombination in plasma flux reduction strongly depends on the plasma conditions. 3-body recombination has been shown in some cases to account for large fractions (> 50%) of the ion sink in the divertor [260, 206] and in the MARFE [261]. However, in some detached plasmas [206, 260, 262, 263], in particular those with high SOL heat flux which detach after impurity puffing [260], recombination appears not to be a significant ion sink. This variation in recombination is due to the strong dependence of 3-body recombination on the local plasma density (n_e^3).

Studies of MAR in tokamaks indicate that its effect is small. Measurements in ASDEX Upgrade show that populations in the molecular vibrational levels required for MAR are only a few percent of the total molecular density [264, 265] and that molecular influxes can be comparable to atomic fluxes [266]. The level of MAR in detached plasmas has been inferred to be in the range 10-50% [257, 267] of the overall recombination rate, similar to the modelling done by Reiter [259]. In fact, inclusion of vibrationally excited molecules in a B2-EIRENE model actually reduced the total recombination rate [267].

The results of recombination and detachment studies using "divertor simulation plasmas" of linear devices [268, 208, 269, 263] show MAR to be much more important for such plasmas. The occurrence of MAR coincident with detachment has been confirmed, in both of its primary pathways, so-called ion conversion [268] and dissociative attachment [270]. In these experiments, which have much higher H_2/H and H_2^+/H^+ ratios than that in tokamak divertors, MAR can dominate radiative and 3-body recombination. These results are, therefore, not necessarily inconsistent with those quoted above for tokamaks, as the plasma conditions in linear devices and tokamak divertors are very different.

Although there is certainly incontrovertible evidence for the importance of recombination (3-body) in current detached divertor tokamak plasmas, the influence of this effect on the divertor performance of next step devices is still uncertain. This requires the improvement of the present modelling codes to include the relevant neutral and molecular processes (including recombination) along the lines of the studies in [222, 220], together with the transport of Lyman radiation in the divertor [223], which will eventually determine the ionisation balance of the divertor in ITER and its performance.

4.2.4 Material Migration.

Material migration studies include erosion of the plasma facing components (Section 4.2.4.1), core contamination by that material (Section 4.2.4.2), and migration to other locations (Section 4.2.4.3) where a separate issue is entrapment of tritium in co-deposited layers (Section 4.2.6). The experimental data base on material migration in tokamak devices has been extended since the publication of the 1999 ITER Physics basis study [18]. Major developments include the discoveries of :

1. Re-deposited carbon films with large tritium retention (Section 4.2.6) following the 1997 JET deuterium-tritium experiment campaign [271],
2. Strong flows in the plasma boundary,
3. High re-erosion of hydrocarbon deposits, and
4. Initial results of migration studies using tracer methods.

At present, the basic mechanisms behind these processes have not been understood sufficiently for confident extrapolation to ITER [272, 273]. A comprehensive 2001 review [274] of plasma-wall interaction physics dealt also with material migration issues. This section outlines the major findings of that review, updated with papers published since 2001. No present-day experiment contains all the features (geometry, materials, particle and power fluxes) expected in ITER, thus making projections difficult.

Different physical processes occur in the divertor and the main chamber :

a) Divertor processes.

In the divertor, the impurity sources are highest near the strike points and can extend along the target plates. Target plate material is released by deuterium induced physical sputtering with additional contributions by chemical sputtering [275, 276] (in case of carbon) and by impurity induced physical sputtering (in case of high Z metals [277, 278]). The initial migration process is prompt re-deposition when the ionising mean free path is of the order of the ion gyro radius making the created ions re-impact the target material in the vicinity of the initial erosion. Prompt re-deposition mitigates erosion rates making the net erosion as much as an order of magnitude lower than gross erosion rates. The effect increases with decreasing ionisation mean free path, either as a result of increasing plasma density or higher Z materials [279]. Impurities migrate for longer distances if they leave the divertor region either as neutral atoms or ions pulled out of the divertor by the thermal force. Impurity ion flow velocities in the range of 20 km/s (out of the divertor) have been observed [120, 280], with the magnitude agreeing with UEDGE calculations [281]. These impurities are eventually deposited at some distance from the strike point. A similar deposition pattern is found for material eroded at main chamber plasma facing components, which can be ionised already in the periphery of the boundary plasma [282]. Carbon can be deposited as hydrogenated amorphous films, which are subject to high re-erosion [283]. By subsequent erosion-deposition steps C can

migrate to remote locations, which are not in direct or line-of-sight contact with the plasma. The entire process depends on the geometry, material composition of the plasma facing components, and the plasma parameters in front of surfaces.

The ITER divertor is designed to retain the emitted carbon near the strike points in a partially detached plasma regime although this cannot be tested experimentally in current machines. Further, the ITER materials combination has yet to be used in existing experiments. Therefore projections to ITER are uncertain and more dedicated experiments are needed [274].

b) Main chamber processes.

In the main chamber, impurities are released from the walls and divertor baffles as neutrals and also enter the main chamber as ions from the divertor. The most basic and unavoidable impurity source in the main chamber is due to impact of neutral atoms created from charge exchange of hydrogen neutrals in the core. Another source of impurities can be created by ion bombardment. Radial transport of ions (Section 4.2.1.3) and/or ELMs (Section 4.2.2.3) can be significant. Both enhance the erosion of main chamber walls [284] and protection limiters in the main chamber [285].

Neutral impurities are ionised in the scrape-off layer some distance from the separatrix. Direct impurity ionisation in the core plasma is only observed in lower density plasma regimes. Impurity ions can diffuse in the edge plasma radially inwards to the core, or radially outwards to the wall. As well, they experience parallel transport along the field lines to the inner or outer divertor legs. Complicating the motion of the impurity ions is the balance of different parallel forces acting on the ions, which can create large SOL flows (Section 4.2.1.4).

4.2.4.1. Intrinsic Impurity Sources.

The dominant impurity source mechanisms depend upon the material used (Section 4.2.5) and on coatings and material mixes due to re-deposition (Section 4.2.5.6). Typically, the dominant impurity sources originate at the outer divertor target and the main chamber walls and limiters. The basic impurity generation mechanisms [274] are:

1) Sputtering of the main chamber walls by neutral particle bombardment. These sources can peak in the vicinity of gas or neutral beam injection ports [286]. Chemical sputtering of carbon walls is usually larger than physical sputtering [275].

2) Sputtering of the main chamber walls by steady state (section 4.2.1.3) or ELM-related (sections 4.2.2.3) ion bombardment. These sources may be concentrated near main chamber components such as protection limiters [285] and at the baffles near the divertor entrance.

3) Increased sputtering of RF antennae and protection limiters by energetic ions due to acceleration in RF rectified sheaths [106, 287].

4) Divertor targets experience the dominant power loading and particle flux, which can lead to strong erosion by sputtering but also to macroscopic erosion processes (melt layer losses, evaporation and sublimation due to heat load transients). For target plates manufactured from carbon based materials, chemical sputtering due to D/T, oxygen, and carbon is an additional important erosion mechanism [288, 289].

5) Devices with high Z target materials often report impurity induced physical sputtering as the dominant cause of material erosion [277, 290; 282]. For high-Z materials, self-sputtering can contribute significantly to impurity induced sputtering processes [291].

6) Unipolar arcing and ion bombardment can occur on start-up limiters and regions of plasma contact and leads to significant erosion along the arc track [292]. There are no quantitative estimates on the contribution of this process to the overall material migration because there are no reliable experimental data on the discharge conditions leading to arcing or on the frequency of arc occurrence.

Some results challenge our understanding and, hence, current models, for example:

1. Molybdenum erosion at the C-MOD outer strike point was attributed to boron induced physical sputtering, even though little boron was observed at the erosion region (Fig. 4 of [278]). Similarly, Tungsten erosion in the ASDEX Upgrade divertor I was attributed to carbon induced sputtering [277]. In the inner divertor, the tungsten became entirely covered by a carbon layer in contrast to the outer divertor where the strike point remained metallic tungsten [293]. Models for these synergistic erosion processes can qualitatively explain the transition between continuous erosion and formation of protective layers, however, only for a narrow parameter range and limited material combinations.

2. The DIII-D carbon erosion at the outer strike point was attributed to physical sputtering by WBC/REDEP simulations [294]. However, a 50% difference between experimental findings and simulation, which also underestimated the erosion by a factor-of-five at distances 5-10 cm from the strike point [295] remains unexplained.

3. Recent JET outer strike point erosion rates [296] are orders of magnitude below earlier results (e.g. Fig. 4 of [295]), and the cause of the difference has not been addressed in the literature.

4. Current thinking is that the net erosion rate experienced at the outer strike point depends upon the carbon influx from the main chamber. In fact, if the outer strike point is detached, then erosion rates drop [107] and the area often becomes a region of net deposition. This phenomenon has not yet been modelled.

In contrast to sputtering, macroscopic evaporation, sublimation and melt layer losses due to heat load transients have not been well-characterized in present fusion experiments. However, such processes are a concern for ITER [273] due to the expected larger ELM energy loss (Section 4.2.2).

4.2.4.2. Core Contamination.

Material eroded from the main wall and divertor enters the main chamber SOL plasma and has a finite probability of being transported into the core plasma before it is re-deposited. This probability depends on parameters such as impurity species, source location, edge and core plasma parameters and cross field transport processes. At the present time, the relative contamination caused by the divertor and main chamber impurity sources can only be inferred indirectly from measurements of fuelling efficiency in the two regions. Gross divertor sources can be larger than wall sources, but the probability of reaching the core is lower.

The core contamination on DIII-D was attributed to the main chamber as evidenced by the decade long reduction of the divertor carbon light emission, without a corresponding reduction of the core carbon content [297]. A similar de-correlation of Mo sources and contamination was observed in C-MOD [106]. In JET [298] and ASDEX Upgrade [299], when the carbon divertor was replaced by a beryllium and tungsten divertor respectively, the change did not affect the carbon core concentration. However, recent spectroscopic analysis with improved diagnostic capability at DIII-D indicates that additional sources exist at the divertor baffle regions [300]. Similarly, correlations of the temporal evolution of the molybdenum core contamination with Mo sources in Alcator C-Mod [290] showed that for ICRF-heated cases the main chamber sources were dominant.

Measurements of impurity fuelling efficiency.

Several experiments have quantified impurity fuelling efficiencies [287, 301, 302, 298, 290]. Typically 5% of carbon injected as methane at either the JET outer mid-plane or vessel top reached the separatrix. Slightly smaller values are measured by laser ablation for tungsten for source locations both at the high- and low-field side of the plasma [303]. For tungsten, the comparatively small ionisation length means that tungsten ions need to diffuse a longer radial distance across the magnetic field in order to contaminate the core plasma.

From the divertor region, a smaller fraction, typically of order 1% reaches the separatrix. For tungsten, this fraction is smaller due to larger prompt re-deposition at higher Z [304]. Both Monte-Carlo transport modelling (DIVIMP [301]) and fluid modelling (UEDGE [305]) show that impurities escape the divertor as ions accelerated by the thermal force. Core contamination in both models is simulated by assuming ad-hoc cross-field diffusion coefficients (Section 4.3.6).

In ITER, impurities will be ionised further from the separatrix potentially allowing more time to flow to the divertor as opposed to diffusing towards the separatrix. For accurate

predictions, the scaling of cross-field diffusion and turbulent intermittent transport in the SOL will need to be fully characterised.

4.2.4.3. Impurity Migration.

Eroded wall material will generally not be redeposited locally but migrate to other locations due to long range plasma transport processes. Formation of redeposited layers due to such migration processes is observed in all divertor tokamaks but clear examples of carbon deposition have also been observed in limiter machines such as in long duration Tore Supra discharges where co-deposited layers grew with rates of up to 20 nm/s [306]. The particular case of hydrocarbons, which can locally migrate into castellations, to sides of tiles, and to other remote areas of the divertor is discussed in section 4.2.5.2.4.

The main chamber is a zone of net erosion [278, 271, 307], while the inner divertor target area is a zone of net deposition. Wall material is observed to preferentially migrate to the inner divertor with examples such as boron in C-Mod [278], beryllium in JET [271, 308], ^{13}C from methane puffing in JET [309]. However, migration to both the inner and outer target is found in ASDEX Upgrade for tungsten [292] and for ^{13}C from methane puffing at the outer mid-plane [310]. ^{13}C methane techniques have promise since fixed plasma and divertor conditions can be maintained, and quantitative migration can be determined, thus aiding the modelling. However, results are just now being analyzed and the use of such data to benchmark codes for projections to ITER has not yet been done.

The outer divertor target was a region of net erosion in JT-60U [311], DIII-D [107], ASDEX Upgrade divertor I [312] and C-Mod [278] and small net erosion/deposition on JET [296]. The outer strike point became a region of net deposition on DIII-D during detached operation [107]. In ASDEX Upgrade the DIV IIb outer divertor baffle is also a region of erosion [307], but clear experimental evidence does not yet exist for the strike point zone.

Directed SOL flows have been observed [111, 313, 114] and are presumed to influence the preferential deposition at the inner target. JET reverse field experiments reduced the SOL flow, creating a stagnation point at the vessel top [27]. Infrared measurements indicated that surface layers were built up on the outer target during reversed field operation pointing towards increased deposition there, reversing roles with the inner divertor (forward field). Apart from the SOL flows, the observed erosion asymmetry between divertor plates could also result from differences in the balance of erosion and re-deposition. The inner divertor plasma is often detached and generally cooler than the outer divertor. Therefore, the re-erosion of deposited material might be different in the inner divertor. A similar explanation was reported from EDDY modelling of JT-60U erosion/deposition [314]. A difference in the inner and outer target temperatures due to the different power loading induced changes in the chemical sputtering rates so the inner target was a deposition region even though the model did not have a strong SOL flow. Measurements of tungsten deposition [292] show smaller

differences between inner and outer divertor compared to results for carbon [307]. This can be attributed to the small re-erosion rate of tungsten even in the outer divertor where carbon would be re-eroded.

Attempts to establish a total balance of erosion and re-deposition have been pursued at JET for carbon [315] and at ASDEX Upgrade for tungsten [282]. The overall carbon deposition in the JET Mk-IIA and Mk-IIGB configuration during their divertor operation time of 19 and 16 operation hours is estimated to be about 1000g in Mk-IIA and 500-600g in Mk-IIGB. This is in good agreement with the amount eroded from the first wall derived from spectroscopic data [315, 316]. The carbon deposition rates are similar for both divertor configurations with consequently similar fuel retention by co-deposition; however, the co-deposition occurs preferentially on different locations, namely the louver area (Mk-IIA) and surfaces in the private flux region excluding the dome (Mk-IIGB). For beryllium in JET, similar analysis indicates good agreement of total erosion and total deposition [316]. Tungsten migration from main chamber walls to divertor was investigated in ASDEX Upgrade. A 10% fraction of the eroded tungsten reaches the divertor target area [282]. The tungsten is mainly eroded during limiter configuration start-up and ramp-down discharge phases. DIVIMP modelling showed that most of the eroded tungsten is expected to be re-deposited at the inner main chamber wall [291].

ELMs could influence material migration in burning plasma experiments. Presently, erosion/deposition and material flow measurements are difficult to resolve on an ELM time scale. Some ELM phenomena have been observed including:

- Increased energy/particle fluxes causing increased transient erosion of the divertor target and main chamber plasma facing components. The migration of the eroded material has yet to be quantified; however large ELMs on JET enhanced material deposition to areas not in direct plasma contact [317].
- Deuteron (and possibly impurity) flows are modified by ELMs. Expulsion of impurities from the confined plasma into the SOL occurs at ELMs [318]. Also, flow changes occur such as flow reversal near the divertor entrance following ELMs [319].

4.2.4.4. Extrapolation of present results to ITER and open issues.

There are several steps to impurity behaviour - erosion, migration and deposition. At each step, attempts have been made to characterize current experience and use that information to predict ITER operation. Modelling efforts estimated divertor strike point net C erosion rates which vary with values of 6.4 nm/s [272], 10 nm/s [320], 20 nm/s net erosion [273], 30 nm/s [321] and 100 nm/s [311]. Clearly, additional experiments aimed at testing the codes and the base assumptions that are incorporated into them are needed. The effects of the level of detachment and mixed materials must also be addressed.

The prediction of main chamber surface erosion is based on charge exchange induced sputtering. The major uncertainties arise from the contribution of ion bombardment due to localized or turbulent processes (e.g. ELMs or blobs). Corresponding measured erosion rates significantly exceed the rates due to impact of charge exchange atoms.

In the area of transport (material migration), key issues are the modelling of flows, ion temperature gradient forces and electric fields. Progress has been made in characterizing SOL flows. However the magnitude and poloidal variation is not understood, so that projection to ITER is difficult.

The situation is similar with respect to deposition. While a number of C PFC divertor tokamaks observe inner divertor deposition, the detailed pattern in the inner divertor has not been simulated. Recent efforts using ^{13}C tracer studies, analysis of un-wetted surfaces (e.g. tile sides) and comparison to deposition of metallic impurities are aimed at providing the needed benchmarking for models.

In summary, extensive experimental and modelling efforts have improved our knowledge of material migration processes. However, the predictions for ITER erosion, optimal material selection, material migration, and resultant tritium retention are still uncertain. The development of new experimental measurements (e.g. ^{13}C and metallic tracers) and progress in modelling (e.g. flows) in both existing experiments and the ITER non-nuclear phase are needed.

4.2.5. Divertor and main chamber materials.

4.2.5.1. Expected requirements of materials.

Plasma-facing component (PFC) materials used for design of next-step DT burning plasma devices must meet several demands including resistance to damage by large steady-state heat loads, resilience to transient heating and MHD events, sufficient component lifetime against erosion by the plasma, and minimization of tritium retention in the vessel. The demands on PFC materials in ITER will go far beyond those of existing machines because of simultaneous large increases in several parameters: power density, plasma stored energy, tritium throughput, and plasma duration. As a result of these strenuous demands, issues arising from plasma-materials interactions (PMI) can limit the viability of the PFC components and, therefore, the operational availability of future devices, as indicated from experience in present experiments reviewed in [274]. On the other hand, significant progress has been made in producing actively cooled C or W clad high heat-flux components, which reliably withstand thousands of thermal cycles up to levels of 20 MW·m^{-2}, as required in ITER [322].

Recent research has identified two critical issues with respect to the behaviour of PFC materials in fusion devices: 1) tritium retention rates in plasma-deposited films and 2)

lifetime/viability issues for materials undergoing ablation or melting from transient heating events like ELMs and disruptions. Present knowledge favours metal PFC materials on the former issue and carbon-based PFC materials on the latter, although significant uncertainties remain in the extrapolation from present to next step-devices. As a result, the basis for the choice of the original PFC material distribution in ITER remains unchanged. Furthermore, recent research has demonstrated the existence of long-range transport of materials in tokamak devices (see Sect. 4.2.4), which causes the formation of mixed material layers (Be, C and W in the case of ITER) adding further uncertainties to the extrapolability of present results to next step devices, which will have different PFC material composition (see Sec. 4.2.5.6).

Given the uncertainties in our knowledge of plasma-wall interactions for next-step-relevant conditions (in particular of the interactions between the plasma and the main wall), it cannot be ruled out that the replacement of major plasma facing components and testing of different combinations of plasma facing materials will be necessary over the lifetime of a device like ITER. This is foreseen in the ITER design both for the divertor target and the main chamber PFCs. The ITER divertor targets are designed to be replaced by remote handling as part of the routine maintenance of the device (remote handling shutdown for the replacement of all divertor cassettes of ~ 3-6 months duration). On the other hand, the blanket modules, on which the main chamber PFCs are mounted, are designed to be replaced by remote handling in small numbers and only occasionally, following the initial requirements of the ITER design [323, 324]. While not presently a reference scenario, the entire first wall replacement is, in principle, possible. However, its cost, practical implementation and schedule require further assessment [325].

4.2.5.2. Issues related to use of carbon containing materials.

4.2.5.2.1. Operational experiences with carbon based devices.
Graphite is the most commonly used PFC material in present devices because of its good compatibility with a wide variety of plasma operations. The present experience with carbon allows for an optimistic extrapolation of its compatibility with thermonuclear plasmas in ITER : a) because of the good thermo-mechanical properties of CFC (Carbon Fibre Composites) and the lack of melting under transient power fluxes, the compatibility of these materials with high power flux plasmas its optimal, b) despite its relatively large sputtering yield, high density plasmas in ITER-like regimes can be obtained in present experiments with a relatively low core contamination ($Z_{eff} = 1.5 - 2.0$) [326], and c) due to its low Z, the core radiative losses associated with C in high temperature plasmas are low, while the divertor radiative losses by C, which are necessary to maintain semi-detached operation in ITER, can

decrease the divertor power flux by more than a factor of ~ 2 compared to fully attached conditions [327, 160].

The most serious issues with carbon PFCs are lifetime restrictions on net erosion areas due to the large erosion yield of carbon, the associated build-up of carbon deposits and the subsequent tritium retention in these layers [274, 160], which is the main mechanism of long-term hydrogenic isotope retention in carbon clad fusion devices. A tokamak demonstration of a regime that maximises the radiation losses at the divertor, while maintaining tritium retention at very low levels, as required in ITER, remains to be carried out. A target value for the effective (i.e., after T-removal techniques are applied) T retention for routine ITER operation is ~ 0.1 % of the injected T. The required amount of T in ITER is estimated at ~ 50 g/discharge for the Q_{DT} = 10 reference scenario [328]. This is equivalent to a retention of ~ 0.05 g per discharge, which would allow ~ 7000 full performance discharges to be carried out before a T-removal shutdown is required.

4.2.5.2.2. Erosion behaviour of carbon based wall materials.

While the mechanisms of physical sputtering are well understood, the chemical erosion of carbon, i.e. the release of volatile hydrocarbon molecules and radicals (e.g. CH_3, CH_4, C_2H_4, etc.) caused by ionic and atomic hydrogen fluxes, continues to be an active area of research. Chemical erosion yields depend on a wide variety of conditions: target temperature (T_{surf}), incident particle energy, flux density Γ_i, plasma impurities; as well as on the surface conditions and exposure history of the carbon material [274].

Chemical erosion yield is measured on carbon-clad devices using visible spectroscopy of highly dissociated hydrocarbon molecules (CH, C_2) interpreted through adequate modelling of the molecular processes [329]. The yields measured for attached (ionising) divertor plasmas span a range from 0.4 - 10% corresponding to a large range of experimental conditions with T_{surf} = 350-600 K, plasma fluxes of Γ_i = 0.1-1.0 10^{23} $m^{-2}s^{-1}$ and, possibly, the enhanced erosion of co-deposited films under high power loads [330, 331, 81, 332]. DIII-D reports a total suppression of hydrocarbon emission in detached plasmas (T_e < 2 eV), despite the modelled high photon efficiencies for CH in these conditions, which suggests a highly suppressed chemical erosion yield < 0.01% [81]. The very large scatter in experimental measurements indicates that all plasma/surface parameters (such as ion impact energy, flux, surface temperature) play a major role in determining the magnitude of chemical erosion. The unprecedented high ion and power flux densities near the ITER divertor strike-points, therefore, make the prediction of chemical erosion very complex.

A database of chemical erosion yield obtained in different tokamaks, linear plasma devices and beam experiments has been recently compiled and used to normalise the yield data with respect to ion energy, target temperature and ion flux. The database suggests a weak dependence of the erosion yield on ion impact energy between 10 and 200 eV and a clear

tendency for the yield to decrease with increasing flux density [276], implying a ~ 2.5-fold reduction in yield for the ITER strike-point conditions compared to previous assumptions ~ 1 %). Figure 4.2.5-1 illustrates the implications that such a yield reduction (taking into account realistic surface temperature, impact energy and flux dependences) has on the calculated gross erosion of the ITER divertor target [333] compared to previous estimates with a ~ 1% fixed chemical erosion yield [334]. The reduction of the chemical gross erosion yield results in similar improvements in target lifetime and expected tritium retention. This figure illustrates the complex coupling of target erosion and power load and associated tritium retention which makes predictions to ITER uncertain :

a) The carbon chemical erosion yield depends strongly on the target temperature, which is determined by the incident plasma power flux.

b) The power flux at the divertor is determined by the radiative losses and the degree of detachment, which is strongly influenced by the release of carbon into the divertor by chemical erosion.

On the other hand, changes of the plasma conditions at the divertor from quiescent to transient phases of the discharge (ELMs, disruptions) will most likely contribute more to carbon erosion than the uncertainties in the chemical erosion yield described above.

4.2.5.2.3. Brittle destruction.

New results have been obtained on the erosion of isotropic graphite and carbon fibre composites by explosive emission of small particulates occurring under rapid (~ms) heat loads, so-called brittle destruction [335], which leads to enhanced erosion and surface non-uniformities for carbon materials. This erosion mechanism has been observed to set in for graphite above an energy density threshold > 100 MJ m^{-2} $s^{-1/2}$ (which is more than twice larger than the carbon sublimation limit) and at somewhat lower values for CFC. CFC erosion associated with local overheating and matrix-fibre detachment has been identified in experiments in electron beams/plasma guns and modelling [336]. Therefore, while carbon is chosen for its robustness to transient heating events like ELMs and disruption in ITER, this resilience is limited, and energy densities from transient events in ITER must be kept below the sublimation and brittle destruction thresholds for carbon in order to prevent a severe limitation of the ITER divertor target lifetime even for CFCs.

4.2.5.2.4. Location and properties of carbon film deposits.

Recent experiments show that nearly all of the carbon films formed by chemical erosion are deposited in the line of sight of high sticking probability C_xH_y fragments [307]. In general, a strong temperature dependence of the deposition is observed, which is due to the strong temperature dependence of the re-erosion of deposited layers by atomic hydrogen, as demonstrated in laboratory experiments [337]. This has important implications for the

recovery of the tritium retained on deposited hydrocarbon films. The access to these films is generally easier if they are deposited in surfaces close to the region of interaction between the plasma and the material (where the material is subject to both hydrogen atomic fluxes and power fluxes and is, therefore, at high temperatures) than if they are deposited in remote and/on shadowed areas such as tile gaps (see Sect. 4.2.6 for more details). The amount of hydrocarbons deposited in very remote areas, such as divertor pump ducts is very small (typically less than 1% of carbon films) [338, 339, 340, 81] while the amount of hydrocarbons that can deposit in shadowed areas close to the divertor can be very large [296].

The structure and hydrogenic content of carbon deposits is highly dependent on its location. Deposits on plasma-receiving surfaces are hard and brittle, while deposits elsewhere are softer and exhibit columnar structures [341]. Various deuterium fractions in the carbon deposits can be found. Usually, areas that are subject to large temperature excursions during operation show very low hydrogen concentrations (10^{-3} to 10^{-2}) [320, 342, 340] consistent with hydrogen desorption during these high temperature transients. On the contrary, shadowed areas of plasma facing components, such as those in TFTR [343] and JET [344], can lead to the deposition of hydrocarbons with a large hydrogen content (much larger than 10^{-1}). The contribution of the hydrocarbon deposition in tile gaps to the observed total fuel retention remains an active field of research of critical importance for the design of the ITER divertor target.

4.2.5.3. Beryllium.

Beryllium (Be) has two major advantages for its use as main wall plasma facing material (in areas of low power flux) in fusion devices : a) it is a low Z material and, as its sputtering yield is not higher than that of carbon at low plasma temperatures [345], it leads to low radiative losses from the core plasma, and b) it provides gettering for the residual oxygen from the base vacuum. Both these advantages have been demonstrated at JET in which both Be evaporation [346] and solid Be plasma facing components [347] have been used.

The plasma interaction behaviour of beryllium is affected by the presence of oxygen and other impurities. Oxygen forms a BeO_2 layer on PFCs that reduces the physical sputtering yield with respect to the pure material. On the other hand, the presence of oxygen in Be increases the retention of hydrogen, which for the pure material is very small [348] to similar levels of hydrocarbon deposits (H/Be $\sim$ 0.3) [349, 350]. However, new results from experiments in PISCES-B have produced oxygen-containing Be deposits (O/Be $\sim$ 0.03-0.3) with low hydrogen retention (H/Be $\sim$ 0.01-0.03) for surface temperatures of 400-600 K [351], indicating that besides oxygen other impurities may be responsible for the large hydrogen levels observed in some oxidised Be samples. Besides this, the temperature for the release of hydrogen from deposited Be layers is considerably lower than from carbon layers. On the basis of these results, retention of hydrogenic fuel in Be is expected to be very small when

compared to carbon, although a complete assessment including the effects on temperature excursions of the PFCs and their influence of oxygen diffusion and H trapping remains to be done. Furthermore, a mechanism which enhances the erosion of Be (and all metals) at high temperatures has been identified [352, 353]. This mechanism is similar to the radiation-enhanced sublimation of carbon and leads to erosion rates which are one order of magnitude larger than physical sputtering ($E_{ion} \sim 50$ eV) for $T_{surf} \sim 1200$ K. This enhancement would be particularly important if significant energy fluxes reach the ITER first wall during transients such as ELMs and make the prediction of the erosion of the ITER main wall very uncertain for such conditions.

The major issue concerning the use of Be as plasma facing material in next step devices, such as ITER, is related to its relatively low melting temperature (1550 K). Deposition of plasma energy during transients such as ELMs, VDEs and disruptions can bring the Be temperature to the melting value and, thus, cause extended melting of PFCs. Furthermore, techniques that mitigate the effect of such events, such as massive impurity puffing to mitigate the thermal quench energy flux during disruptions [354], cause radiative fluxes leading to a deposition of energy of ~ 0.5MJ/m^2 in timescales shorter than 1 ms, causing significant melting of the Be PFCs (20-50 μm). The dynamics and loss of the layers of molten Be during transients, which are subject to forces associated with plasma impact, Lorentz forces, etc., remain to be studied in detail. The experience with Be in JET was recently reviewed [355] with emphasis on the behaviour and influence on the plasma of Be melting and molten Be-PFCs. In JET, a single large ELM depositing ~1 MJ in less than 1ms [356], led to substantial melting of the Be JET divertor target and terminated the high performance ELM-free phase of the discharge. However, the effects of Be melting on subsequent plasma operations were not catastrophic, due to the plasma's high tolerance to the low-Z Be. Therefore, the precise implications of significant Be first-wall melting on the lifetime of the wall in ITER, and on the performance of a burning plasma experiment like ITER, are still not clear and require further study.

4.2.5.4. High-Z Materials.

For general issues on the use of high-Z plasma facing components in present fusion devices and on the development of these materials for fusion applications, the reader is referred to recent reviews on these topics [357, 358].

4.2.5.4.1. Behaviour of high-Z plasma-facing components in tokamak experiments.

The major focus of research on high-Z materials in fusion devices has been the achievement of low core plasma contamination, due to the low "fatal" core concentrations (for ignition 10^{-3} to 10^{-4} for Mo and W respectively) in burning plasma experiments. The core concentration of high-Z impurities is controlled by both the impurity physical sputtering

source at PFCs (see Sect. 4.2.5.4.2) and impurity transport. High Z materials have been used for the majority of PFCs in several large fusion experiments : FTU with molybdenum toroidal limiters [359], Alcator C-Mod with a molybdenum first wall and divertor [360], TEXTOR with high-Z components as limiters [361], and ASDEX-Upgrade both at the divertor [362] and main chamber [363]. Recent experimental results from these devices show that acceptable core impurity fractions can be obtained by adequate plasma operation: high plasma density, central heating and magnetic divertor geometry all help to control the overall core impurity levels and central impurity peaking in high performance plasmas. These results have increased the confidence for the further possible use of high-Z PFCs in future burning plasma experiments and fusion reactors.

In general, high Z core concentrations decrease with increasing density [364, 365, 361], as expected from the reduction of physical sputtering with edge temperature, and are lower (by factors of 2.5 to 10) in divertor than in limiter geometries [290, 364]. Experience in ASDEX-Upgrade has shown that it is possible to operate the device in a large range of conditions while maintaining the core W concentration in a range of 10^{-6} to $3 \ 10^{-5}$ both with W as divertor and main chamber material [363]. On the other hand Alcator C-Mod, with complete molybdenum PFCs, finds that the molybdenum concentrations can reach values as high as 10^{-3} in some operating conditions [364]. The different observations in ASDEX Upgrade and Alcator C-mod may be attributable to differences in high-Z first-wall coverage between the two devices.

Impurity transport, rather than the source, can play a dominant role in determining high-Z core concentrations, in agreement with expectations from neo-classical transport theory (for example see [366]). Large high Z impurity accumulation is observed in conditions that are favourable for this from neoclassical transport expectations, as seen in TEXTOR [367] and FTU [368]. Central high-Z accumulation leads to strong central radiation, hollow temperature profiles and can, eventually, lead to the termination of the discharge. Studies in ASDEX Upgrade have shown that the central W concentration is dominated by impurity transport in the bulk plasma with the lowest W concentrations being found for discharges at high density with flat density profiles and high levels of additional heating [152]. Discharges with peaked density profiles showed, on the contrary, increased core W concentrations and even accumulation [152]. This problem is exacerbated for discharges with reduced core transport, such as with ITBs [369].

Because the concentration of high Z impurities is dominated by transport, it is possible to affect the core levels of impurities by applying central heating through the coupling of energy and particle transport in many tokamak regimes. This technique has been demonstrated in TEXTOR [370], Alcator C-Mod for discharges with ITBs [151] and studied in detail in ASDEX Upgrade with ICRH and ECRH [371]. The reduction of the central concentration of W can be explained by the changes caused by the central heating in the

plasma particle transport [371, 372]. On the basis of these physics arguments, present modelling [373] suggests that no W accumulation is expected in the ITER reference $Q_{DT} = 10$ scenario. For regimes with internal transport barriers, no detailed modelling has been carried out for ITER conditions but it is expected that the accumulation of W in the core of these plasmas would lead to more serious problems [369].

The operating conditions of the device can affect the core impurity content. For ASDEX Upgrade, which is gradually switching to W walls, the clearest influence of W is seen for discharges with low levels of input power, in which long ELM-free periods can lead to increased core radiation decreasing further the ELM frequency [363]. This negative feedback loop can be easily broken either by increasing the level of additional heating, which increases the ELM frequency, or by triggering ELMs with pellets [363]. In Alcator C-Mod the molybdenum level is most clearly linked to the confinement mode (ELM-free operation leads to much higher Mo concentrations that EDA mode [364]) and the quality of the boronised layer. As the boronisation layer wears off through operation, the Mo levels increase [290].

Even with significant surface area coverage by high-Z materials, plasmas in present devices are often dominated by the more easily eroded low-Z impurities. These are either introduced through conditioning techniques or originated from other low-Z PFCs in the device. For instance, light intrinsic impurities in ASDEX Upgrade have not changed significantly despite the exchange of 40% of the plasma facing components from graphite to tungsten [363]. The experimental observations show that this is associated with a highly dynamic equilibrium of erosion and deposition on the W PFCs of carbon originating from other components [285]. Similarly, the level of Mo in the core was shown to be dependent on how recently the surfaces were boronised [290]. Such results indicate the inherent difficulties in interpretation of experiments with a significant amount of mixed materials, and their extrapolation to devices like ITER (see Section 4.2.5.6).

Significant melting of high-Z PFCs under transient loads such as ELMs and disruptions is a major concern for their use in next step devices like ITER, but it is not expected in present tokamaks due to the lower energy densities that can be achieved. Most of the melting of high-Z PFCs observed in present devices is due to : poor thermal contact between high-Z coatings and the substrate, tile misalignments, and/or runaway electrons [374]. Energy densities during ITER transients may cause significant melting of the high Z PFCs [166, 375]. The dynamics of the molten layer and the effect of repetitive melting under ELMs and disruptions both on the lifetime of the PFCs and on ITER plasma operation remain open and they are, presently, an active field of research [161].

4.2.5.4.2. Erosion of high-Z materials in a tokamak environment.

Due to the large sputtering thresholds (~ 209 eV for D on W), the erosion of W PFCs by a low temperature hydrogenic plasma (T_e < 20 eV) during quiescent phases of the

discharges, particularly for a detached divertor plasma, will be negligible. No substantial chemical erosion by volatile W-oxides has been measured either, in line with recent molecular dynamics calculations where chemical erosion of W by O was found to be negligible in the relevant parameter range [376].

The major source of sputtering of high Z materials are impurity ions in the background plasma. These may be intrinsic or seeded, in order to provide radiative cooling of the divertor plasma, and lead to an "effective sputtering yield" of W under D-plasma impact ($Y_{eff}^W = \Gamma_W/\Gamma_D$), which is much larger than that due to the impact of the D ionic flow. Impurities with higher charge states gain additional energy through the sheath potential at targets and dominate the effective physical sputtering yield of high Z materials. Modelling of Alcator C-Mod shows that the measured Mo influx can only be reproduced if the sputtering by ~ 2% B^{3+} (from boronisation) and Mo self-sputtering are taken into account [377], while in RF heated discharges localised Mo sputtering near RF antennae was linked to high ion impact energies due to sheath rectification [290]. In ASDEX Upgrade (see Fig. 4.2.5-2), divertor W release is dominated by low-Z impurity impact and erosion results could be modelled taking into account sputtering and deposition from 1% carbon impurities [304]. The higher effective W yields in TEXTOR (Fig. 4.2.5-2) at similar plasma temperatures are attributed to larger fractions of C and O impurity fluxes in these plasmas (factors of 2-5) [357] and to higher W self-sputtering due to higher W concentration in TEXTOR. ASDEX Upgrade has shown that the measured inner limiter W erosion exceeds the expected values from erosion by charge-exchange (CX) particles [378] by at least an order of magnitude. This is mostly attributed to direct plasma contact during plasma ramp-up and ramp-down, with an inner-wall limited phase [379], but continuous erosion during the divertor phase due to impurity ion sputtering contributes significantly as well and, therefore, should be taken into account when estimating the erosion of the ITER main chamber.

Net erosion of high-Z materials is reduced by prompt re-deposition, which is strong due to their large mass and short ionisation mean free path into the plasma [279]. In Alcator C-Mod, the Mo outer strike point region net erosion is only ~ 0.1nm/s [278], which is a factor of 10-100 lower than in the C-clad DIII-D divertor [294].

A major uncertainty in the erosion of high Z material in next step devices is their behaviour under transient loads such as ELMs and disruptions, which can cause the high Z material to melt [166, 375]. Significant displacement of this molten layer and its splashing could cause losses of several μm of material per event, which is much larger than the erosion during quiescent phases of the discharge, and can lead to further roughening of the surface, causing the PFCs to be more prone to further melting by the power fluxes during the steady-state phases of the discharge. The detailed processes that are involved in these phenomena are complex, but initial results in laboratory experiments have demonstrated that the detailed PFC design can have a deep influence over the melt layer dynamics and prevent its loss under

ELM-like loads [161]. Nevertheless, due to the potential implications for ITER, the control of ELM and disruption energy fluxes remains a high priority research issue for the use of metal PFCs in ITER.

4.2.5.4.3. Hydrogen retention and blister/bubble-formation in tungsten.

In general, the retention of hydrogen in W is very small [380], although the measured values of the retention depend considerably on material grade, fabrication process, temperature of the W and the presence of carbon and oxygen [381]. In TEXTOR, pure W surfaces had D inventories $< 10^{19}$D m^{-2}, whereas co-deposited layers of B and C on tungsten revealed D-contents higher by more than two orders of magnitude [382]. These results indicate that the use of mixed materials as PFCs in ITER adds significant complexity to understanding tritium retention with high-Z materials, since deposit layers are typically dominated by the low-Z plasma constituent impurities (see Sect. 4.2.5.6).

The formation of gaseous blisters/bubbles in high-Z materials has been studied because of its potential to: a) increase the amount of T-retention by high-Z materials and b) to cause surface damage and enhanced erosion of these materials. Hydrogen blisters/bubbles are formed in W during large fluence irradiation experiments [383]. This can be effectively suppressed either by adequate surface treatment of the plasma facing materials [384, 385] or by adequate fabrication of the materials themselves [386]. Helium bubbles and holes can also be formed in W under high fluence He plasma irradiation, even at relatively high surface temperature [387], which could be a critical issue for the erosion of W. Both processes can, in principle, increase the hydrogen retention in W and may give rise to an initial surface damage (micro cracks), which may then be enhanced by overheating under plasma exposure. Despite the possible enhancement with respect to its base-level retention, T retention in W is expected to be very low in ITER, in comparison with that associated with the use of a carbon-based material, because of the intrinsic low T retention of W (even with blisters/bubbles).

Although the detailed conditions and mechanisms that lead to bubble formation in laboratory experiments have been studied in detail, no bubble formation, neither from hydrogen nor from helium bombardment, has ever been observed in present tokamaks. This is probably associated with the small integrated fluences on W PFCs that can be achieved in present experiments compared to ITER and, possibly, the low He concentrations in these plasmas. Direct extrapolation of the results obtained in present tokamak experiments, indicates that bubble/blister formation in the ITER W PFCs may not be a dominant process for ITER conditions. However, due to the uncertainties with respect to fluences and He concentrations described above, a final quantitative assessment of these effects for ITER requires further experimental studies in present tokamaks and laboratory experiments for the various W grades foreseen for ITER PFCs.

4.2.5.5. Wall conditioning and particle control.

In next-step superconducting devices like ITER, the tasks of wall conditioning are : (i) commissioning before operation after major openings, (ii) limiting release of hydrogen and non-hydrogenic gas impurities during plasma operation and (iii) the limitation of the tritium inventory in the plasma facing components. The first task is done with no magnetic field, and most of the techniques used in present day tokamaks can be used (see [18]). The last two must be done primarily with the toroidal field coils energised, which rules out many of the standard conditioning techniques used in today's experiments. In this section we concentrate on the advances in the last few years on conditioning techniques for task (ii), while tritium removal techniques are discussed in Sect. 4.2.6.

4.2.5.5.1. Conditioning with permanent magnetic field.

In the presence of a permanent magnetic field, RF assisted discharge cleaning is the most suitable technique available, and experiments have been reported from different tokamaks, using ECR-DC (Electron Cyclotron Resonance-DC) [388, 389] or ICR-DC (Ion Cyclotron Resonance-DC) [390, 391, 392] and from the stellarator W7-AS (ICR-DC [393]). These techniques have recently been reviewed in [394], where the reader is referred to for more detailed information. Two critical parameters need to be adjusted for the optimisation of the conditioning : a) the homogeneity of the discharge as achieved in HT-7 [392] and b) for ICR-DC, optimising the wave heating so that energetic particle bombardment of the first wall occurs, while still achieving a low density, low temperature plasma to avoid re-ionization and re-deposition of wall-desorbed neutrals before they are exhausted by the pumping system. Typical values are 10^{16} m^{-3} < n_e < 10^{17} m^{-3} and 8 < T_e < 40 eV, but with ion energies of the order of a few keV, allowing isotope exchange up to several 100 nm's in carbon [390, 392]. The required RF power varies between ten and hundreds of kW [390, 391, 392] in present size devices. The usual sequence consists of first using D$_2$ as the working gas for wall cleaning and isotope exchange, and then He for deuterium removal [390, 392]. The overall efficiency of RF-DC is shown to be comparable to that of GDC (Glow Discharge Cleaning) in the stellarator W7-AS [393].

Very recently, in HT-7 a carbon removal and surface conditioning campaign was run using He/O-ICRH discharges, varying the oxygen partial pressure and the ICRH power at continuous toroidal field. Carbon removal rates were determined by residual mass analysis of the exhaust gas and impressive cleaning rates could be extrapolated to ITER [395].

4.2.5.6. Implications on the use of multiple PFC materials.

The present design for ITER foresees the use of three plasma-facing materials: Be for the first wall (700 m^2), W for the divertor and baffle region (100 m^2) and CFC for the divertor strike point tiles (50 m^2). The choice of the different materials is motivated by the

optimisation of plasma-wall interaction processes for the pure materials. Cross contamination of the material surfaces will be unavoidable. Therefore, the plasma-wall processes have to be evaluated for the case of mixed materials. There is no fusion device to date using the same material mixture as foreseen for ITER. Limited experience exists for the simultaneous use of different materials, e.g., JET for C and Be and ASDEX Upgrade for C and W. Laboratory studies can cover all three possible combinations, in principle. However, the number of parameters which control the interaction among the materials and of those with the plasma is extremely large and, therefore, our level of knowledge in this field and our predictions of the dominant phenomenology in next step devices are very primitive at this stage.

4.2.5.6.1. Formation of mixed materials.

The carbon-metal interactions are governed both by carbide formation reactions, carbon diffusion into the bulk metal and by the bond type of the formed carbide. Transition metals (e.g. W, Ti, Ta, Fe, Ni) form metallic carbides, where the formation of carbides occurs above a material-specific threshold temperature and is followed by strong carbon diffusion into the metal bulk at elevated temperatures. In contrast to these metallic carbides, ionic or covalent carbides (e.g. Be_2C, SiC) lack the diffusive carbon loss process. After a temperature threshold, carbide formation proceeds until the available carbon amount has reacted and the stoichiometric carbide is formed [396]. Ternary systems (i.e. with three material species) pose additional difficulties, especially if oxygen is one component. Due to the formation of volatile species, predictions of the ternary system behaviour, e.g. with increasing temperatures, are difficult. For example, in the ternary system W-C-O, the erosion of carbon films at elevated temperatures even depends on the type of oxide [397].

Beryllium and tungsten form several alloys, with some alloys exhibiting enriched Be concentrations (e.g. $Be_{12}W$) and melting temperature similar to Be [398], as reported recently from experiments in PISCES-B [399, 400]. However, these Be-rich phases were not observed when evaporating Be onto W surfaces and investigating the inter-metallic phases using X-ray photoelectron spectroscopy. Upon heating, a < 2nm interfacial layer reacted to Be_2W while for thicker deposits the remaining Be layer evaporated [401].

It is unclear whether the conditions expected in ITER will lead to the formation of such alloys between the Be eroded at the wall that deposits on the divertor and the W divertor PFCs, leading to the W PFCs to lose some of their structural and thermomechanical properties. The formation of such alloys would be more probable for the case of a full W target rather than if W PFCs are limited to the baffle and dome region, as in the reference ITER start-up PFC material distribution, in which the surface temperatures are lower. The formation of Be/W alloys thus remains a concern for ITER and is presently under investigation.

4.2.5.6.2. Effects of material mixing on erosion.

The simultaneous impact of plasma ions with impurity ions eroded from other plasma facing materials can lead to both enhanced and reduced erosion. As an example, the erosion of W by C/D impact was investigated [402]. The erosion of W in areas of low plasma temperatures is only possible by sputtering due to impurity ions. The sputtering threshold for D/T ions is of the order of 200 eV, while it is reduced for typical impurity ions to less than 30 eV (see Sec. 4.2.5.4.2.) [403]. Therefore, the erosion will depend strongly on the concentration of impurity ions in the incident plasma. For low impurity concentration, where the incident flux of deuterium keeps the W surface clean, the erosion rate of W is proportional to the concentration of carbon ions. For high carbon concentrations the implanted carbon atoms are not completely removed and a protective layer will form, which suppresses W erosion. The maximum effective erosion yield will be obtained for the C/W system at a carbon concentration in the plasma of about 4% (see Fig 4.2.5-3. [402]), which is a typical concentration of carbon in tokamaks with carbon PFC's. At elevated temperatures, enhanced erosion processes and bulk diffusion may alter the detailed balance of erosion/deposition [404] leading to higher erosion yields.

Carbon chemical erosion can be drastically reduced by impurities on the surface [405] and in the bulk [406]. Surface impurities, such as incident Be ions on the ITER C target can reduce the chemical erosion of carbon by coverage effects [405, 407]. Bulk impurities added on atomic scale, such as Ti, W or V at concentrations of less than 10 at%, decrease the activation energy for hydrogen recombinative release thus reducing chemical erosion at elevated temperatures [408].

In general, the introduction of mixed materials in fusion devices complicates enormously the erosion/deposition calculations, and the implications for the calculated erosion rates in devices like ITER are just beginning to be addressed.

4.2.5.6.3. Effects on H isotope retention.

The hydrogen retention in plasma facing materials and in redeposited layers is very sensitive to surface and bulk contamination of the material. Surface oxide or carbide layers at the surface may act as diffusion barriers and strongly influence the recombination necessary for molecular release of hydrogen. Since the number of parameters is large (multi-material mixing, material structure, temperature, ion energy) no general statements can be made. Both large increases and reductions of retention are observed compared to pure materials and reliable estimates of the situation in next step devices do not exist. Therefore, several examples of experimental results that may be relevant for ITER are summarised here. Superficial oxide or C layers are seen to lead to the increase of hydrogen retention in W [381]. On the other hand, in W samples pre-bombarded with C-ions, a transition from retention similar to pure C, to WC and pure W was observed [409]. Similarly, fully oxidized Be retains

D at similar concentrations as carbon [350, 349], with desorption starting at 600 K, while in clean Be the retention is strongly reduced [348] and the release temperatures are around 400 K. As described in Sect 4.2.5.3, recent data from PISCES-B indicates that the Be/D deposition rate and the presence of other impurities may be additional controlling parameters to the D retention in Be with impurities. A C-Be mixed-material layer was formed containing at least an order of magnitude more deuterium at room temperature than pure Be [399], but this additional amount of D decreased and vanished at 500°C.

From the examples above, it is clear that the formation of mixed materials have significant effects on the retention of hydrogenic isotopes either increasing or decreasing it with respect to the pure materials. Determining which will be the dominant phenomena in ITER is still far beyond the present understanding of the processes involved and, because of its importance for ITER operation, it remains an active field of research.

4.2.5.6.4. Effects on tritium removal techniques (oxidation or heating).

Doped graphites and carbon layers show in many cases drastically reduced chemical erosion properties, either due to their influence on the hydrogen recombinative release or due to enrichment of the impurity level at the surface, leading to protective surface layers. This can affect not only its erosion behaviour and its hydrogen retention but also the effectiveness of techniques which can be applied successfully to remove tritium from pure materials. One technique for tritium removal relies on the chemical erosion of carbon deposits due to oxidation [410]. Similar to hydrogen, the chemical reactivity with oxygen can be reduced by the presence of impurities in C, which makes the removal more difficult. For layers containing B due to boronisation of the vessel walls in tokamaks, after an initial fast oxidative removal of D and C, much lower removal rate levels were reached, the D being locked up by a stable boron layer in the material [411].

Although little is known of the effect of mixed materials on tritium removal techniques, it is clear that the presence of mixed materials can complicate considerably the practical application of these techniques. It is, therefore, necessary to proceed to a thorough investigation of tritium removal techniques for the material mixes expected to be formed in ITER so that a reliable estimate of the viability of such techniques can be obtained.
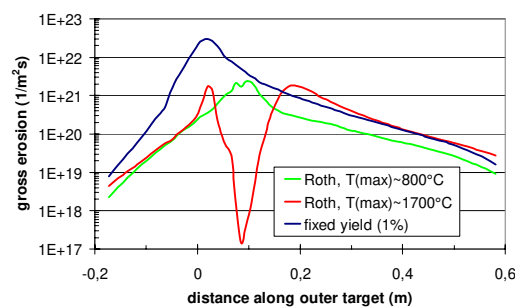

Figure 4.2.5-1. Calculated chemical gross erosion of the outer ITER divertor target assuming a fixed erosion yield of 1% [334] or the full erosion dependence on energy, surface

temperature and particle flux [276]. Calculations are done for a high and a low surface temperature case [412], (after [333]).
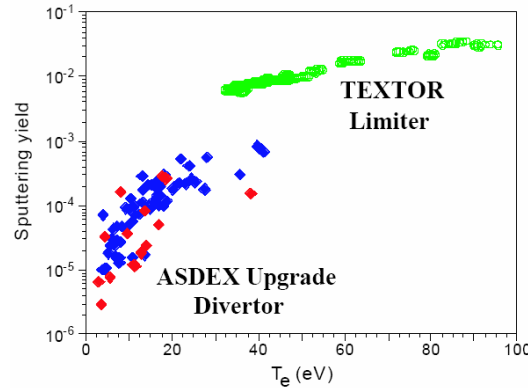

Figure 4.2.5-2. Effective W erosion yield as a function of the local plasma temperature at TEXTOR test limiters and the ASDEX Upgrade outer divertor target (after [357]).
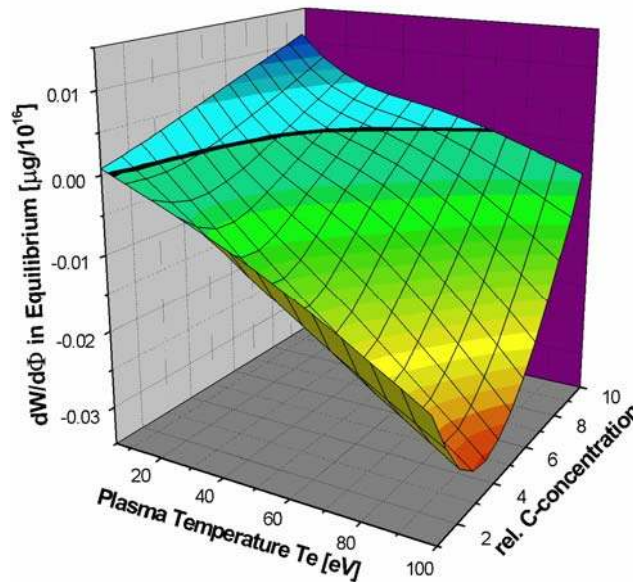

Figure 4.2.5-3. Dependence of tungsten (W) erosion on plasma electron temperature and on the carbon concentration (%) in the incident D plasma [402]. Negative values of dW/dΦ denote net W erosion.

4.2.6. Tritium retention.
4.2.6.1. Introduction.

ITER will routinely use large amounts of tritium as fuel (e.g., 100 times more in ITER than in present T-experiments), and control of the tritium inventory will be a key operational issue in any next-step experimental burning plasma facility both for environmental and safety reasons. The working guideline for the maximum in-vessel inventory of tritium that can be mobilised in the ITER vacuum vessel is presently ~ 350 g. The assumption made for safety analysis is ~ 1 kg of tritium mobilisable in the vacuum vessel [134]. Independent of safety

considerations, tritium is limited in supply and, for this reason alone, as much as possible needs to be recovered and re-used during the operation of any next step device.

The recycling of hydrogenic fuel and its retention in plasma facing-materials considered for next step devices has been a traditional research topic in all fusion devices but the research in this field has become particularly active after the use of considerable amounts of tritium and its incomplete recovery in the full D-T campaigns in TFTR [413, 414] and JET [415, 416]. A more detailed description of these observations, the mechanisms of T retention and the techniques used to remove fuel from PFCs in fusion devices can be found in [274, 380, 417, 418]. Table 4.2.6-1 provides some key quantities related to tritium balance in experiments carried out in existing tokamaks and ITER [415, 419, 420, 18].

Parameter	TFTR T-experiment	JET T-experiment	ITER projections & requirements
Tritium in-vessel inventory limit	2 g	20 g site inventory	350 g (guideline value) 1000 g (assumption for safety evaluation)
T-introduced in the torus	5.2 g	35 g	50 g/pulse (400 s)
Discharge number and duration before inventory limit first approached.	708 pulses $\approx$ 33 min	500 pulses $\approx$ 250 min	
Tritium retained in the torus before cleaning	1.7 g	11.5 g	
Fraction of tritium removed by cleaning	50%	50% (prior to venting)	requirement close to 100%
Tritium retained after cleaning	0.85 g	6 g	

Table 4.2.6-1. Parameters of the balance of tritium for the experiments carried out in TFTR and JET [415, 419, 420, 18] and foreseen for ITER.

The number of hydrogenic atoms in the surface of plasma facing components that interact with the plasma exceeds in general the total number of ions in the plasma. This leads to a complex coupled system between the hydrogenic species at the wall and the plasma fuel inventory. The recycling and retention behaviour at the walls can strongly affect the fuelling of the plasma whilst the plasma changes the composition of the wall surface. The mechanisms that cause retention of fuel in fusion devices are [274]:

(i) Direct implantation of ions and neutrals in a shallow surface layer and possible diffusion into the bulk. For this mechanism, the wall inventory is determined by material properties, diffusion and recombination coefficients and the concentration/strength of trapping sites. Depending on these parameters, the fuel is retained temporarily ("dynamic retention") or

quasi-permanently by solution and/or trapping. The amount of fuel retained by these mechanisms tends to saturate with time and/or plasma fluence, as the surface layer concentrations reach steady state values and the trap sites are filled.

(ii) Possible production of tritium by transmutation nuclear reactions. This occurs only for special wall materials (e.g. beryllium) and can cause the build up of a tritium inventory within the bulk material by trapping in microscopic defect sites and helium bubbles.

(iii) Co-deposition of hydrogen with eroded wall material forming hydrogen-rich co-deposits inside the fusion device. The rate of retention by this mechanism depends on : a) the rate of erosion of the material and b) the fuel retention capability of the re-deposited material. This retention mechanism is only relevant for few materials (e.g. carbon) in a certain temperature range. For example, diamond-like amorphous carbon films show retention (H/C ratio) of about 0.4 at room temperature, decreasing significantly only above 1000K. On the contrary soft carbon films show a ratio H/C >1 at room temperatures, which decrease strongly with increasing temperature. Because of its physics nature, the amount of fuel retained by this mechanism does not saturate in time and it is, therefore, the mechanism that raises more concern with respect to fuel retention in next step devices.

4.2.6.2. Database on fuel retention in present fusion devices.

The majority of the fuel retention data comes from fusion devices with carbon PFCs. The amount of fuel retention is determined either by comparing the fuel injected to the exhaust ("gas balance") or by ex-situ analysis of wall tiles. The overall tritium balance in the TFTR and JET tritium experimental campaigns showed that 16% (TFTR) and 17% (JET) of the injected tritium was still retained in the device after several cleaning procedures [274]. In TFTR, the tritium is mostly retained at the plasma facing surfaces, with some part on the vessel wall and a significant retention in the gaps between the wall tiles. On the contrary, in JET, the vast majority (> 90%) of this long-term retained tritium was found in carbon layers deposited on water-cooled louvers at the entrance to the pumping plenum at the inner divertor [271]. A minor proportion of tritium was found on plasma facing surfaces and most of it was retained in co-deposited C-layers at the inner divertor. Only a small fraction of the tritium diffused deeper inside the material along the open porous structure of the CFC material [421]. The JET T retention experience is the prototypical for carbon PFCs; the retention of T is associated with the formation of codeposited C-layers while the retention associated to direct implantation and diffusion of T into the CFC matrix is small.

The quantification of fuel retention by the use of tritium has the advantage of being very precise but the disadvantage that these experiments are usually performed under restricted tritium and neutron production limits and, thus, very focused. Therefore, the results obtained may not represent the average fuel retention of the fusion device when operated to address a wide research programme. Because of this, it is important to compare the results

above with those obtained from the retention of deuterium fuel in present fusion devices. Table 4.2.6-2 summarises these observations, which are explained in detail below.

Long-term deuterium fuel retention has been determined at JET by post mortem surface analysis. These results show a large amount of hydrogen-rich carbon deposits at the inner divertor [271]. The total amount of carbon deposited at the inner divertor target is 900 and 500 g for the two divertor configurations explored, MKIIA and MKIIGB divertor respectively, which accumulated during an integrated time of diverted plasma operation of 19 and 16 hours respectively. The corresponding averaged carbon deposition rates were 6.6 10^{20} C/s and 4.1 10^{20} C/s at the inner divertor for the MKIIA and MKIIGB divertors, respectively. This deposition rate corresponds well with the overall amount of carbon eroded from the first wall, estimated from a combination of spectroscopic, carbon screening and Z_{eff} measurements [142]. The location of the deposits that lead to the fuel retention changed significantly in the two divertor configurations. In the MKIIA divertor, particularly for the tritium experiments, the plasma was routinely run on a horizontal diverted configuration, which led to a formation of large deposits near the divertor corner on the water cooled louvers at the entrance of the pumping plenum. In the MKIIGB divertor, the plasma was routinely run on an ITER-like vertical divertor configuration, with pumping through the private flux region, which led to the largest deposits being formed on the horizontal target and on the private flux region components. Due to these different configurations and the larger range of experiments carried out in the MKIIGB divertor compared with the tritium experiments in the MKIIA divertor configuration, there are significant differences in the amount of long-term fuel retained in these two JET campaigns, which is 17 % of the injected fuel for the MKIIA tritium campaign and only 3% for the MKIIGB divertor deuterium campaign [422].

Fuel retention in ASDEX Upgrade is associated with co-deposition of C layers at the divertor with a rate of 3.5 10^{20}C/s, which is similar to the JET values [423]. Most of this deposition occurs at the inner divertor with some deposition taking place the outer one too [423, 424] and, at present, cannot be explained only in terms of erosion of main wall carbon PFCs [285, 424]. Retention of fuel in remote areas of the divertor, such as pump ducts, is very small in ASDEX Upgrade. The films deposited in this area are soft and have a large deuterium content (D/C =0.5-1) but the total amount of carbon deposited in these films is very small (< 1% of the overall carbon deposition). [338].

In TEXTOR, global carbon erosion and deposition balance studies show net-erosion on about 2/3 of the toroidal pump limiter with deposition on the remaining part, on protection limiters and obstacles in the SOL and the pump limiter neutralizer plates. The averaged carbon deposition rate is about 2.5 x 10^{20}C/s, similar to JET and ASDEX Upgrade values. This carbon deposition leads to a fuel retention of 1-2 x 10^{19} D/s, with a typical D/C ratio in the deposited layers in the range 0.05-0.1 [320]. As a consequence, the long-term deuterium retention in TEXTOR is about 8% of the injected fuel [320].

In JT-60U, carbon layers build up at the inner divertor [311], as in JET and ASDEX Upgrade and have reached thicknesses up to 100 μm after the operation period from 1997-2000 in which ~ 8500 shots were performed, leading to a total carbon deposition of 320 g at the divertor, similar to the JET values [425]. The deposition on shadowed areas (mainly on areas in the private flux region viewing the vertical tiles) is much lower than on the target and only ~ 9g C were deposited in these areas during this operation period. The overall carbon deposition at the inner divertor of JT-60U is about 2×10^{20} C/s normalised to the total discharge time or 3.3×10^{20} C/s normalised to the discharge period in which additional heating was applied. Despite this large carbon deposition, the amount of fuel retained in these JT-60U layers is low. This is due to the D/C ratio in these carbon layers being only about 0.015 on average [426]. This is associated with outgassing of the deuterium from these layers under the plasma flux, which is favoured by the relatively high operating temperature of the JT-60U divertor of 600 K [426].

Recently, new attempts have been made to measure the overall fuel retention by particle balance in hydrogen/deuterium operation [427, 428, 429]. This is one of the possible methods to measure the retention of fuel during the initial non-activated phase of ITER operation. In general, these data still suffer from significant uncertainties for a number of reasons, such as the accuracy of the measuring systems, difficulties to account for long term overnight and weekend outgassing, release by daily, overnight or weekend wall conditioning, etc., but progress to deal with them is encouraging. Time-resolved particle balance during long discharges allows the separation between the dynamic and long-term retention in the discharge and could determine the long-term fuel retention in the device. This approach has been followed in Tore Supra (T_{wall} = 400-500 K) [342, 429] with 250 s discharges at low plasma density (1.5×10^{19} m^{-3}). The measurements show a small transient dynamic wall pumping at the beginning of the discharge followed by constant fuel retention at a rate of about 2.5×10^{20} D s^{-1}, which is about 50% of the injected fuel. The amount of fuel retained in the analysed PFCs in Tore-Supra is not consistent with this retention [342] and, thus, further research in this area is on-going to resolve this disagreement. This problem is not only restricted to Tore-Supra, although the disagreement in this device is greatest. In general disagreements by factors of 3 or larger are found between post-mortem analysis and fuel retention determination from gas balance of deuterium and hydrogen discharges due to the difficulties of the latter technique. The agreement is, however, much better for tritium experiments due to the better diagnostic possibilities of the tritium gas balance compared to deuterium/hydrogen [419, 415, 416].

Device/campaign	Average ion flux (lim/div) (D^+-T^+ s^{-1})	Carbon deposition rate (C s^{-1})	Average fuelling rate (D-T s^{-1})	Carbon deposition ratio C/ (D^+-T^+)	Fuel retention rate (D-T s^{-1})	Fuel retention fraction (ret. D-T/ inj.

						fuel)
JET MKIIA div.	$3.8 \cdot 10^{22}$	$6.5 \cdot 10^{20}$		0.037	$5.8 \cdot 10^{20}$ (D/C=0.8)	0.17 (in DTE1)[1] 0.11 (in DTE1)[2]
JET MKIIGB div.	4.3×10^{22}	$4.3 \cdot 10^{20}$	$3.2 \cdot 10^{21}$	0.01	$1.25 \cdot 10^{20}$ (D/C=0.3)	0.03[3]
TFTRT campaign						0.16[1]
AUG		$3.5 \cdot 10^{20}$				0.0353[3] 0.1[4]
TEXTOR	9×10^{21}	$2.5 \cdot 10^{20}$	$1.5 \cdot 10^{20}$	0.029	$1.6 \cdot 10^{19}$	0.08[3]
Tore Supra			$4.6 \cdot 10^{20}$		$2.5 \cdot 10^{20(5)}$	0.5[5]
JT60-U		$2.7 \cdot 10^{20}$			$5.3 \cdot 10^{18}$ (D/C=0.02)	

Table 4.2.6-2: Compilation of fuel retention data from various fusion devices.
[1]T-retention after (non-mechanical) T-cleaning, [2]T-retention after long term outgassing and mechanical removal of accessible T-deposits, [3]D-retention from post mortem analysis, [4]D-retention from fuel balance, [5]D-retention from fuel balance in dedicated long pulse discharges.

4.2.6.3. Fuel retention mechanisms in present devices and implications to ITER.

Since the vast majority of the fuel retention in present carbon-clad devices is by co-deposition of the fuel with eroded carbon, the understanding of the T-retention process is mainly the understanding of carbon erosion, its migration and finally its co-deposition with the fuel to form hydrogen-rich layers. Most of these issues are discussed in Sect. 4.2.1 (SOL flows), Sect.4.2.4 (material migration) and Sect. 4.2.5 (divertor and main wall materials) and we will, therefore, only concentrate on the aspects relevant to tritium retention here.

All divertor tokamaks show net deposition at the inner divertor, while the observations at the outer vary from being erosion-dominated to deposition-dominated. In all cases, the deposition measured at the divertor cannot be explained by local divertor processes and a significant contribution from material eroded at the main chamber wall depositing at the divertor is required to explain the observed divertor deposition. Two major processes are known to be involved in determining the observed carbon deposition at the divertor : local divertor plasma conditions, which favour deposition for low temperature/high density conditions and SOL flows which transport, preferentially, the main chamber eroded carbon to the inner divertor. The final location and amount of re-deposited hydrocarbon layers, which contain most of the retained fuel in carbon-clad devices, depends on local transport processes at the inner divertor. Recent measurements at JET and ASDEX Upgrade have shown that hydrocarbon deposition at the divertor occurs mostly in areas within the line of sight of the

hydrocarbon source at the divertor target. This is because most of the radicals formed there (> 90%) have large sticking coefficients [307, 424], which is consistent with the low amount of redeposited hydrocarbons found in the pump ducts of ASDEX Upgrade and TEXTOR [430, 338].

On the basis of these observations, most of the fuel retained in ITER could be expected to concentrate in areas in line-of-sight from the carbon sources, with only a small fraction of carbon travelling longer distances [431]. In reality, the picture of carbon migration is more complex than this and significant re-erosion of these layers can occur under plasma flux, causing the hydrocarbons to migrate from their initial deposition areas to other areas in which erosion is negligible. This process can take place during the quiescent phases of the discharges, due to the large erosion yields of hydrocarbon deposits under plasma flux [432, 320, 433], or on a discharge-to-discharge basis. In this case, hydrocarbon deposits can be formed in areas of the divertor not in contact with plasma in some discharges, which are then eroded in discharges for which such areas are exposed to plasma flux. Eventually, the retained fuel will be localised in areas not accessible to the divertor plasma flux. Such process has been well documented in JET experiments with Quartz Microbalance monitors (QMB) [434] near the inner divertor corner, whose results for the whole experimental campaigns in the period of three years operation with the JET MkIIGB divertor are shown in Fig. 4.2.6-1. Obviously, due to this hydrocarbon migration, the build up of re-deposited layers, with the corresponding accumulation of fuel, in various areas of the tokamak is very dependent on the detailed experimental programme run in the devices as well as on the divertor target and magnetic geometry of the various discharges executed.

Besides being difficult to predict the expected location of hydrocarbon deposits in ITER, the size of the deposition itself is also uncertain. This is associated with the uncertainties on the chemical erosion yield (source of the hydrocarbons in ITER) for ITER conditions, as discussed in Sect. 4.2.5. A simple empirical extrapolation of the observed fuel retention in present machines, which is dominated by the erosion of the main chamber walls, towards ITER readily demonstrates that T retention would lead to a very short operation time between major clean-up operations if all ITER walls would be made of carbon. Present retention fractions of the injected fuel (from Table 4.2.6-2) are in the range of 3 to 50%. Simulations of ITER plasmas [328] indicate that up to 50 Pam^3s^{-1} of tritium will be injected in the ITER reference Q_{DT} = 10 scenario, which corresponds to 54 g of tritium for a discharge with 400 s of burn. The fuel retention if the ITER main wall would be covered by C would then be in the range 1.6 – 27 g/shot. As a consequence a major tritium clean up operation to remove the retained tritium would be required every 13-218 reference discharges, if the goal of maintaining a maximum in-vessel T inventory of 350 g has to be fulfilled.
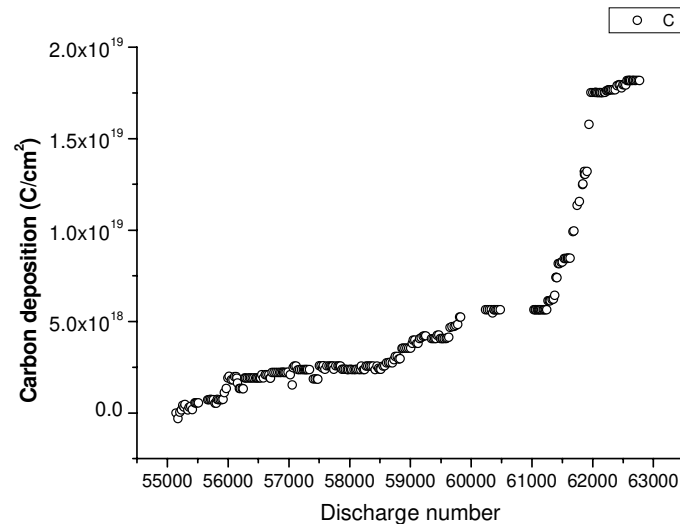
Figure 4.2.6-1. Integrated carbon deposition on the QMB detector at the JET MKIIGB inner divertor during the March 2001-January 2004 period, corresponding to a total exposure to divertor plasmas of 26.4 hours [434].

The extrapolations above (and others which can be done on the fraction of retained fuel normalised to divertor fluxes) are purely empirical and, although they provide a sound argument against a full C wall in ITER on the basis of T retention, do not describe the expected situation in ITER with a full Be wall. More realistic predictions can be done by using Monte Carlo impurity transport modelling codes such as REDEP/WBC or ERO codes [272, 433]. In this modelling, the only source of carbon is sputtering (physical and chemical) at the ITER divertor target and the pathways of eroded species are then followed based on the atomic database, e.g. from [435, 436]. Redeposition and sticking of eroded species is computed using assumptions for the hydrocarbon radicals (such as 1 or 0) or from MolDyn calculations [437] and TRIM data for ions and atoms [438, 439]. The resulting modelled tritium co-deposition is shown in Fig. 4.2.6-2 and varies from ~ 0.02 g to 2 g of tritium retained per discharge in ITER [333], depending on the assumptions for the sticking of hydrocarbons and on the sputtering yield. The reduction of the tritium retention in ITER in the new estimates with respect to those of [440] comes mainly from the inclusion of a more realistic model for the chemical erosion yield in ITER [333], rather than a fixed ~ 1% rate. Besides this, the parameter which influences more the results is the sticking coefficient of the hydrocarbons produced, which can change the calculated retention by a factor of more than 20 when high/low sticking probabilities are considered. As described above, the effective sticking probability of hydrocarbons is affected by their re-erosion (in-shot or shot-to-shot) and it is difficult to predict which will be its value for the ITER divertor conditions. Depending on this value, major tritium clean-up operations will be required in ITER every 600 high performance discharges (i.e., every few months) or just once in the operation lifetime of the device, according to these new estimates, as shown in Fig. 4.2.6-2.
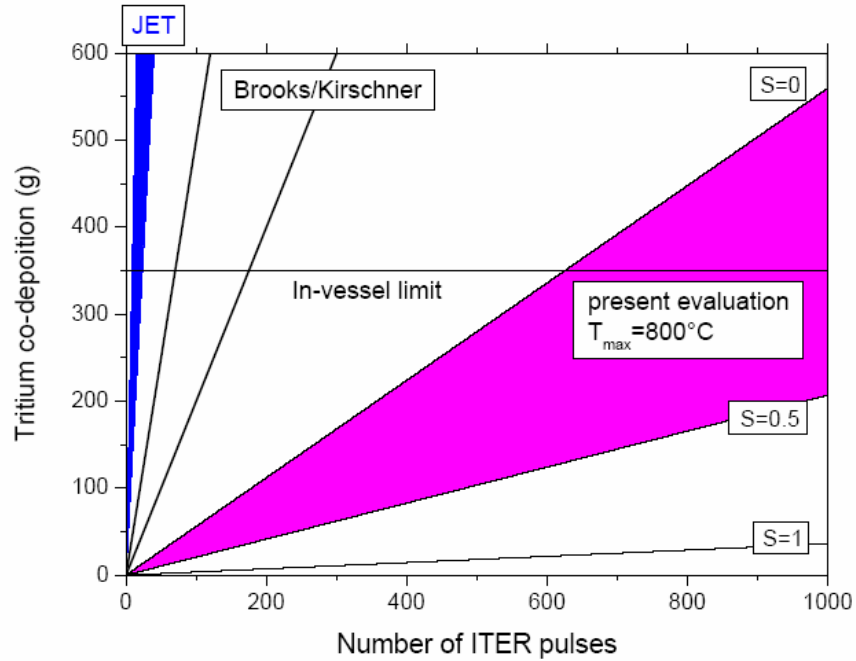
Figure 4.2.6-2. Modelled Tritium retention in ITER based on T co-deposition with a carbon divertor target, showing the expected retention using a fixed chemical erosion yield (1%, Brooks/Kirschner) and using a more realistic chemical erosion formula. Different assumptions are included on the sticking probability of hydrocarbon species returning to the divertor surface (S=1, full sticking, S= 0.5, S=0, zero sticking for hydrocarbons). The solid line shows the goal for maximum in-vessel tritium inventory limit in ITER [333].

It is important to note that the above calculations do not include the additional production of carbon associated with Type I ELMs (see Sect. 4.2.2 and 4.2.4), which would increase the production of hydrocarbon layers, nor the migration of Be eroded from the main wall, which decreases the C surface concentration and, thus, the production of hydrocarbon layers and fuel retention in ITER. Although this will be discussed in more detail in the next section, it is clear that depending on the mechanism that dominates, the T retention in ITER can be much smaller or much larger than that estimated for the inter-ELM conditions shown in Fig. 4.2.6-2.

Recently, attempts have been undertaken to mitigate the formation of carbon layers and the associated retention of fuel by adding certain amounts nitrogen in the divertor region of devices with a carbon divertor target, which cause the formation of volatile radicals. This technique may fulfil both the requirements for divertor radiation control (nitrogen does not affect the chemical erosion of carbon and can replace the carbon as radiator) and low redeposition probability (low fuel retention), which are necessary for ITER. The technique is well known in the field of plasma processing and a factor of five reduction in hydrocarbon deposition has been demonstrated in tokamaks [441], but more experiments are needed in order to confirm its effectiveness and applicability to ITER.

A final point to consider is that the divertor PFCs in ITER will have a significant number of castellations/gaps, which are necessary for the PFCs to withstand the high cyclic

thermal stresses. This creates a specific problem with respect to tritium retention for ITER related to the possible retention of fuel in carbon layers that build up in the larger gaps between the divertor cassettes and the narrower gaps between the tiles of the divertor targets and the castellations themselves. A 5 years period inventory study in TFTR with a total amount of 83 g deuterium into the vessel, revealed a total of 33.6 g of fuel retained from which 47 % was on the plasma facing sides, 15% in the gaps of tiles and 38 % on the vessel wall [274]. During the JET MKI divertor campaign, in which the divertor tiles were ITER-like castellated, about 30% of the fuel retained in the inner divertor layers was retained in the gaps with the rest deposited on top of the inner divertor tiles [442]. At this stage, the comprehensive models of T retention (e.g. the results in Fig. 4.2.6-2) do not include these effects and, therefore, no quantitative evaluation of the expected T retention in tile gaps at the ITER divertor exists. Despite this, initial dedicated experiments to address this problem have shown that the amount of fuel that can be retained in these gaps is large and comparable to that retained in the shadowed areas of the plasma facing components [443].

4.2.6.4. Implication of the ITER wall material choice and mixed material effects on tritium retention.

The results described in the two previous sections come from devices dominated by carbon PFCs, which will not be the case for ITER. In ITER, carbon PFCs are limited to a narrow zone near the strike points in the lower divertor (50 m^2) with a large first wall area covered with Be (700 m^2) and W on the divertor baffle and dome. Due to its low Z and low binding energy, Be will be eroded from the first wall at a similar rate to carbon in present experiments, despite the absence of chemical erosion. The eroded Be will be transported to the divertor where it will deposit. Depending on the SOL flow patterns and local divertor conditions in ITER, this eroded Be will deposit predominantly at the inner divertor (as presently is the case at JET) or in a more in/out balanced way. In these conditions, it is expected that Be will accumulate on the divertor target thus suppressing the production of hydrocarbons at the divertor. This physics hypothesis has been recently demonstrated in experiments at the plasma divertor simulator PISCES-B, in which Be seeding on a plasma in contact with a C target has been shown to decrease to negligible levels the chemical erosion yield of carbon even at Be concentrations of ~ 0.1% [444, 405]. Although the extrapolation of these results to produce a quantitative estimate for ITER conditions is uncertain, it is clear that such effect can have a major effect on tritium retention in ITER by reducing the divertor carbon source and hydrocarbon transport in ITER. The size of this reduction in ITER will depend on the erosion/redeposition balance at the ITER divertors and the expected T-retention by co-deposition (Be can only deposit on plasma exposed areas, while hydrocarbons migrate into shadowed areas [308]), provided that these protective Be layers are not removed by the divertor energy pulses associated with Type I ELMs.

If large areas of the divertor are covered by Be layers, the T-retention in these Be layers may become a serious issue, in particular if the oxygen content of these layers is not sufficiently low. The hydrogenic content of mixed Be/C/O material layers increases with the incorporation of impurities (in particular of oxygen) increasing the expected T retention in ITER due to Be [350, 349]. However, recent experiments from PISCES-B have shown that Be layers formed in realistic ITER conditions [351] can contain much less deuterium than expected from previous measurements [349] so that very small deuterium contents (< 0.01 D/Be) are found for temperatures above about 600-700K (typical of the ITER divertor target) even for ratios O/Be ~ 0.3, as shown in Fig 4.2.6-3. Even if there is significant retention of tritium in the Be deposits, removal of tritium from these deposits should be eased by the fact that the Be layers will only form on the plasma facing sides of PFCs, where they can be more easily accessed for cleaning.

A major advantage of tungsten as PFC is that its retention of hydrogen is negligibly low at the ITER operation temperatures. This has been measured in various beam experiments but also confirmed in the tungsten experiments in present machines [445, 304, 382, 278] and is discussed in detail in section 4.2.5. Due to concerns of the compatibility of a large range of plasma operating scenarios with a full tungsten divertor (including damage under transient loads associated with Type I ELMs and disruptions) this is presently considered only as a back-up option for ITER, should the tritium retention be unacceptable with the reference ITER plasma facing material choice.
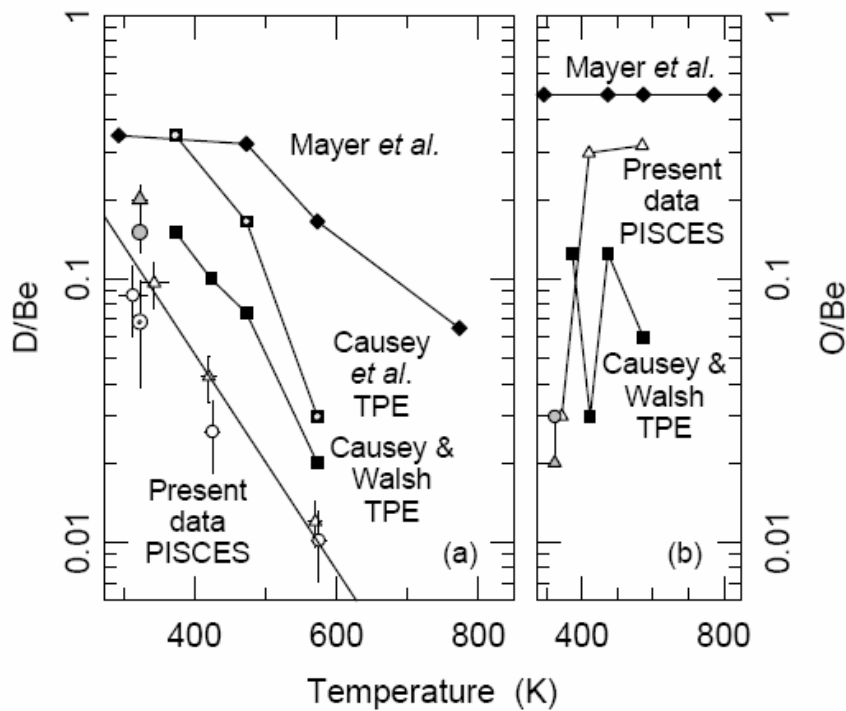
Figure 4.2.6-3. Retention fraction of D in different re-deposited Be layers in various experiments with different oxygen concentrations [351].

4.2.6.5. Dust in Tokamaks (and impact on T-retention).

The subject of dust formation and T retention is reviewed in [274]. In the past, the production of dust has received little attention within the fusion community, mainly because dust is neither a safety nor an operational problem in existing tokamaks. However, in a next step burning plasma device, such as ITER, production of dust could have important safety implications [446, 447]. The safety issues associated with tokamak dust include radiological hazard (tritium and activation products), toxicity and chemical reactivity with steam and air. A variety of products can result from plasma-wall interactions (e.g. deposited films, flakes, debris), as shown by measurements in present tokamaks [274, 448], and many of these products can be considered as 'dust' hazard. The carbon and beryllium dust limits in ITER stem primarily from concerns related to chemical reactivity, whereas the tungsten dust limit is determined both by chemical reactivity and activation hazards. There are still large uncertainties associated with dust production mechanisms in a Be-W-C environment, rates of formation and the determination of the dustquantities. The existing database does hardly permit the extrapolation from present machines to the next generation of tokamaks because of the different material composition of the wall. Despite some new attempts at improving the experimental situation [449], techniques for reliable measurement of dust inventory, particularly in hidden areas, are not well developed, although are needed to ensure compliance with regulatory limits. Similarly, dust removal methods are not developed. Several methods for the removal of dust-forming co-deposits have been proposed [450], but they have not been tested and qualified enough with respect to their application for ITER.

4.2.6.6. Tritium removal methods.

As highlighted before, the working guideline for the maximum in-vessel inventory of tritium that can be mobilised in the ITER vacuum vessel is presently ~ 350 g. The assumption made for safety analysis is ~ 1 kg of tritium mobilisable in the vacuum vessel [134]. Therefore, operation of ITER will require periodic removal of tritium captured in in-vessel deposits in order to avoid approaching this limit. Techniques for tritium removal are only partially developed at present and usually not demonstrated in a tokamak environment. TFTR and JET have intensively explored various T-removal techniques but the methods suffer in general from the fact that they are too slow to cope with the higher duty cycle of a next step device and that they act mainly on the plasma facing surfaces [451].

The presently foreseen methods to remove tritium from ITER are reviewed in [419, 415, 417] and can be roughly divided into four categories :

a) Plasma cleaning. On areas in direct contact with the plasma, T retention can be reduced by isotope exchange during deuterium plasma operation or desorption by plasma heating of the material. Plasma heating or isotope exchange are restricted to areas of direct plasma impact but are difficult to apply on remote areas or gaps in between tiles.

b) Surface heating. This can be achieved by heating the redeposited hydrocarbon by external means such as a laser or flash lamp [452], leading to the release of fuel or the ablation of the film itself. Along these lines, the use of the end of plasma discharges in ITER for tritium removal by inducing a radiative collapse similar to that of mitigated disruptions has been considered [354]. The major problem of the applicability of such technique in ITER is that it requires a very high level of reproducibility, to avoid causing frequent large-scale melting of the Be wall, which could impact very negatively on the operability of ITER. Even if successful, the isotropically emitted radiation pulse is unlikely to illuminate the areas in the divertor where the highest deposition is expected to occur. In addition to the various issues related to their practical application in tokamaks (i.e. accessibility of the electromagnetic radiation to the redeposits), such methods can cause an uncontrolled production of dust, which is a concern for ITER.

c) Oxidative methods. The most promising method in this line is the removal of the C-deposits by oxidation, which transforms the carbon into CO and CO_2 and thereby releases the incorporated T, mainly in form of tritiated water [453, 454]. A good database from laboratory experiment exists on the oxidation of different carbon films by molecular oxygen [455, 456] but the experience in fusion devices is limited. TEXTOR has demonstrated the removal of carbon films by oxygen venting of the device at 620 K and successfully recovered plasma operation with standard conditioning (He and D_2 GDC) for these conditions [457]. However, the technique has serious drawbacks, such as the required wall temperatures difficult to achieve in ITER, which should be above 550 K, the interaction with other non-carbon in-vessel components (such as Be), the recovery time for normal plasma operation and the processing of the resulting tritiated water. Recently, ozone has been shown to oxidise carbon layers at significantly lower temperature compared with molecular oxygen [458], but this method has not been yet demonstrated in the tokamak.

d) Conditioning methods. Wall treatment with RF conditioning plasmas in the presence of the toroidal magnetic field have been further explored [459, 460, 395], as described in Sect 4.2.5.5. These techniques have shown to be effective for releasing the retained fuel from the material elements facing the plasma, which may open options for their use in ITER to release tritium from surrounding walls by their routine application between discharges.

More experiments are necessary to demonstrate the effectiveness of these techniques, the recovery of released tritium, the interaction with the non-carbon ITER wall materials, the handling of the debris that is potentially produced by ablative methods and the recovery of

plasma operation, before a credible tritium clean up schedule and their consequences for ITER operation can be evaluated in a quantitative way.

4.2.7. Plasma Fuelling.

4.2.7.1. Separatrix density.

The separatrix serves as the key interface between the pedestal/core density, as requested by core operational and burn criteria, and the divertor particle and energy exhaust, which are controlled by the neutral pressure. The separatrix density is determined to a large extent by the power flux and pressure balance via SOL and divertor physics, which affect the ionisation of neutrals at the plasma edge. Ideally, in a burning plasma the separatrix density should be regulated at a value corresponding to the maximum divertor heat dissipation and particle exhaust, while the core and pedestal plasma densities should be optimised for the optimum core performance. However, through anomalous transport, particularly in H-modes [22], and edge ionisation physics, the separatrix density is tightly coupled to the pedestal density [461, 462, 463], which constitutes a major fraction of the line average density in H-modes (see Sect. 2.4). Therefore, controlling the ratio of separatrix to line average density to meet the requirements for both core confinement and divertor heat load is expected to be a challenging task and may make it necessary to operate a burning plasma device at a density which is not optimum for either requirement.

Assuming a fixed density peaking factor (n_{line} / n_{ped}), the following knowledge is required to design the optimum operating density point of a device :

1- Acceptable operating range of pedestal densities with sufficiently high pedestal pressure.
2- Core performance as a function of core and pedestal density.
3- Range of separatrix densities that can be obtained for a given pedestal density.
4- Divertor performance as a function of the separatrix density

Of particular importance for item 3 is the physics that determines the steep density gradient zone up to the pedestal top. In order to address these points, a new multi-machine database for the separatrix density and related quantities has been set-up for H-mode conditions [464]. It contains experimental data from Alcator C-Mod, ASDEX Upgrade, DIII-D, MAST, JET and JT-60U gas fuelled discharges with NBI and ICRH additional heating in H-mode confinement. The bulk of the measurements consists of electron density and temperature measurements by Thomson scattering, supported by probe measurements in the SOL (JT-60U) and lithium beam measurements and modelling (JET) [22]. A two-point model based on power balance [465, 77] is used to assign the separatrix location for cases where the uncertainties of the equilibrium reconstruction are comparable to the density decay length. The noisy experimental data are fitted and regularized by a modified hyperbolic-tangent function [67]. The data have been restricted to conditions without strong core density peaking.
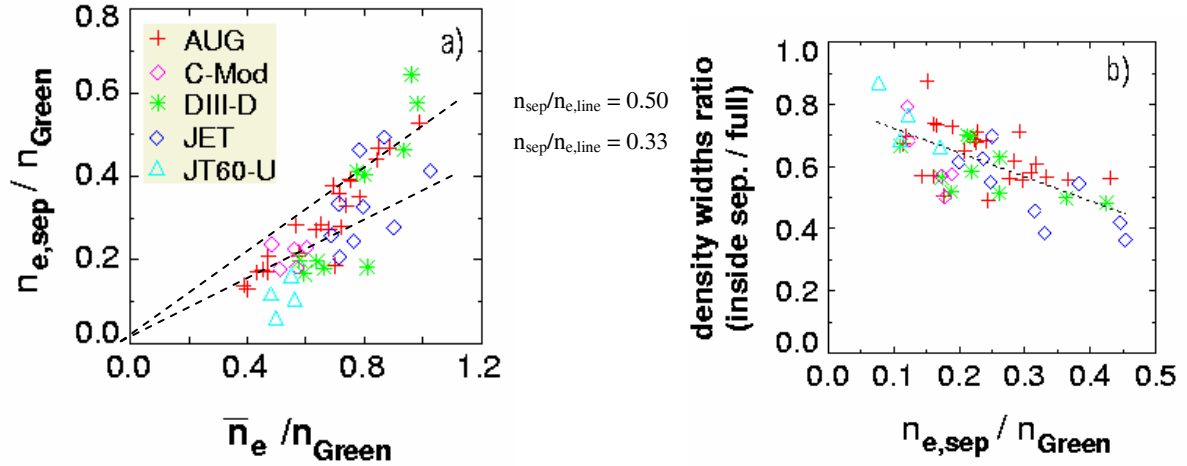
Figure 4.2.7-1: a) separatrix density versus line-averaged density, both normalized to the Greenwald density for H-mode discharges in several tokamaks, the dashed lines correspond to two different ratios of the separatrix to line average density and are drawn to guide the eye. b) fraction of the steep density gradient region inside the separatrix for the discharges in a) versus separatrix density normalized to the Greenwald density [464].

The normalized separatrix density, n_{sep}/n_{Green}, from the multi-machine data is shown in Figure 4.2.7-1.a versus the normalized line-averaged density. The Greenwald density provides an excellent normalisation of the data, which vary, e.g., by a factor of 30 in absolute value between C-Mod and JT-60U. For low Greenwald fractions (f_{Green}), the line-averaged density is a factor of 3 larger than the separatrix density, while this factor decreases to less than 2 for high values of f_{Green}. Figure 4.2.7-1.b shows a plot of the fraction of the steep density gradient region width inside the separatrix (or pedestal density width), δ_{in}, in relation to the full width of the steep gradient zone, δ_{tot}, versus the normalized separatrix density. The negative slope indicates an outward shift of the steep gradient zone with respect to the separatrix with rising density. Example profiles can be found in Fig. 11 of [22] .

An analytic gas fuelling model [466] describes many features of edge density profiles by neutral penetration physics. Figure 4.2.7-2 shows modelled DIII-D density profiles. Consistent with data of figures 4.2.7-1.a and 4.2.7-1.b, the ratio of the separatrix to pedestal density increases with increasing pedestal density while the profile width inside the separatrix becomes narrower. According to the model δ_{in} tends to scale as $\sqrt{Ti_{ped}}/(\,n_{ped}.E^{*})$, where E^{*} is a measure of the poloidal distribution of the neutral source relative to the X point. E^{*} is largest when the neutral source is concentrated at the X-point, the location of largest flux expansion. In addition to the direct effect of the local neutral sources as implemented in the simple model, radial particle transport around the separatrix [77] and neutral screening in the SOL plasma [58] affect the density profile shape.
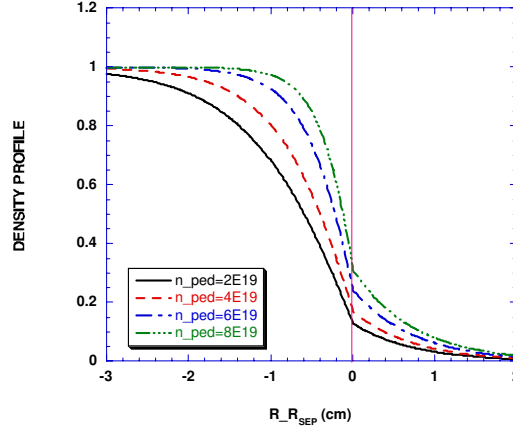
Fig. 4.2.7-2. Modelled DIII-D density profiles, normalised to the pedestal density. With increasing n_{ped}, the width of the density pedestal becomes narrower while the ratio of separatrix to pedestal density increases [466].

The density width data shown in figure 4.2.7-1.b are better organized when plotted versus the n_{sep} normalized to the Greenwald density. While the outward shift of the steep gradient zone of the density profile with increasing n_{sep} can be understood as an effect of the neutral ionisation location, the dependence on the Greenwald density suggests an impact of transport effects. One obvious effect is the dependence of the diffusion coefficient on the plasma current. Another possible player is the radial SOL particle flux caused by intermittent events [195, 49], which has been observed to increase strongly in Alcator C-Mod when the density is increased towards the Greenwald value [128]. This rise in radial transport is accompanied by larger wall fluxes and, therefore, affects the neutral fuelling in the SOL as well as in the pedestal regions. Since at least three different, complicated mechanisms (neutral penetration, transport in the edge barrier region and SOL transport linked to main chamber recycling) affect the edge density profile, further inter-machine scalings, derived from more complete databases, and detailed comparisons with code modelling are necessary, and in preparation, to disentangle the interplay of these processes.

There are practical operating windows for both the pedestal and separatrix densities. The lower limit on the separatrix density is set by the divertor heat flux. B2-Eirene modelling of the ITER edge plasma with 130 MW of heat flux across separatrix shows that a minimum separatrix density of $4 \ 10^{19}$ m^{-3} is needed for an acceptable peak heat flux [29, 253, 20]. An upper limit on the separatrix density is set by energy and momentum balance in the SOL [467] and by volumetric recombination in the divertor plasma [468]. Scaling from DIII-D [466] sets an estimated upper limit of $6 \ 10^{19}$ m^{-3} for ITER, assuming Bohm transport scaling in the SOL and open geometry. It is conceivable that there are more restrictive limits on the separatrix density due to its effect on H-L transition or onset of type-III ELMs. However a causal relationship has not, so far, been established between separatrix density, H-L transition or type-III ELMs. Therefore, further theoretical studies should be pursued to guide the experimental and modelling progress in these issues.

Pedestal densities as high as 90% of the Greenwald limit, with no confinement degradation, have been achieved in DIII-D [463] and in type-II ELMy discharges in ASDEX Upgrade [469]. This has been exceeded in JET with highly shaped discharges, in which pedestal densities up to $n_{ped}/n_{Green}=1$ have been reached [470]. Because of the coupling of separatrix and pedestal densities with standard gas fuelling, a sufficiently high pedestal density may not be accessible in ITER. Alternate fuelling techniques, which provide a higher particle source at the pedestal top, are discussed in sections 4.2.7.2 to 4.2.7.4.

4.2.7.2. Supersonic gas jet and low field side puffing.

Supersonic molecular beam injection (SMBI) offers a potentially superior fuelling technique compared to cold gas fuelling and is technically simpler in comparison to pellet injection (PI). Main features of SMBI are a higher molecular speed and lower divergence compared to gas puffing (GP). SMBI has been implemented on the HL-1M tokamak [471, 472], the HT-7 tokamak [473] and the W7-AS stellarator [474]. A Laval nozzle is utilized to inject a well collimated supersonic jet in the plasma (typically 5 10^{19} particles per pulse with an injection time ranging from tens to hundreds of ms [471]). Gas speeds higher than 1 km/s have been obtained [475], to be compared with 300 m/s typical of gas puffing.

On the Tore Supra tokamak, a repetitive SMBI system with a fast mechanical valve has been installed, allowing use of a shorter injection time (2 ms) and a high injection rate (10^{23} particles s^{-1} or 200 Pam^{3}s^{-1}, corresponding to 2×10^{20} particles injected per pulse) with a repetition rate up to 10 Hz [476]. Figure 4.2.7-3 shows a comparison of the achieved plasma particle content for the 3 fuelling methods (SMBI, GP and low-field-side PI) with a roughly equivalent number of particles injected. As observed in the other experiments, the main results obtained with SMBI are an improved fuelling efficiency (in the range 30-60 % to be compared with 10-15% for conventional GP and up to 80% for PI) associated with a strong plasma cooling [476]. A reduction of the hydrogen wall inventory has been achieved in Tore Supra long discharges comparing GP and SMBI [477, 478] when the injected quantity per pulse is significant compared to the plasma content (~ 50 % in the above experiments), inducing a strong perturbation of the plasma and a short detachment phase after each injection. This effect is not observed with injection at a lower rate. An attempt was made on ASDEX Upgrade to use the perturbation by the SMBI to trigger ELMs in the type-I ELMy H-mode, as has been done with shallow pellets [479]. While a better fuelling efficiency of the SMBI compared to gas puff was observed, the instantaneous triggering of ELMs could not be achieved [480], probably due to a not sufficiently deep neutral penetration.
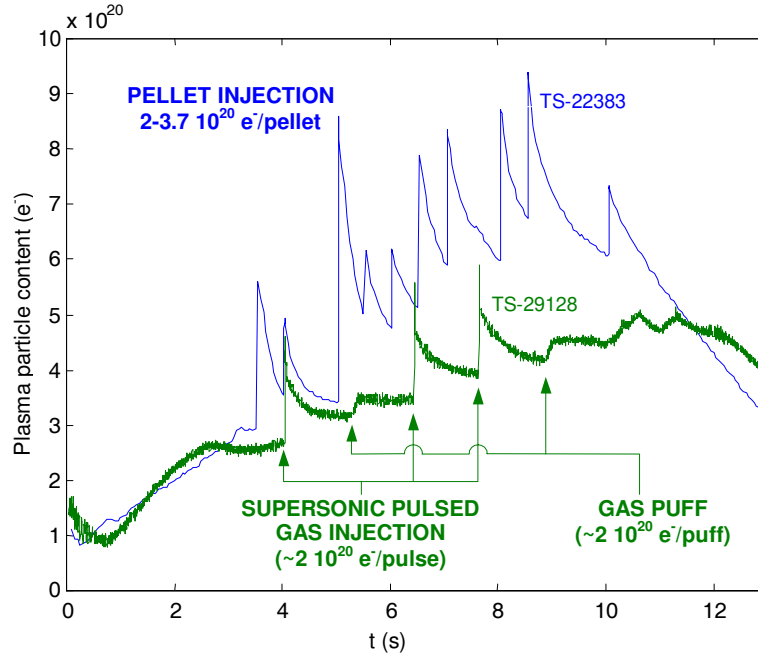
Figure 4.2.7-3: comparison of the plasma particle content behaviour for 3 fuelling methods (SMBI, GP and low field side PI) for the same number of particles injected on Tore Supra [476].

The dependence of the gas fuelling efficiency on the fuelling location has been investigated in DIII-D [481]. Inner wall gas fuelling did not show the significant increase in fuelling efficiency as observed with pellets [482]. This is explained by the poorer penetration depth and a lack of significant polarization drift effect [483] with gas puffing. The enhanced fuelling efficiency of SMBI is also not attributed to a polarization drift, since the beam density is estimated not to be high enough to trigger collective effects. Simulations with a 1D particle transport model taking the plasma cooling into account have shown good agreement with the experimental results [484].

4.2.7.3. Pellet fuelling.

As discussed above, for efficient core fuelling, deep pellet particle deposition is required. Key parameters for the determination of the pellet penetration depth Δ are : plasma density n_e, temperature T_e, pellet mass m_p and velocity v_p. A multi-machine study [485] has confirmed the neutral gas shielding scaling of the penetration depth $\Delta \sim n_e^{-1/9} T_e^{-5/9} m_p^{5/27} v_p^{1/3}$ for outboard launch. The absolute pellet penetration depth for inboard launch is about twice that of the outboard launch. The deeper penetration of the high-field-side injection [482, 486] is attributed to the ∇B and outward curvature-drift force on the plasmoid formed around the pellet [487, 483, 488]. The observed increase in penetration depth with inboard launch has been confirmed in several machines [489, 490, 491, 492]. Inboard launched pellets must be transferred through a curved guiding system, which limits the pellet speed. Currently, the fastest pellet accelerators, based on the multi-stage gas gun principle can launch pellets at up to 4500 m/s [493]; whereas, highest pellet speed achieved in a centrifuge, which is more

suitable for steady state operation, is 1200 m/s [494]. A repetitive injector, able to operate at a frequency higher than 10 Hz, has also been developed for continuous fuelling [495] and successfully tested on long discharges in Tore Supra [496].

The planned ITER fuelling system is based on a centrifuge injector launching pellets at the high field side via a transfer system suitable for speeds up to 500 m/s [497]. Central fuelling is questionable with this system, even when the beneficial effects of high field side launch are taken into account. [498] calculated the penetration of pellets in ITER with a size d = 6.6 mm and a speed of 500 m/s with the integrated ablation/mass relocation model SMART, which had been benchmarked for pellet injection experiments in ASDEX Upgrade and DIII-D [499], as well as for HFS edge-localized absorption in JT-60U [491]. The resulting deposition is entirely outside r/a= 0.65; this is not adequate for central fuelling but very suitable for increasing the pedestal density. The same system will be used for the triggering of ELMs with the aim of reduction of the ELM amplitude [498]. This concept is based on ASDEX Upgrade observations, which show that pellets can trigger high frequency Type-I ELMs with a lower energy loss per ELM relative to the naturally occurring ELMs, with no significant confinement degradation [148].

4.2.7.4. Compact toroid fuelling.

Compact toroid (CT) fuelling involves the injection of dense, self-contained magnetic plasmoids to achieve deep fuelling (see ITER Physics Basis Ch 3.5.3 and references therein). Possible benefits of CT injection, with respect to other fuelling techniques, are the possibility of deep fuelling and the controllability of the fuelling location, which may be essential for the fuelling of steady-state advanced tokamak plasmas in burning plasma experiments. CT injection into tokamak plasmas was pioneered in TdeV [500] and was investigated in JFT-2M [501]. CT injection has not matured into a continuous standard fuelling technique so far. Reasons for this are the technical complexity of the injector and the fact that the CT length is comparable to the plasma radius in small tokamaks.

4.3. Modelling and Theory.

4.3.1. Introduction.

To date, tokamak divertors and wall systems have been designed largely on the basis of empirical extrapolation supported by basic theoretical concepts, and this remains the principal means of proceeding to ITER. Computer-based modelling greatly assists this process by identifying the potential role of presently known edge effects, through the construction of self-consistent 'thought experiments'. Edge code modelling also aids in the identification of controlling physics, by pointing to quantities whose measurement in existing tokamaks can expose those effects and their role. Empirical extrapolation requires sufficient

theoretical understanding to be able to identify scaling factors, and while present edge code-modelling is not usually capable of detailed prediction, it can be capable of the identification of trends, as required for scaled extrapolation. Edge code modelling, therefore, continues to play a central role in the design of the ITER divertor and wall system. We have to be aware, however, that present codes use a diffusion type ansatz as basic paradigm for anomalous transport across field lines, which is hard to justify in the edge region, where the gradient length and the different scales determining turbulence (notably ρ_i) approach each other.

Edge code-modelling is instrumental in addressing a number of ITER edge issues, e.g. the operational window for acceptable target power, helium exhaust, target lifetime, impurity migration, tritium retention, core boundary conditions, etc. Significant progress has been made since the IPB [18] in a number of theory and modelling issues, including code developments in neutral/radiation transport, study of fast ion effects, ELM buffering, preliminary drift modelling – including replication of power asymmetry scaling in JET for example, etc. The identification of outstanding problems has also continued including validated/routine application of drifts, modelling hydrocarbon migration, the issue of how to deal with peripheral turbulent transport and main wall interactions, ELMs, difficulties in describing the details of detachment, etc. In the rest of this section some of these matters are described in detail, however, space limitations prevent comprehensive coverage and the selection of topics, inevitably somewhat arbitrary, aims at touching on a few recent high points.

4.3.2. Progress in ITER divertor modelling

In section 4.3.2.1 we describe the current status of the models used to analyse the ITER divertor performance, emphasizing the logics backing the parameter choice. Although some of the assumptions may be challenged, these are the models on which a number of ITER design solutions are based (section 4.3.2.2). An outlook towards further model development relevant to ITER (or other reactor-grade experiments) is given in section 4.3.2.3.

4.3.2.1. Model parameters.

The computational models contain a number of free parameters representing such quantities as anomalous cross-field transport, semi-empirical kinetic corrections to the parallel transport, and boundary conditions, reflecting the incomplete present state of knowledge of the physical models describing the transport processes in the edge plasma. In interpretative mode, these free parameters are adjusted to fit the experimental data; this leads to different values of cross-field diffusivities resulting from fits to different experiments [502] (see also section 4.2.1). Predictive modelling, such as extrapolation to ITER, requires then a choice of these free parameters on the basis of other constraints.

For a given input power, the width of the SOL temperature profile upstream is determined primarily by the ratio of the cross-field to parallel thermal diffusivity (see also section 4.2.1), and the temperature itself is determined by the values of these diffusivities. Parallel transport is modelled by classical Spitzer-Härm heat conductivity with "flux-limit factors" (FLF) [18], which partially account for kinetic effects (the depletion of the high-energy tails of the particle distribution functions at low collisionality). From kinetic modelling [503] based on a hybrid, fluid-kinetic model [504], a value of the FLF for electron heat conductivity of 0.2 is selected for the ITER calculations, whereas for technical reasons, no FLF is used for ion heat conductivity in these calculations. The cross-field transport, which determines the profile, should then be constrained by considerations of Larmor radius and stability. First, the profile width must be larger than the poloidal Larmor radius of the ions, which is the measure of radial excursion of the banana particle orbits in the SOL, thus eliminating for ITER modelling the lower of the diffusivities fitting the experiment [502]. Secondly, there is no experimental evidence that radial gradients in the SOL can be steeper than those just inside the separatrix [505, 22] (see also sections 4.2.1.1 and 4.2.7), which are determined, apparently, by stability. The gradients limiting the plasma stability just inside the separatrix can, therefore, be taken as constraints also for the radial gradients in the SOL. These constraints are consistent [506] with a choice of $\chi_{\perp i} = \chi_{\perp e} = 1$ m^2/s and $D_\perp = 0.3$ m^2/s for the cross-field transport in ITER modelling, resulting in a typical width of the power load profile around 5 mm when projected to the midplane, and in a radial pressure gradient in the midplane close to the experimental ballooning limit. Sensitivity studies in [507] show that reduction of these diffusivities by a factor 2 produces the same effect on the peak power loading as an increase of the input power by 25%, i.e., less than the size of the operating window, see section 4.3.2.2. Intermittent transport events leading to flat profiles in the Far SOL (see Section 4.2.1.3) may be related to the profile readjustment necessary to maintain the Near SOL profile near the limit, corresponding to the above specification of the transport; they are not explicitly included in the ITER modelling but may affect erosion processes at the walls. Although a radial pinch may be important to fit some present experiments [508, 126], it is not used in ITER modelling because the classical Ware pinch [509] is unlikely to be important (the loop voltage in ITER is expected to be very low), and present knowledge is not sufficient to extrapolate an anomalous pinch velocity to ITER.

The boundary conditions also require a choice of free parameters. At the target, the most important region for the solution, the boundary conditions are well-established [18], at least for the conditions investigated so far, in which drifts and electrical currents are assumed to be of minor importance only [510]. Near the side walls, radially far from the separatrix (low power levels), the boundary conditions are complicated by the fact that the computational grid has to follow the magnetic surfaces which do not conform to the first wall. Moreover, a high triangularity of the plasma column, required for better performance of the

core plasma (see chapters 2 and 3), brings the second x-point in ITER slightly inside the first wall. Initial modelling studies of double-null divertor configurations for ITER [511] showed the expected target loading of the secondary divertor to be below 2 MW/m^2, provided that the distance between the separatrices is at least 2 cm at the outer mid-plane, and this requires no special target design. This allows to simplify the modelling configuration, and in the recent ITER calculations, the grid is limited radially by the second separatrix, leaving a gap to the real wall. To account partially for the presence of a plasma in this gap and to simulate wall recycling and erosion, a gradient scale length of 3 cm is specified at the last magnetic surface boundary for all densities and temperatures (equivalent to a specification of an outward convection with $v_\perp = 10$ m/s for all ion species, which contributes a constant 43% of the energy outflow at the grid edge [512]), and a condition of non-slipping ($v_\parallel = 0$) is applied for the momentum equations. As concerns the neutrals, the Monte-Carlo neutrals are allowed to travel freely in the gap, although in reality there would be some plasma-neutral interaction there. Both approximations are justified by the low power flux (several percent of the input power) crossing the boundary surface, which renders it unlikely that the exact values chosen will have a strong impact. However, no sensitivity studies have yet been done for these parameters, and the model used for the plasma transport boundary conditions lacks a first-principle based theoretical justification. Recently, the importance of substantial plasma-wall contact – additional to the plasma-target contact – has been demonstrated experimentally, and model developments are proceeding to include this new physics element.

Generally, the specification of the material properties on the plasma facing components (PFCs) may have a strong influence on the results obtained in the modelling studies. In long-pulse reactor operation, the state of the surface should reach equilibrium at every point with the impinging particle fluxes with regard to erosion and re-deposition, i.e., the boundary conditions evolve in the course of the iterative solution along with the local plasma parameters. Specifically, a pure metallic surface, which would absorb all the incident carbon, does not retain this property: at low incident DT fluxes (deposition-dominated) a carbon layer builds up and the surface properties become those of deposited carbon, whereas at high incident DT fluxes (erosion-dominated) the surface properties are those of the metal and all the deposited carbon is re-eroded. Interpretative impurity transport modelling has had only limited quantitative success so far in the cases where chemistry is significantly involved (in particular chemical sputtering and hydrocarbon chemistry). Nevertheless, based upon best guesses for the relevant rates, first studies of this effect for ITER conditions ([513, 512]) have been attempted. They result in an increase of Z_{eff} at the separatrix to a value ~ 1.7, accompanied with a shift of the operational window towards lower densities. In case of a constant chemical sputter yield, Y_{ch}, they predict for ITER a carbon deposition from plasma ions on the lower outer part of the first wall just above the outer baffle, which disappears if

the Y_{ch} for the deposits is an order of magnitude higher [512]. Note that the deposition occurs on a time scale of 10 s, i.e., equilibrium would be reached within a single shot.

There are very few free parameters in the Monte-Carlo part of the code, although some free parameters may be inherent in the data on particle-wall interaction calculated with the TRIM code [438, 439]. A fixed value, $Y_{ch} = 0.01$, is chosen as the standard value in the ITER modelling. This selection was reasonable given the spread of the experimental data on chemical erosion of carbon materials [18]. Recent data suggest that this modelling may have to be improved to account for the flux dependence of the sputtering yield [333] and the possible differences in sputtering yields of solid and re-deposited carbon surfaces [514].

Recent development of the neutral transport model for ITER involves also inclusion of neutral-neutral and molecular-ion collisions, besides the elastic collisions of helium atoms with plasma ions, in the calculations [515].

4.3.2.2. Modelling results.

A number of modelling results on the performance of the ITER divertor have been obtained in last five years [511, 516, 253, 29, 517, 20, 513, 512, 515] as new experimental results have been obtained, further physical effects have been included and a design optimisation of ITER toward lower cost has been performed. The primary aim of the studies has been the identification of the major control parameters, the exploration of the operational window, the investigation of the effect of divertor geometry, and the development of integrated modelling of the whole plasma by coupling of the edge and core models at their interface. The B2-Eirene code package, version SOLPS4.0 [518] with some reactor-specific modifications [253], has been used in the ITER divertor modelling – see the previous sub-section for the model details.

In ITER modelling, fast transients such as ELMs are not included explicitly. The resulting state, therefore, describes a time-averaged base state perturbed by ELMs. Such an approach, forced by the lack of a proper ELM model, can be justified by noting that in ITER less than 25% of the average power is expected to be transferred by ELMs [4], and by the fact that the modelling region in the 2D calculations here does not include the pedestal. It can of course not cover strongly non-linear effects arising from large individual ELMs – like massive evaporation of target plate material – but these aspects are dealt with in section 4.2.2. The results of the time-averaged modelling can be briefly summarized as follows.

Six major control parameters for the edge plasma are identified as: (1) power entering the SOL, P_{SOL} – strongly affects all the parameters; (2) D/T neutral pressure in the divertor p_{DT} – strongly affects the peak power loading on the targets, together with the helium and carbon concentrations at the separatrix, c_{He} and c_C, and determines the degree of detachment of the plasma from the targets; (3) pumping speed and (4) fusion power – both affect c_{He}; (5) the distribution of fuelling between gas puffing and core fuelling – affects the neutral influx to

the core Γ_{DT}, plasma density at the separatrix n_s, and c_{He} and c_C, and (6) the connection length (differing between inductive and continuous operation scenarios) represented through the q_{95} value – affects the upstream plasma parameters [20, 512]. These simulations have shown that an operational window in these parameters, with acceptable power loading $q_{pk} \le 10$ MW/m^2 and sufficient helium removal rate, exists and extends to P_{SOL} at least 50% higher than the nominal ITER value of 86 MW. A certain margin to cope with uncertainties and flexibility in divertor parameters therefore exists. Recent modelling has shown that helium removal from the edge plasma is not a severe constraint, once the elastic collisions of He atoms with D/T ions are taken into account [253, 517, 252]; this relaxes the requirements on pumping throughput. Taking into account the neutral-neutral and molecule-ion collisions shifts the operational window towards higher p_{DT}, 5 to 15 Pa [515], thus alleviating pumping. The modelling predicts saturation of the separatrix ion density as the throughput increases, as well as high opacity of the hot ITER SOL to neutrals, rendering necessary the implementation of core fuelling techniques such as pellet injection [253, 20] in order to maintain the required density in the core in ITER.

Modelling for ITER has indicated the importance of two geometrical features in particular and these have been ensured in the design. First, a V-shaped intersection of the targets and the divertor floor is found to enhance the neutral compression near the separatrix strike point and to facilitate partial detachment [253, 202, 519]. Secondly, high gas conductance of the structures supporting the dome was found to be essential for reducing the in-out divertor loading asymmetry [253, 224].

A power law parameterisation of the results of 2D modelling in terms of the control parameters described above and the interface parameters at the separatrix such as n_s, Γ_{DT}, c_{He}, c_C, plasma temperatures, etc. has been developed [517, 20, 512] providing a set of boundary conditions for the core plasma models and thus allowing consistent modelling of the whole ITER plasma [520, 521, 522]. Moreover, the results obtained with different assumptions on the surface composition can be put in a linear order and be then unified in the same scaling by introducing one more artificial input parameter [512]. Fig. 4.3.2-1 illustrates the quality of the obtained scaling [512]. Besides providing the boundary conditions for core modelling, the identified scalings of divertor plasma conditions also serve as a framework for comparison between calculations done with different models, allowing reliable quantification of the effect of different modelling assumptions [515].

4.3.2.3. Future improvements to the physics model

A significant future improvement to the physics modelling used in the ITER modelling studies will be the incorporation of drifts and currents in the edge plasma. Whereas a model of the drift effects is already included in some versions of B2-Eirene [518, 124, 523], this rather complex extension to the code affects the running time and stability of the code,

and its routine use for ITER modelling can be envisaged only once further tests and verification against experimental data are carried out. Its incorporation would be expected to have only a moderate effect on target loading in ITER. Indeed, since the in-out power asymmetry for ITER is already 2:1 (Shafranov shift) [20], a further increase of this ratio would be similar to an increase of the input power by 20%, i.e. within the operating window margins. A reduction of this asymmetry would lead to a reduction of the power loading of the outer divertor, which is not dangerous, and an increase at the inner divertor target, which is anyway designed for the same power loading as the outer one. The expectation that impurity transport in the SOL would be affected significantly is not supported by first modelling results for ASDEX-Upgrade [523], although the net erosion-deposition pattern can change.
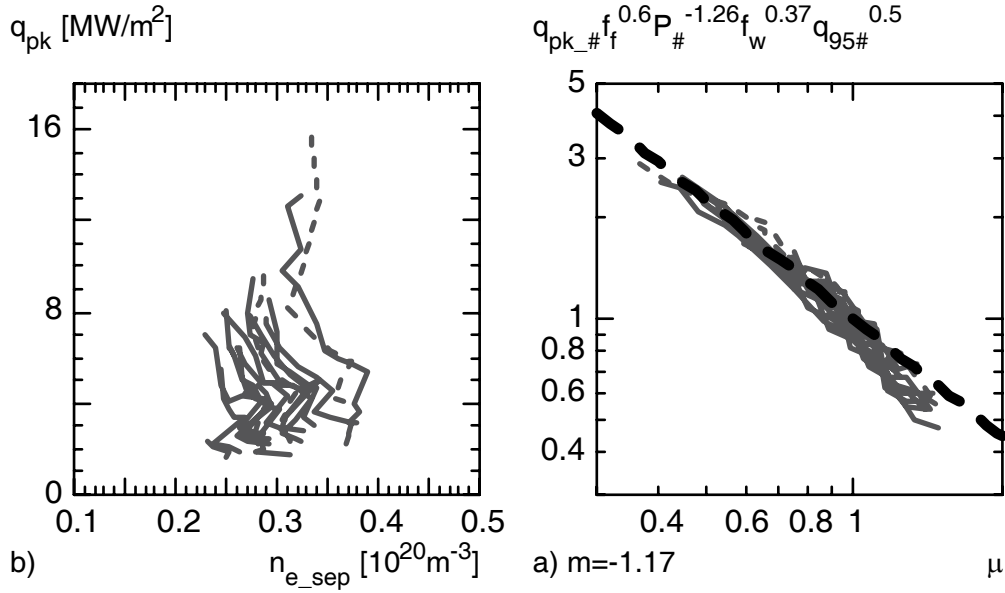

Fig. 4.3.2-1. Quality of the divertor parameter scaling [512]: the raw data in terms of q_{pk} vs. n_s (left) and the same data after the proper normalisation (right). The individual curves correspond to a density variation for different values of the input power (80 to 130 MW), different operational mode (inductive vs. steady state), different fuelling scheme, and different assumptions on the erosion/deposition properties of the walls. Here $\mu \equiv p_{DT\#}\, P_{SOL\#}^{-0.87}\, f_f^{-0.8}\, f_w^{-1}\, q_{95\#}^{-0.27}$ is the normalised neutral pressure in the divertor, $f_f \in [1, 1.2]$ and $f_w \in [0.7, 1.1]$ are the factors quantifying the fuelling scheme and the surface properties, and the sub-script # means normalised value of the corresponding parameter. Further detail can be found in [512].

Several important items remain to be implemented in the neutral transport model. These are Lyman radiation transport and hydrocarbon generation and dissociation. The first may have a considerable effect on saturation of the plasma density since excitation of neutrals during absorption of radiation (optical pumping) facilitates their ionisation and changes the ionisation-recombination equilibrium, resulting in higher ion density. This effect, already included in an experimental version of Eirene [524], will soon be included in ITER modelling

(see sect. 4.3.4). Explicit modelling of hydrocarbons can be implemented in the future following assessment and validation of the detailed surface interaction processes and would then allow improved modelling of tritium co-deposition. Another open question, not sufficiently covered by present experiments, is the currently planned Be main chamber wall and its effect on overall SOL chemistry. Beryllium hydride formation and its possible interplay with carbon targets will be addressed by dedicated research projects in the coming years. Initial experiments on PISCES [405] indicate that deposition of beryllium may significantly reduce the erosion of carbon surfaces, alleviating the tritium co-deposition problem but raising an issue of necessary impurity seeding to ensure the required level of power radiation from the edge.

In summary, replacement of the free parameters in the model (plasma transport, boundary conditions, erosion rates, and so on) by more detailed physical models on the basis of improved model validation by the physics community against experimental data remains a priority.

4.3.3. Development of Predictive Codes.

Predictive codes are tools that integrate the existing knowledge of various physical processes in the edge plasma in order to project the physics to the range of plasma parameters of future devices. In contrast to the codes normally used in interpretative mode to analyse experiments in present-day devices, codes used in predictive mode cannot rely on direct input from experimental data and must, therefore, be self-consistent and comprehensive as far as possible. In order to avoid non-physical solutions, they should use only externally controllable quantities as input parameters (see also section 4.3.2).

Of the codes satisfying the requirements above the most developed are the three major two-dimensional divertor codes: B2-Eirene, EDGE2D, and UEDGE [18]. These codes are widely used in both interpretative and predictive mode. They incorporate a multi-species fluid description of the charged plasma components coupled to a Monte-Carlo model for neutral particles. The latter is essential once pumping, fuelling, and detailed plasma-material interactions are to be modelled (see section 4.3.5). Moreover, both modelling results and experimental data indicate the importance of the gas flow between the inner and outer divertor in the private flux region (PFR) to reduce the asymmetry of the operational conditions in the divertors [253, 224]. Therefore, whereas a fluid description of the neutral transport on the same grid as for the plasma would be attractive from the point of view of numerical efficiency, it is not suitable for a predictive code.

As a general requirement, the numerical error (or noise) introduced by a code must be significantly smaller than the effect to be modelled. The transport equations on which the modelling codes are based [18] describe the balance between the fluxes and the sources in the volume and on the surfaces, and an estimate of the required code accuracy can be obtained

from a comparison of different terms. The major terms in the energy equations are the input power, the impurity radiation, the power spent for recycling, and the power delivered to the targets. In normal conditions these terms are comparable, so that evaluation of all these power losses or use of the input power as a boundary condition does not impose any special requirements on code accuracy. The power transferred to the first wall is lower, usually less than 10% of the input power, so that modelling of the interaction of the plasma with the first wall with accuracy better than 10% requires accuracy of the power balance well below one percent. In the momentum transfer, unless the plasma is close to a full detachment, the parallel flow velocities are mainly determined by conservation of total – static plus dynamic – pressure [18], modulated to compensate for the drift flow divergence [124, 523]. In the particle balance, the major terms are the ionisation and recombination sources and the recycling plasma flow to the targets. The source terms related to pumping and fuelling, the only quantities which can be controlled, are, e.g. in ITER, three orders of magnitude lower, and correct modelling of these processes thus requires that the particle balance be accurate to better than 10^{-4}. This is a challenge for a hybrid, fluid plus Monte-Carlo code, and requires modification of the coupling scheme [253].

The description of the physical processes modelled by the major codes has been augmented in recent years particularly by inclusion of the drifts and currents in the edge plasma [33, 126, 124]. This work is in progress, and more effort is needed to validate the models against the experimental data. The initial results yield parallel particle flows with Mach numbers ~ 0.2 to 0.5 in the upper part of the SOL [124, 313, 123] (without drifts, these Mach numbers are an order of magnitude lower). This flow is directed from the outer to inner divertor for the usual B direction (ion B×∇B drift towards the divertor), like in experiment, and roughly compensates the E×B drift in the SOL [525], resulting in a toroidal rotation of the SOL plasma. However, the experiments show factor 2 to 5 higher Mach numbers [111, 313, 526], and the effect of the drifts on divertor asymmetry, especially with reversed magnetic field, still remains to be demonstrated in the modelling [27, 527].

Another important development is the introduction of neutral-neutral collisions in the Monte-Carlo description of the neutral particle transport [259] and making it a routine part of the B2-Eirene code package [515]. This makes the neutral transport model internally consistent for intermediate collisionality range, where the usual linear approximation of molecular flow fails, and improves correspondence between the modelling results and experimental measurements of the gas pressure in the divertor of Alcator C-mod [220] (see also section 4.3.5).

As concerns the numerical aspects of the code development, beyond the incorporation of the drifts and currents [33, 126, 124] and improvement of the particle balance [253] already mentioned above, the introduction of the adaptive grids in B2-Eirene [518] has been an important advance. This method allows better space resolution in the regions of interest at

reasonable total grid size. A thorough comparison of the three major 2D codes (B2-Eirene, EDGE2D, and UEDGE), which employ different discretisation schemes and iterative solution methods [18], is still at early stage [528], so that the advantages or disadvantages of the different approaches remain to be evaluated.

The inclusion of a certain class of effects, such as propagation of fast ions leaving the core plasma in the scrape-off layer (SOL) or interaction of short heat pulses with the targets during ELMs or disruptions, in a major code is impractical because of their weak interaction with the edge plasma or very different time scales. Modelling of these effects requires dedicated codes, three of which have been developed recently:

(a) ASCOT – a kinetic Monte-Carlo code which follows the fast ion orbits from the pedestal region, taking into account the electric fields in the plasma and a broad spectrum of fast ion collisions with the background plasma and neutrals [529]. This code reproduces the experimentally observed sharp peaks of the outer divertor power loads in the H-mode discharges on JET [530, 531, 24], Fig. 4.3.3-1, and shows that the fast ions could be responsible for a significant fraction of the in-out asymmetry in the divertor power on JET. Initial results exhibit a high sensitivity of power load asymmetries to the radial electric field in the SOL, taken as a free parameter in this modelling, and to the ion temperature gradient just inside the separatrix. Since the interaction of the fast ions with the background plasma is rather weak, this code can be used as a post-processor for predictive runs with the major codes, to improve the evaluation of the target loading – especially when the model includes a full treatment of drifts and currents including self-consistent electric fields in the edge [124]. Application of this code to an ITER case modelled with B2-Eirene [26] shows a minor (< 10%) effect of the fast ions on the target loading once a realistic pedestal width is assumed (the plasma profiles just inside the separatrix determine the source of the fast ions in the SOL). However, it should be noted that the attempts to reproduce with ASCOT the distribution of the divertor power loading in the experiments with reversed magnetic field on JET were unsuccessful [19] – probably, because of using the same values of radial electric field as for the standard case.
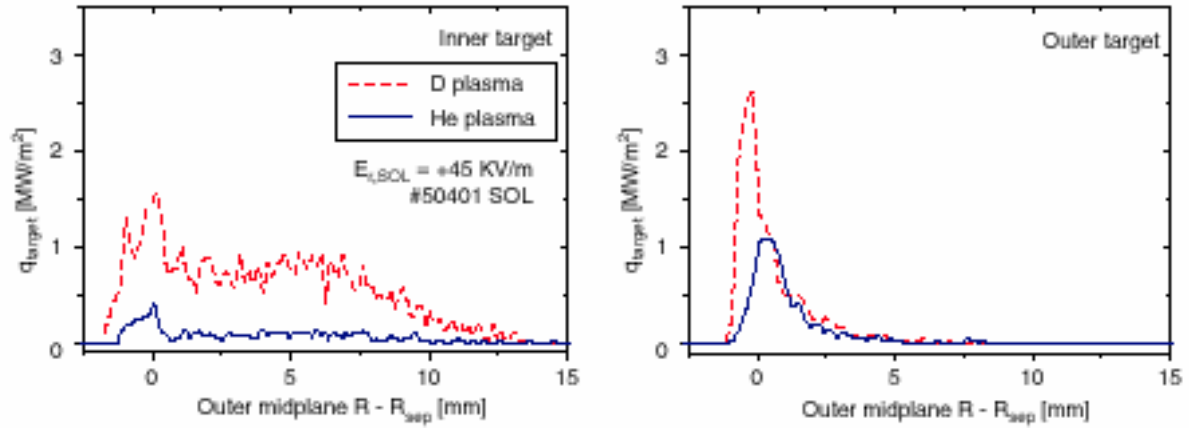
Fig. 4.3.3-1. The power loading profile due to fast ions on the JET targets in D (dashed) and He (solid line) discharges [530].

(b) HEIGHTS [532, 533] and FOREV-2 [534, 157] – two code packages with similar scope, describing the interaction of a strong pulse of heat and particles with the targets, together with the transport of the erosion products and the radiation transport. Whereas the HEIGHTS package looks more developed in terms of detailed description of the target structure, the FOREV-2 code puts more emphasis on a real magnetic geometry of a tokamak. The codes reproduce experimental results on the radiation and heat transport from the MK-200UG plasma gun for pulses corresponding to the disruption loads expected for ITER [534, 533]. For ITER, both codes predict a formation of a dense vapour shield at a disruption, with radiation being the main channel of heat deposition on the divertor structures, whereas the efficient vapour shield does not form during ELMs [535, 536]. Further validation of the codes against the disruption and ELM data from tokamak experiments remains a priority.

In summary, the development of the predictive codes incorporates progress in the theoretical and experimental exploration of edge plasma physics. Recent activities, stimulated by the observation of plasma flows with M ~ 0.5 to 1 (see section 4.2.1.4) along the magnetic field in the SOL and of very narrow peaks of divertor power loading, have resulted in development of the major edge codes to include a comprehensive description of the drifts and currents in the SOL, and in development of a kinetic code which describes the transport of fast ions in the SOL. Current studies of several other effects, such as enhanced cross-field transport due to a long-scale turbulence in the outer SOL (see sections 4.2.1 and 4.3.7), have not yet reached a state which would permit the results to be incorporated directly into the predictive codes. Furthermore, a comprehensive and verified model to predict ELM behaviour is urgently needed, but the underlying physics remains yet to be established.

4.3.4. Radiation transport.

4.3.4.1. Introduction.

In most quantitative assessments of ITER divertor plasmas (see sect. 4.3.2) the radiation field has been regarded as entirely decoupled from the particle fields, i.e., the plasma is assumed to be optically thin. However, various spectroscopic studies have shown clear evidence of opacity (line absorption) effects in the lower Lyman series. In order to quantify these effects for the ITER divertor design, "radiation transport code" development projects have been initiated.

The opacity $\tau = L/\lambda_{mfp}$ (inverse Knudsen-number for photons) scales linearly with n_A $\cdot$L, the product of number density n_A of radiation absorbing particles (in this case, neutral hydrogen atoms), and the average chord length, L, of the absorbing layer. λ_{mfp} is the monochromatic photon mean free path. The photon mean free path at the central wavelength λ_0 of a Doppler broadened line is

$$\lambda_{mfp}(\lambda_0) = (5.4\times10^{-9} \cdot \lambda_0 \cdot f_{nm} \cdot (\mu/T)^{1/2} \cdot n_A)^{-1} \sim 1.3\times10^{13} \cdot T^{1/2} n_A^{-1} f_{1m}^{-1} \text{ [cm]}. \qquad (4.3.4.1)$$

In the right hand expression we have inserted the typical wavelength for Lyman lines, $\lambda_0 \sim 10^{-5}$ cm, and $\mu= 2$, the mass of the emitting particle relative to the proton mass. Here T is the temperature [eV] of the neutral atoms, n_A is their ground state density [cm^{-3}], and f_{nm} is the oscillator strength (f_{1m}=0.4162, 0.079, 0.029, … for the Lyman series). Radiation transfer is probably the best established edge plasma transport mechanism, in terms of accuracy of data: the Einstein-Milne coefficients and Doppler broadening for hydrogen are certainly much better known than any other atomic or molecular cross section. On the other hand, the photon mean free path (defined here for a fixed wavelength) is an extremely steep function of the photon energy, varying by many orders of magnitude within only a few Doppler widths of the line profile. Therefore, the detail of the line profiles is important, with only the near line-centre photons being affected in the divertor. This effect, along with differences in the local conditions of the emitter and absorber, turns modelling of the radiation transport into a rather involved book-keeping issue often requiring Monte Carlo methods for solution.

Eq. (4.3.4.1) shows that plasmas in most of the current divertor tokamaks are optically thin to the Lyman lines since n_A is typically $<< 10^{13}$ cm^{-3}. However, this is *not* the case for very high gas densities (Alcator C-Mod) or for sufficiently large divertors (JET, ITER). The neutral gas temperature and degree of dissociation are also important because only the neutral atomic component can re-absorb this resonance-radiation. Radiation transport effects lead to an enhanced degree of ionisation through "optical pumping", and consequently, reduced neutral-ion friction. Quantifying them is an essential ingredient for understanding and, ultimately, quantitatively predicting the operational window for divertor detachment in ITER.

4.3.4.2. Experimental evidence for opacity.

Solid experimental proof for the resonance line re-absorption is obtained from a modification, with a variation of the neutral density, of line intensity ratios along the same spectrometer line-of-sight, such as between a Lyman line and another line with the same emitting state (e.g. Lyman-β and Balmer-α). Using this method, opacity effects on the resonance Lyman lines have been observed experimentally, in particular for the very dense Alcator C-Mod divertor [257], and in MARFEs [537].

By a similar method, JET divertor plasma conditions have been identified as marginally optically thick for Ly-lines [538, 262], whereas the quoted Alcator C-Mod results show clear evidence of strong line re-absorption, with implied values of n_A as high as 10^{20} m^{-3} [257].

Less direct observations, e.g. from line-shape analysis or from experimental determination of populations of highly excited states of atoms and their deviation from collisional radiative modelling have also been reported, see [539] for a summary and further references.

4.3.4.3. Theoretical predictions.

Opacity effects have been discussed for a long time as possible contributors to overall divertor dynamics in high density regimes. See [540] for one such early example (INTOR phase), although note that the neutral densities used in the calculations were two orders of magnitude larger than are observed in present experiments. Computational assessments have typically been based upon highly idealized, often zero-dimensional approximations (so called "optical escape factors" in collisional radiative models) [541] or one-dimensional (slab) approximations [542]. Detailed photon transport procedures are well established in many fields of science, e.g. in astrophysics, and for high pressure discharges used for lighting purposes. Considerable effort is required to adapt these specialized codes to typical fusion edge plasma conditions, especially configuration details. Some steps have already been undertaken, e.g., with the CRETIN code [537, 543, 544, 545] and with the EIRENE Monte Carlo Code [223, 539, 524, 546], which is already in use and well adapted for ITER design studies as a neutral particle module within the B2-EIRENE code package (see section 4.3.2).

In the CRETIN code, rather simple geometry (slab) and plasma models are typically used, and emphasis is on self-consistency between the radiation field, the non-LTE gas conditions, and the (1D) plasma. All relevant line broadening mechanisms are included. In particular, Zeeman splitting in a strong B-field is fully implemented, along with the Stark effect. Significant changes in the steady state plasma solution are reported when the Lyman line re-absorption is taken into account, as compared to the conventional optical thin assumption from present edge modelling [547].

In the EIRENE code, the advantage is exploited that the radiation transfer equation is mathematically analogous to the linear Boltzmann equation for neutral particles solved by EIRENE. As a result, a major part of the existing code can be used directly for photon transport problems, with only minor modifications. EIRENE has been run on a set of converged B2-EIRENE simulated ITER divertor plasma conditions, with and without line absorption effects taken into account. Although a self-consistent feedback of the changes in the neutral divertor pressure caused by radiation trapping has not been studied up to now, the neutral gas pressure and neutral-ion friction in the divertor are always found to be reduced significantly (factors between 2 and 5) [539] as compared to the assumption of optical thinness. The dominant line broadening mechanism in these studies is Doppler broadening, with the linear Stark effect and natural line broadening playing only a minor role [524]. However, the opacity effects may have been overestimated here because Zeeman line splitting is not yet implemented, and they might be further reduced in mixed D-T cases where the Doppler line profiles would no longer overlap significantly at the 1-2 eV gas temperature observed in these simulations. Benchmarking and validation of the radiation transfer module in EIRENE (excluding non-LTE effects and Zeeman splitting) has recently been accomplished by application of a coupled photon-plasma code FIDAP-EIRENE to high intensity discharge plasma lamps (which operate at pressures of 20-50 bar and are clearly in LTE) in a joint effort with the lighting industry. Assessment of the code developments through comparison with measurements from fusion experiments, particularly JET and Alcator C-Mod, is underway. It, therefore, seems realistic to assume that within the next few years ad hoc opacity assumptions can be eliminated from current divertor codes.

4.3.5. Neutral Particle Transport.

4.3.5.1. Introduction.

The mutual interaction of neutral gas dynamics and the plasma flow provides access to favourable plasma conditions in divertors, such as the high recycling and the detached plasma regimes. This is similar to other areas of (computational) fluid dynamics, where there is also often a tightly coupled fluid/solid interface. In edge plasmas, this interaction not only sets the boundary conditions but dominates the exchange of matter, at least for the divertor operating conditions currently envisaged for ITER.

Whereas the basic physical process for the edge plasma, the Coulomb interaction, is simple, the formulation and numerical solution of tractable plasma fluid equations – the ordering of terms, and the identification of a set of consistent boundary conditions – is still a very active and rapidly evolving field of edge plasma research. The situation is reversed in the case of neutral gas transport, which provides this mechanism for exchange of matter, momentum and energy between the solid, gas and plasma states. This transport mechanism is

ruled by the well known, and often even linear, Boltzmann equation. Corresponding linear transport theories and their diffusion approximations are well developed. Rather complex reaction mechanisms, governed by specified cross sections, are often involved; sometimes rich chemistry, e.g., hydrocarbons, must be invoked. In particular the Monte Carlo method of solution is routinely applied for ITER design studies with the EIRENE neutral transport code [546, 548] (see Sect. 4.3.2). Such "recycling models" can properly account for arbitrary geometrical and physical complexity.

In principle, the factors limiting the predictive quality for a given host medium (plasma) are the remaining uncertainties in some atomic, molecular and plasma surface interaction data (see below). In practice, however, it is often quite difficult to anticipate the necessary level of sophistication required (at the expense of CPU-performance, usually) in any particular study. This makes the necessary pre-selection of tolerable model approximations a rather critical step in predictive neutral gas transport modelling studies. It probably will always have to be carried out on a case by case basis.

4.3.5.2. Transition to low temperature hydrogen plasma physics.

With the transition of envisaged ITER divertor plasma states from the high recycling, ionizing phase (until the early nineties) towards a (partially) recombining detached plasma solution, a large number of new atomic and molecular processes become important, which have been safely ignorable under fully ionizing plasma conditions.

Molecular hydrogen (and molecular hydrogen ions), in particular vibrational kinetics, and resulting resonant charge exchange between unlike particles (protons and vibrationally excited hydrogen molecules), start to play a dominating role in the degree of dissociation and the ionization-recombination balance in the divertor (see also Sect. 4.2.3.3, on Molecular Assisted Recombination "MAR").

The first Fulcher band divertor spectroscopy (i.e., on the molecular counterpart of atomic Balmer-α emission), carried out in the ASDEX-Upgrade divertor [549] had initially led to mismatches between experimentally deduced and B2-EIRENE simulated molecular densities (a factor of up 20), first attributed to a possible role of MAR at that time [549].

Later, this discrepancy diminished after replacing the initial corona assumptions in the experimental Fulcher band data interpretation by the full collisional radiative model for the p-H-H_2-H_2^+ system [550, 259] used in the EIRENE molecule transport model. Apparently, not only the atomic hydrogen (long known regarding high recycling divertors), but in detached states, also the molecular component requires detailed non-corona and non-LTE treatment. Corresponding models have been set up [550, 551] and included in the codes [259, 552], and are further being refined currently.

As discussed in 4.2.3.3 for the case of MAR, vibrational kinetics and hydrogen chemistry is a well established mechanism in low temperature gas discharge plasmas, in

which the neutral gas density is set as an external control parameter. In divertors, its role is far less clear because the molecular pressure is set at a value self-sustained by the recycling at the targets. As a result, for example, in B2-EIRENE simulations of an ASDEX-Upgrade detached divertor scenario, the inclusion of the additional vibrational kinetics (required as precursor for MAR) had led to a strong reduction in the self sustained neutral pressure, an overall reduction in the volume recombination rate (rather than the enhancement initially predicted from idealized, separated and strongly simplified arguments, see [18]) and even a subsequent re-attachment (into a high recycling divertor state) under otherwise identical edge model parameters and upstream boundary conditions [267].

This modelling result was consistent with the above mentioned detailed Fulcher band divertor spectroscopy at ASDEX-Upgrade, and indicates that in the current recycling models without the molecular kinetics, the volume recombination rate and upstream parameter window may not be underestimated, but instead over-estimated. The original choice in ITER divertor modelling to neglect them altogether seemed, therefore, justified. Indeed, first results of ITER modelling with the molecular kinetics taken into account show no significant effect of MAR [515]. Further quantitative assessments are currently being carried out.

Observations (B2-EIRENE model vs. experiment) confirming this picture of "enhanced dissociation" rather than "enhanced recombination" due to vibrational kinetics have been reported from TCV [553, 554]. The initial application of the B2-EIRENE code to the experimentally observed transition to detached states showed that the volumetric recombination rate used in the code model had to be increased artificially by a factor 5 over the (quite well established) true atomic rates used in EIRENE for recombination. Vibrational kinetics in H_2 transport, and hence "MAR", had not been included in these first simulations. However, after activating the vibrational kinetics, the same trend appeared as in the ASDEX-Upgrade study, where detachment was even harder to achieve with MAR than without.

Therefore, other mechanisms must be active in TCV divertor detachment, which have yet to be explicitly identified. Rather complex hydrocarbon chemistry could play such a role [555], and is, amongst other possible contributors ("blobby transport"), currently being investigated by code simulations and further experiments.

As a result of the clear signatures of complex hydrogen (and hydrocarbon) chemistry, significant efforts have been undertaken to upgrade the corresponding atomic and molecular databases used for plasma edge modelling. Most recent compilations of hydrocarbon data are available in [436] (methane family and their ions) and [329] (ethane and propane families and their ions). The current hydrogen chemistry data status (p-H-H^- -H_2-H_2^+-H_3^+) has been compiled and critically assessed in [556].

4.3.5.3. Sensitivity to configurational and physical details.

The baffling of the neutral gas in some places, either by the action of the plasma flow or by divertor hardware, and the resulting gas conductance between different places in the divertor (e.g. inner to outer leg) are essential design criteria for particle removal, helium pumping, etc. Present self-consistent plasma-neutral gas models seem to work quite reliably for those aspects of the divertor dynamics which are dominated by the direct plasma surface contact and recycling from near divertor strike points and the outer SOL. If the private flux plasma is involved in a controlling way, agreement between experiment and plasma-neutral gas simulation is much harder to achieve. Configurational details, low temperature hydrogen plasma chemistry, the onset of neutral gas viscous effects and uncertainties in experimental identification of the weak private flux plasma all seem to matter simultaneously. For example, for the Alcator C-Mod divertor only by a lengthy step-by-step model upgrade could an initial mismatch of experimental and modelled pumping plenum pressure of a factor 10 be reduced to a (still) remaining factor 2 [557, 220], see Figure 4.3.5-1, where the toroidal non-uniformity of the neutral pressure is illustrated, depending on whether the nearest port is open or closed. Note that ignoring the (known) effects of 3D divertor leakage pathways and resonance radiation trapping gave excellent agreement between model and experiment, apparently by coincidence. However, this only demonstrates that matching experiments with simplified models can be strongly misleading.
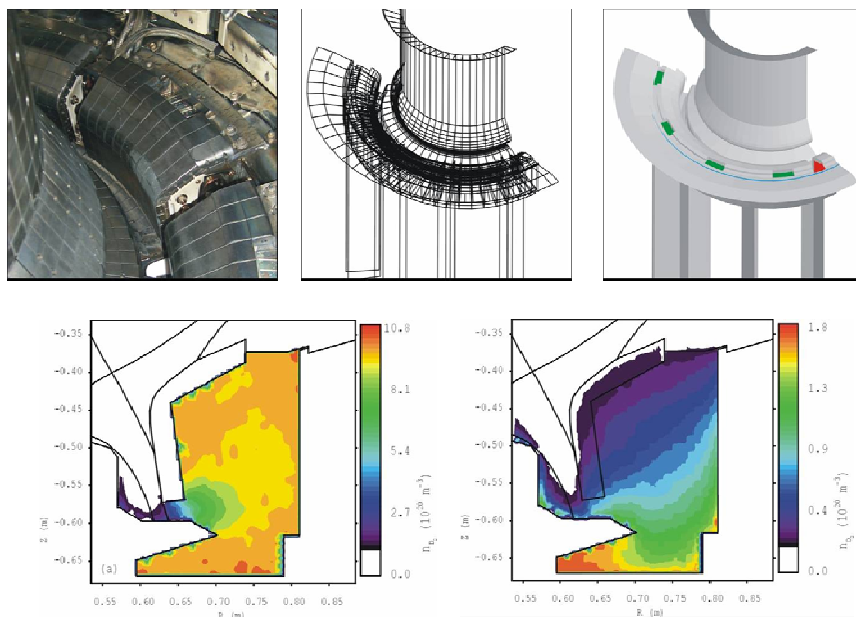

Figure 4.3.5-1. 3D neutral gas modelling for Alcator C-Mod [557 and 220]: toroidal gap and gussets, bypass and poloidal gap are included in order to calculate toroidal variations in the divertor neutral pressure. Refinement of 3D structure, SOL and PFR plasma solution, atomic and molecular processes, viscous and radiation trapping effects have led to improved agreement with the measured divertor pressure (factor of 10 initially, now about a factor of 2). Below left: gas pressure at location of open port, below right: gas pressure at location of closed port, different colour scale.

A confirmation of the sensitivity to private flux region physics, stressing the need for further neutral gas model refinements was also provided by a predictive modelling "design" study (again: with B2-EIRENE) on the ASDEX-Upgrade divertor modifications. Strong effects on in-out asymmetry in neutral flux densities had been predicted for the private flux region [246], but no such trends could later be found experimentally after completing the hardware upgrades [152]. Current coordinated research projects on low temperature hydrogen plasma chemistry and on transport are also being initiated to improve the predictive quality of numerical divertor models in this essential aspect.

4.3.5.4. Concluding Outlook.

Many or perhaps even most of the relevant processes between neutral particles in the edge plasma in present machines and in ITER, which are relevant for the overall divertor plasma dynamics, are known, even quantitatively, and could, in principle, be included in the modelling codes in great detail. There have been, and still are, continuing coordinated efforts to improve the atomic and molecular databases and surface interaction models used in neutral gas modelling. Subsets of these databases have been or are currently being implemented in neutral particle codes (and impurity codes). A sufficiently detailed set of atomic and surface physics can and will most probably be implemented first in the rather laborious but physically transparent Monte Carlo codes currently used for ITER divertor design studies.

However, an 'a priori' selection of the relevant processes to be included for a particular predictive study, in order to devise a sufficiently detailed but still "simple as possible" model, remains a critical task. Amongst these issues, which may matter in some cases but not in all, are: proper timescale separation in collisional radiative approximations, details of the particle-surface interaction, surface accommodation factors for momentum and energy, 2D vs. 3D geometry for pumping efficiency and divertor leakage studies, main chamber recycling, recycling at parallel targets (baffles), the onset of viscous effects in the gas, radiation trapping (see Sect. 4.3.4), etc. These issues continue to require major edge physics studies (also related to the recycling and self-sustained neutral gas build-up) in many tokamaks, covering a wide range of densities, temperatures and configurational aspects.

4.3.6. Impurity Modelling.

Modelling of impurity sources and transport in the edge has always been an important component in edge research and this effort has continued across a broad front since the 1999 ITER report. In the short space available no attempt is made at full coverage of this substantial ongoing activity; but only some new developments since 1999 – and which are directly pertinent to ITER – are briefly outlined. Impurity transport is modelled in order to understand its effect on tokamak operation and tritium inventory control. The impurity level in the core and SOL affects radiation and fuel dilution. Co-deposition of impurities with

tritium on first-wall surfaces can lead to unacceptably high levels of T retained in the vessel. The latter area has been the major emphasis since the IPB.

The experience of the JET 1997 DTE campaign shows how important C/T co-deposition can be [271] (see also section 4.2.6.3). The co-deposits formed a remarkable pattern: the great majority occurred on water-cooled louvers in the pumping recess facing the inner divertor target – thus out of direct plasma contact. Since such an effect potentially provides useful opportunities for recovering the T, it is important to understand how the C and T arrive there and stick. Without adequate understanding, extrapolation to ITER is uncertain.

The modelling of carbon behaviour in tokamaks continues, generally, to be one of the most pursued – and hard to explain - areas in edge physics [320, 558, 559, 560, 561]. Modelling of the JET co-deposition process [271, 272, 440] increases the challenge because of the wide range of edge processes playing a role. Three main steps are evidently involved: (a) the primary source of the carbon in the co-deposits appears to be the main chamber walls, (b) this carbon is then transported as ions along the main SOL, and across the private flux zone, to the inner divertor where it may initially deposit on the inner target, (c) it may then be removed by some process and transported as neutrals to remote, cool regions, out of plasma contact, e.g. the JET louvers. Each of these main steps is characterized by major questions. Is the source due to carbon eroded by charge-exchange neutrals or by plasma contact? Does the sputtering occur mainly during 'normal' plasma conditions, i.e. the flat-tops of standard discharges, or during transients such as ramp-up, ramp-down, ELMs, disruptions? Is the wall, more or less uniformly, the source or the leading edges of specific edge structures? Although there is now evidence for the existence of flows that could carry the C to the inner divertor, the basic cause has not been clearly identified. It is probably due to some combination of drifts [126] and closing of particle 'loops' driven by radial transport [114]. Finally the process by which neutral carbon is transported from on/near the inner target to the louvers is not understood.

Because of these major uncertainties the modelling to date has often been characterized by a substantial ad hoc, prescriptive component. The modelling effort has been mainly on the carbon impurity itself, taking the 'plasma background' as specified. For example, onion-skin modelling (OSM) with a heavy prescriptive aspect for the background plasma was used to approximately match the measured divertor spectroscopic signals for what was taken to be a representative JET shot [562]; in addition, more rigorous modelling, B2-EIRENE/SOLPS and EDGE2D [563], has also been used. The inner divertor is the most important but also most problematical plasma region to describe owing to the fact that it is typically detached and because of the paucity of reliable diagnostic data (i.e. 2-D fields of n_e, T_e, T_i and $v_{\parallel}$). Of course, this modelling of the background plasma is predicated on the questionable assumption that a 'standard', as opposed to an 'off-normal', plasma condition is appropriate and has been identified. With regard to the impurity modelling itself: the magnitude of the louver deposits

shows that the C-throughput rate can be estimated to be ~4-6% of the total D^+-flux to the inner target integrated over the DTE1 campaign [271]. Accordingly, in the modelling, a wall source of carbon release was simply prescribed to give this magnitude without attempting to actually model the release mechanism. In order to convey the C-ions efficiently to the inner divertor in the OSM modelling, a strong parallel flow was imposed as part of the 'plasma background', and adjusted – as to speed and spatial extent - until essentially all the C-ions reached the inner divertor, in accordance with the measured deposition pattern. It turned out, however, that the substantial flow speed required to achieve this, Mach numbers ~0.5, was in accord with subsequent measurements by Langmuir Mach probes. $^{13}CH_4$ injected at the top of the JET SOL resulted in ^{13}C deposits in the inner divertor [309], also confirmatory of this picture. It is nevertheless the case that the first 2 parts of the impurity "modelling" – source and large-scale ion-transport – are, to date, essentially prescriptive and thus not adequate for predicting future performance (ITER or otherwise).

To date the most ambitious part of the modelling effort has been on the 3rd step, the neutral transport to the louvers. For this analysis work, sophisticated impurity Monte Carlo codes have been employed, REDEP [272] and ERO-JET [440], whose field of focus is restricted to the inner divertor and louver region. These codes have taken as input the prescribed 'plasma background' and C^+-inflow into the inner divertor, as described above. In the cold plasma conditions of the detached inner divertor, chemical sputtering processes have been assumed to dominate. These codes follow in considerable detail the chemical sputtering processes releasing methane and heavier hydrocarbons from the inner target, employing the most recent compilations of rate coefficients for the break-up kinetics [564, 565, 566]; the transport and break-up of the hydrocarbons, both charged and neutral fragments; the reflection/sticking of the fragments which strike solid surfaces, based on new molecular dynamics code simulations [567, 437, 568]; all within the detailed spatial structure of the JET inner divertor and louver region. Figure 4.3.6-1 shows some sample results of this analysis [440].

Despite the large amount of empirical input, the REDEP/ERO-JET modelling using standard assumptions has not been able to explain the large magnitude of the co-deposits found on the louvers: calculated tritium co-deposition rates for the JET MkIIA divertor, using 'reference' chemical erosion yields of order 1% - while higher than previously estimated - are well short (by ~1/40X) of published data [272]. Because all of the basic processes involved have their own significant uncertainties, sensitivity tests were performed to see what changes from the various 'reference' assumptions would be required to bring the modelling and the measurements into agreement. It was found that a reasonable agreement between the simulation and the experimental observation of the carbon deposition at the inner louvers in the MkIIA JET divertor is achieved, if high chemical yields of about 20% together with a negligible effective sticking of hydrocarbons are assumed. Although there are experimental

observations indicating such high erosion yield, such yields cannot be applied as a stationary value for the effective erosion since it would turn the inner divertor into a net erosion area in contrast to the experimental findings, [440]. Indeed, the chemical erosion yield of the carbon depositing on the inner target may be much higher than for the base graphite [320].

With regard to tritium-carbon co-deposition, it is evident that we are presently far from a predictive capability for ITER: the uncertainties about the physical processes involved and the experimental database are still too large for reliable predictions of these processes for future devices, [272]. The principal limitation to progress in this type of modelling appears to be a lack of detailed measurements of all the relevant processes in the divertor region, rather than the modelling tools directly. For example, establishing the original source of the carbon in the co-deposits, spatially and temporally, is essentially an experimental issue, requiring much more extensive diagnostic capability. Interpretation of deposition processes that occurred over an entire campaign is difficult; it may be, for example, that the louver co-deposits were formed during the cleanup procedure when the strike point was intentionally swept along the divertor surfaces to heat them; time-resolved deposition studies, now in progress, will be invaluable.
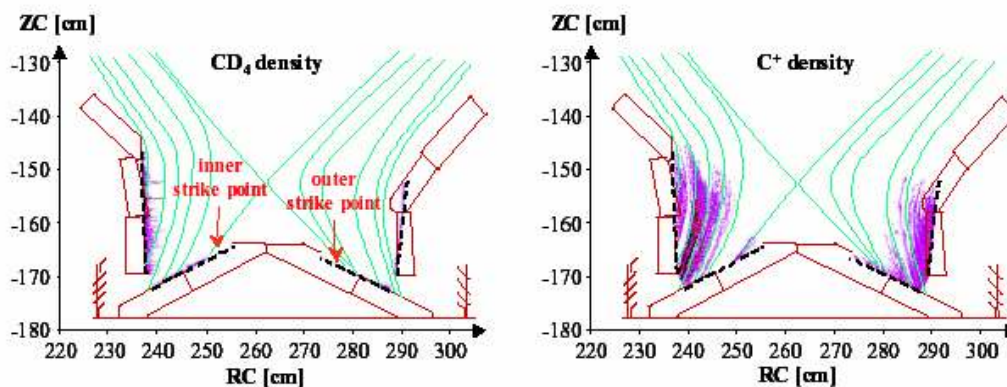

Fig.4.3.6-1. Simulated CD$_4$ (left) and C$^+$ (right) particle density after chemical erosion of CD$_4$ in the divertor of JET MkIIa under the assumption of fully-sticking hydrocarbons [440].

The ITER design calls for an extensive use of W at the divertor region (initially only at the baffles) and, thus, modelling studies of W transport are being actively pursued. An example of modelling of W on wall surfaces in current tokamaks is that of ASDEX-Upgrade [291]. In the first phase of W installation in ASDEX Upgrade, only the lower portion of the heat shield was W-coated, seeFig.4.3.6-2. After a one-year campaign the erosion of the W-coated carbon tiles as well as the migration of W onto the uncoated tiles in the divertor were measured using ion beam surface analysis. Modelling of the W sputtering and edge transport has been carried out using the impurity Monte Carlo code DIVIMP, extended to allow for simultaneous plasma contact with the two divertor targets and the heat-shield wall [291]. The 'plasma background' required as input for DIVIMP was taken from the B2/EIRENE analysis for a well diagnosed discharge – albeit one which might not be representative of the average plasma exposure conditions. A constant W-flux density from the wall was assumed. It was

found that the calculated W-deposition profile shape was in reasonable agreement with that measured.

Modelling the physical sputtering of high-Z elements such as W is particularly challenging since the principal mechanism is the impact of light impurity ions [402, 569], such as C and Be, which will be present for the current ITER design (the sputtering threshold for D/T-ion impact is so high that this source can be neglected). It is therefore necessary to first model the light ion impurity behaviour, and in considerable detail. It is necessary to know: (a) the mix of charge states entering the sheath (since the different charges experience different sheath accelerations); (b) the individual temperatures of the different charge states at the entrance to the sheath; (c) the individual average parallel speeds of the different charge states at the sheath-entrance; each of these factors can have a large influence on the impact energy, and thus the sputtering yield. A further complication of such mixed-element situations is that the fractional coverage of each different portion of solid surface needs to be known, something that has to be computed self-consistently within the impurity modelling itself [570]. Our present capability to predict ITER impurity behaviour for high-Z impurities is therefore even more challenging than for carbon, since the low-Z impurity has to be modelled as well.
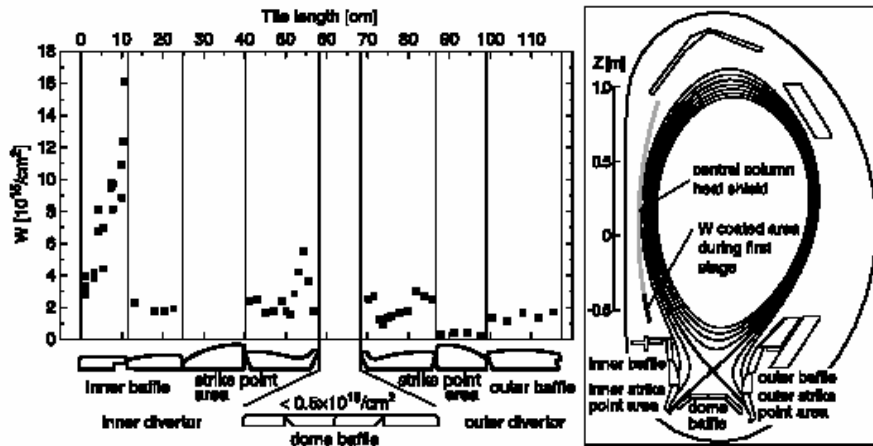

Fig.4.3.6-2. Measurements of deposited W in the divertor of ASDEX Upgrade after the first stage with W tiles only at the lowest heat shield tiles. One can see a strong deposition at the inner baffle and the inner strike point position. There is also some W deposited at the outer divertor [291].

For helium impurity transport, the importance of elastic collisions of He atoms with background ions of hydrogen isotopes has been shown experimentally [252]. Fast thermalisation of He atoms in the JT-60U divertor found from spectroscopic data is well reproduced in modelling when the He elastic collisions are taken into account. These collisions have a beneficial effect on the expected helium removal efficiency of the ITER divertor [253] (see also section 4.3.2).

In contrast to the above-described work on modelling impurity sources and their transport in the SOL there has been less effort dedicated to modelling impurity transport into the core.

This is possibly because the radial transport is critically dependent on the parallel transport in the SOL which, as discussed above, is in itself already problematic. An example of modelling core impurity levels is based on JET screening experiments, see [571] which reference also provides an extensive set of references for methane injection experiments including studies on core carbon transport, plume characterization, erosion and re-deposition, molecular break-up studies, and evaluation of carbon penetration through the SOL to the core. The JET work was fairly successful in reproducing the scaling of C impurity levels with core density and input power. This type of modelling was also applied to Alcator C-Mod with limited success in reproducing experimental results showing poloidal variations in impurity screening.

Impurity behaviour is one of the most challenging aspects of edge physics to understand and model since it is first necessary to sort out, in some detail, many or most aspects of the 'plasma background', i.e. the fuel plasma, including such complex phenomena as ELMs and when/where erosion & re-deposition occur (e.g. transients vs. steady-state portions of the discharge). Advances in understanding should benefit from the acquisition of more detailed experimental data describing the plasma characteristics as well as that of the impurities. On such a basis, one has the chance of developing sound understanding with the ultimate objective of achieving reliable predictive capability. One technique used for interpreting such detailed data involves so-called 'simple-as-possible plasma' experiments [572].

4.3.7. Simulation of cross-field transport of the tokamak Scrape-Off Layer.

4.3.7.1. Intermittent transport in the SOL.

Cross-field transport is a key physics issue in all critical problems of the SOL and divertor plasmas. This physics still remains an open question although significant knowledge, both experimental and theoretical, has been built along the years. In the modelling effort that is crucial for ITER, the cross-field transport is taken into account by an ad-hoc diffusion coefficient [573]. Indeed, it was considered that this cross-field transport could be addressed as due to a random process. In the limit of a very large number of events this approach would lead to a diffusive process in the frame of mean field theory. Tied to this point of view is the idea that the correlation length, that characterises the steps of the random process, is small, in particular much smaller than the SOL width. This point of view is to date the only available description that can be used in the extensive modelling effort required for ITER. However, this description cannot account for the growing experimental evidence that transport in the SOL exhibits intermittent events that are not properly accounted for by a diffusive process. An outstanding experimental aspect is that fluctuations, typically density fluctuations, are large and comparable to the mean density [574]. This fact directly contradicts the theoretical basis that leads to the description of transport in terms of a diffusive process.

Numerous issues in the ITER design involve cross-field transport, the most important being the width of the energy channel onto the divertor target plates and the long range particle transport that might govern recycling in the main chamber. These two effects are characterised by two scales in the transverse direction to magnetic surfaces, namely λ_q the energy channel width and λ_n, the density e-folding length. Although there is significant experimental evidence that both energy and particle transport are governed by electrostatic turbulence, let us introduce the key physics with a rough estimate of these two SOL widths, either governed by collisional transport for energy transport or by electrostatic diffusion for particle transport. The definition of the SOL width, namely the volume of open field lines where plasma "wets" wall components, introduces several difficulties. Indeed, the SOL appears as a region governed by a balance of two transport processes, parallel transport to wall components and cross-field transport. It is assumed that parallel transport is classical, hence described in terms of free streaming particles and collisions. The parallel collisional mean free path L_{coll} is then the characteristic transport scale. Furthermore, it is assumed that the particle life time is governed by the parallel transport to the plasma sink at the wall, this leads to another characteristic scale, the connection length $L_{//}$. For the energy transport, we consider collisional diffusion in both the parallel and transverse directions. One then readily obtains $\lambda_q = \rho_e (L_{//} / L_{coll})$ where the ratio $L_{//} / L_{coll}$ is the number of collisions during a life time of a particle in the SOL and where the electron Larmor radius ρ_e is the characteristic step in the transverse direction. For typical SOL parameters, one finds that this estimate of λ_q is orders of magnitude smaller than the experimental observations. In the case of electrostatic turbulence, we assume that the electric potential eddies have the same characteristic scale in both transverse directions to the magnetic field. The density e-folding length is then found to be a balance between a Bohm-like diffusion and the parallel life time of particles, $\lambda_n = g_B (L_{//} / \rho_s)^{1/2}$. The key parameter here is g_B, the ratio between the magnitude of the electric potential fluctuations and T_e / e, the electron temperature T_e divided by the charge e. We have used here the hybrid ion Larmor radius $\rho_s = c_s / \Omega_i$, where $c_s = (T_e / m_i)^{1/2}$ is the parallel sound velocity and $\Omega_i = e B / m_i$ the ion cyclotron frequency, m_i being the ion mass. For large values of g_B, $g_B > 0.1$, this estimate of the SOL width is of the order of magnitude reported experimentally. Concerning parallel transport, three aspects are highlighted by the analysis. First there is a strong geometrical dependence that is characterised by the connection length, second, the large parallel transport will organise transport in such a way that there is little variation along the field lines, leading to the so-called flute effect, third, the collisional mean free path is comparable to the connection length so that kinetic features should be accounted for. Furthermore, the parallel electron transport will play a strong role in the electric potential fluctuations either via the parallel resistivity or via plasma boundary effects at the wall. Finally, in the case of electrostatic turbulence, energy transport will be governed by the same transverse Bohm-like diffusion but with a shorter parallel life time for electrons.

The electrons heat channel is then expected to be $(m_i / m_e)^{1/4}$ narrower than the density and ion energy channel. The goal of electrostatic turbulence simulations is to determine the geometry and magnitude of the electric potential fluctuations given the various instability mechanisms that can play a role.

Let us now consider the conceptual difficulty introduced by the fluctuation level of order 1. This signature of SOL cross-field transport questions the understanding in terms of local equilibrium and in particular of detailed balance in the master equation governing transport between the magnetic surfaces. As a consequence, there is no general theoretical basis for a diffusive process and for scale separation between the transport events and the system size. The very meaning of profiles could also be questioned. This first principle description of a complex cross-field transport is also backed by recent experimental evidence of long range transport in the SOL [58, 128, 77, 82], and intermittent transport events in the SOL [89, 575, 93, 576, 49, 87, 86].

The power loading on the divertor tiles, and, via this technological constraint, the operation point of high power devices is usually characterised by the parallel heat flux e-folding length λ_q. Given our previous conclusions, one readily understands why there is to date no consolidated empirical or theoretical approach to scale the present experimental results to ITER [577]. The question is then to determine the level of confidence one has in the modelling effort of the ITER plasma-wall interaction.

4.3.7.2. Present modelling effort of cross-field turbulence.

We shall concentrate now on the various theoretical analysis of the SOL turbulence. Three instability mechanisms are considered for the SOL turbulence: interchange modes coupled to either the sheath resistivity [578, 579] or to the plasma resistivity for the resistive ballooning mode [580, 581], and the negative sheath resistivity mode due to plasma temperature fluctuations at the sheath [582]. In most of these models, the electron dynamics is embedded in the vorticity equation derived from the quasi-neutrality constraint so that the electron energy can be regarded as a passive scalar. However, in the negative sheath resistivity model, the electron temperature fluctuations are essential. The curvature effects that drive the interchange mode tend to "balloon" the transport on the low field side with little turbulent transport on the high field side. This agrees with several experimental observations [89]. As a consequence, mechanisms based on the interchange are the prevailing instabilities that are used in the simulations. Drift waves that are claimed to govern the edge plasma transport can also be considered [583]. Let us review the main theoretical investigations of SOL turbulence and their implication for the ITER modelling :

(i) A phenomenological description of interchange-based cross-field transport [195] has become a major reference in the experimental analysis of edge turbulence. It characterises analytically the properties of coherent density structures that would propagate ballistically in

the SOL. These density structures are termed "blobs". The basic mechanism driving the ballistic motion is in fact the standard interchange mode, namely the electric drift velocity induced by the charge separation itself governed by the curvature drift. The finite poloidal extent of the density structure, and, therefore, the existence of a poloidal density gradient is a key element of such radial "blob" transport. A flute approach, namely that all fields are constant along the magnetic field line, is used to reduce the dynamics to a 2D (r, θ) plane [196]. This work provides scalings and predictions for these specific events. These results have been incorporated in a 2D modelling of the plasma-wall interaction. Transport is then modelled in terms of two processes, diffusion due to the turbulence and, superimposed, a radial outward convective flux [584]. Although such a description captures the essence of ballistic flights in the SOL, its thermodynamical foundation is more difficult to assess since transport can take place when the system is at rest (no dependence on a gradient).

(ii) Another approach is a turbulence simulation of the edge plasma in the BOUT code. A flux tube geometry is used with a comprehensive set of fluid equations and the appropriate geometry, in particular the X-point effects [585]. The simulation domain contains both the region of open field lines, the SOL, and closed field lines just within the separatrix. This significant effort of edge simulation is well adapted to analyse experimental results from various devices. Several important topics are presently investigated. For instance, in the DIII-D geometry, a pedestal formation is reported due to the neutral influx, even for L-mode parameters [586]. For the same DIII-D geometry, the existence of sheared poloidal flows is analysed numerically and compared to the available experimental data [587]. A similar effort is carried out for C-mod where a particular mode structure is documented [588]. An original effort has been initiated that couples this turbulence code to the 2D edge simulation tool UEDGE, in order to investigate phenomena that develop on long time scales such as the change in radiation pattern [589] prior to the density limit [590]. This effort remains extremely focussed on the modelling of the DIII-D and C-mod devices. Relevance of the results to other devices, and therefore to ITER, remains an open question.

(iii) A comprehensive investigation of SOL turbulence in what is called a "flux-driven" regime has been achieved [591]. In this approach, a particle flux is imposed rather than a mean density gradient. As a consequence, the confinement properties of the system evolve freely in response to the external drive and the turbulent transport [592]. In such a regime, the turbulent particle flux is found to be strongly intermittent. Density fronts propagate ballistically [591, 593, 594, 595] and a large fraction of the total particle flux is transported by rare and large transport events [596]. In these simulations, no scale separation is found between the smallest density gradient scale, typically $\sim \rho_s$, the mean density gradient $\sim 55 \, \rho_s$ and the long range ballistic propagation of a given density front $\sim 200 \, \rho_s$. The generation of zonal flows [597] can be viewed as the result of an inverse cascade, namely the transfer of energy from the large wave vector to the small wave vectors. These flows are large

scale flows in the poloidal direction that can exhibit fine radial and temporal structures [598, 599]. They are generated by the turbulence and are also regulators of the turbulence [600]. The interplay between the zonal flows and the density fronts is a key element in determining the actual transport regime in the non-linear phase [601].

The scaling of the mean density e-folding length in terms of the connection length has been analysed with extensive simulations that provide an accurate scaling of the SOL width in terms of the connection length with a power 0.62 [602]. This scaling is calculated analytically and one finds that the ballistic scaling (power 1), that actually governs density transport [603], is in fact partly cancelled by the reduced frequency of the intermittent events as the connection length increases so that the scaling is rather close to the diffusive scaling [602]. Including the scaling of the curvature effect, one finds that the dependence on the major radius is still weaker so that the SOL width is nearly independent of machine size [604]. No strong conflict thus appears between the extrapolation of present experimental results performed in the ITER modelling and the average SOL width scaling obtained in the turbulent simulations. Stronger departure from the diffusive modelling and the turbulent transport will be found for transient effects where ballistic transport will govern the time scales.

4.3.7.3. Summary of the outstanding trends.

Theoretical and simulation results indicate that long range transport events, namely that exceed significantly the SOL width, must be expected. These transport phenomena depart significantly from the standard point of view of a diffusive cross-field transport ruling the plasma-wall interaction. Recent simulations of the scaling of such intermittent transport indicate that the scaling of the SOL width on the plasma major radius is significantly weaker than one would expect from a ballistic scaling. In fact, it is found to be similar or even weaker than expected for a diffusive scaling. These results thus indicate that the ITER modelling of the plasma-wall interaction based on diffusive transport capture a reasonable description of the transport features in the steady state regime. However, transient effects cannot be appropriately modelled with diffusive transport. In particular, material born at the wall can exhibit a rapid influx in conjunction with an inward ballistic event. The lack of scale separation indicates that turbulent transport is coupled to macro-scales such as MHD modes. In particular, the coupling of turbulent transport to ELM transport must be considered [191].

Present turbulent simulations of the SOL do not provide an extensive study of the scaling of the SOL width. Several key issues are still to be addressed. In particular, the geometry of the system is characterised by several interface problems, jumps in the connection length with secondary limiters and, more important, the interface between the edge plasma located on the closed magnetic surfaces and the SOL. Large changes in the turbulent transport have been reported between the edge plasma and the SOL plasma [595], in particular structures in the SOL are observed to be more flute like [583]. However, few

simulations allow one to address both the edge and SOL plasmas. In this case, turbulence spreading will enhance transport in the most stable region and reduce turbulent transport in the most unstable region. This effect can strongly modify the present analysis. Another issue is the impact of the large scale flows, both in the radial direction whenever the turbulence eddy size is that of the SOL [605], and in the poloidal and toroidal direction where large scale flows are observed [598, 606].

A proper modelling of SOL turbulence is important not only to model plasma-wall interaction using present experimental data scaled up to ITER but also to model ITER operation where SOL cross-field transport will strongly influence impurity migration, density build-up, heat flux to the divertor and to wall components as well as the performance of the ICRH heating system. Furthermore, the appropriate description of such a transport regime will also require a theoretical effort since the framework imposed by the large fluctuation level departs significantly from the local quasi-equilibrium that is generally assumed.

4.4. Summary and Implications for ITER.

The significant progress that has been made since the IPB in the area of SOL/divertor research is described in this chapter along with an assessment of the implications for ITER operation. A number of important advances in our understanding of key issues has been made (e.g. ELM power loads) as well as uncovering of new concerns (e.g. wall fluxes).

The study of steady state heat and particle loads to Plasma Facing Components (PFCs) has always been a central emphasis in the Divertor/SOL area. The recent better empirical fitting of an expanded database has allowed improved use of the midplane power SOL widths as the scaling parameter for ITER divertor heat load profiles. The presently estimated values are similar to those assumed in ITER modelling, although inclusion of kinetic effects in those models remains to be implemented. Both empirical and modelling predictions of in-out divertor heat load asymmetries are less certain although SOL flows and drifts appear to be the controlling physics. We expect that continued emphasis on inter-machine physics-based scaling work will provide more reliable divertor power profile estimates.

Because of their role in heat loads as well as impurity transport and migration, SOL flows have been the recent emphasis of both experimental and modelling investigations. A general understanding is emerging that flows are driven by two processes: perpendicular transport and drifts. Their relative contribution is still to be sorted out. Models are just beginning to achieve flows that approach those seen in experiment but considerable progress is needed.

While most of the energy flows to the divertor during steady-state this is not the case with particle fluxes; significant particle fluxes are inferred to reach main chamber PFCs in present experiments. These are associated with turbulence whereby filaments (along the field) of high density plasma travel radially at high velocity (~ 0.5 km/s), reaching the first wall before the particles can be lost parallel to the field. Analytical models and codes handling this effect are

still in development and comparison with experiment is limited. Furthermore, it is not clear how models of turbulence will be properly interfaced with the present complement of edge fluid codes. Initial empirical extrapolations of these fluxes to ITER, based on inter-machine experiments, indicate that such fluxes should not pose a problem for the lifetime of first-wall components. Given that the present empirical base for such extrapolation is minimal, further measurements and code development/validation would be very important to give more confidence in this optimistic ITER extrapolation.

Transient heat loads in the form of ELMs and disruptions, are presently the most serious challenge to PFC integrity and lifetime. Significant progress has been made in the determination of the spatial and temporal characteristics of the energy deposition at the divertor target during ELMs. On the basis of these measurements, an empirical extrapolation of the time-dependence of the ELM power pulse delivered to the ITER divertor plates has been developed. Modelling by kinetic SOL codes can describe some of the features identified in the data, but further detailed validation of these modelling tools is required before the predictions for ITER can be considered quantitative.

The magnitude of the ELM energy loss delivered to the plates in ITER relevant conditions (high density, high confinement H-modes) has been determined across most experimental devices and a physics-based scaling derived. The scaling of Type I ELM (proposed operating regime for ITER) energy loads at the ITER divertor gives values that will be close to or above the limits for material damage (sublimation/melting) and could lead to a reduced lifetime of the divertor target. The uncertainty in these estimates is still considerable. Alternative ELM regimes with high confinement, as well as regimes with smaller Type I ELMs, have been identified, which, if proven applicable to ITER, will lead to acceptable heat loads. Further studies of all of these regimes should be pursued together with the development of modelling tools for the transport of ELM energy to all PFCs.

In the period since the IPB it has been found that a significant fraction of the ELM energy (up to ~ 50% for very large ELMs) can be deposited on main chamber PFCs and not in the divertor. ELMs lead to a fast radial expulsion of ions and electrons from the core – in essence carrying plasma energy from the pedestal directly to main chamber PFCs. The radial transit time of the ELM is similar to the ion energy parallel loss time, such that ELM main chamber fluxes are of similar magnitude to those reaching the divertor. This raises concerns regarding the ITER Be wall and upper divertor lifetime. The characterization of these energy fluxes is made difficult by the poloidally/toroidally discontinuous character of the fluxes, and a physics based inter-machine extrapolation to ITER remains to be done. Certainly, given the implications for main chamber PFCs, further experiments and model development/validation are urgently needed.

The migration of PFC material around the chamber has important implications for first-wall lifetime, core impurity levels, and T retention. For standard ion B×∇B drift towards the

dominant divertor, the main chamber and outer divertor are generally found to be net erosion zones with the inner divertor region being a zone of net deposition. Details of the deposition are linked to divertor operating conditions, specifics of the divertor geometry, and the SOL flows which transport the eroded material over large distances. Models are still far from being able to reproduce present erosion and migration observations and so predictions for ITER are very uncertain. Further experiments with C^{13} and metallic tracers combined with detailed modelling should continue to be pursued.

The probability of an impurity reaching the core plasma launched from a given PFC location (screening) has been investigated in many experiments. In general, it is found that main chamber produced impurities are ~ 10 times more likely to reach the core than those launched from the divertor. The uncertainty in the modelling of the impurity transport, both for material migration and core contamination, is linked to the uncertainties in SOL flows and radial impurity diffusivity. The former is, as mentioned earlier, the subject of intense experimental and modelling effort and the situation should improve there. However, our knowledge is very limited regarding the impurity diffusivity (or convective velocity) in the SOL and whether it is dependent on charge state. The areas of impurity migration and core contamination are thus linked in some aspects of their limitations, and similarly need considerable input to reduce the uncertainties of the models.

The details of material properties as well as that of mixed materials have gained more emphasis since the IPB. New results on the flux dependence of carbon chemical sputtering and its reduction under detached conditions indicate that steady state carbon erosion can be expected to be much smaller for the ITER divertor than originally expected. On the other hand, recent results have raised concerns about the integrity of CFC carbon under transient loads due to the anisotropies introduced by the fibres. Whether this will be a problem for ITER relevant loads remains to be assessed by experiment and modelling in dedicated facilities.

Although the properties of Be are not in doubt, new information indicates that its use may add more risk for ITER operation than had been previously thought. The first issue, raised earlier, is the realization that significant heat loads of, as yet, poorly quantified nature, may result in localized melting of Be PFC surfaces, reducing wall PFC lifetime. JET has shown that it is possible to operate a device with damaged Be without deleterious effects for ITER relevant high density/confinement conditions, but the low density operation is more restricted. A second materials issue involving Be is its effect on the properties of W when deposited on such surfaces. Alloys can be formed which potentially have poorer properties than the original W. The use of Be may also lead to positive mixed materials effects. It is expected that Be eroded from main chamber surfaces will arrive at C divertor surfaces and assist in suppressing C chemical erosion and the associated T retention. All of the above mixed materials questions are relatively new and experiments, both in the laboratory and in tokamaks should be

encouraged. The modelling of the level of mixing expected in ITER is, of course, dependent on better understanding of impurity transport as described above.

The present plans for ITER include tungsten covering the dome and much of the divertor plates. High-Z PFC operation in current devices has shown that it is possible to operate ITER relevant plasmas in high density/confinement conditions while maintaining low core impurity concentrations. This, and the use of central heating to reduce core levels in certain operating regimes, bodes well for ITER, although the uncertainty in modelling of W effects on the core requires the development of better models of impurity transport in general.

The plans for ITER call for eventual switching to an all W divertor and, potentially, its extensive use elsewhere in the machine for reasons of T retention (reducing it), as well as reactor relevance. The main concern over such a change is the melting of W under transient loads (and the associated implications for machine operability) and the possible accumulation of W impurities in discharges with ITBs. Further experiments to control the energy loads during ELM and disruption transients, and on W density control during ITBs, are necessary to justify an increase of the W coverage in ITER from the one presently foreseen.

We now have a better idea of where T is retained in PFC and other vessel surfaces. Present experience with carbon PFC tokamaks indicates that T is retained primarily through co-deposition with C, mainly at the inner divertor although a significant fraction (~ 15-30%) can be found around the chamber in tile gaps. However, the C deposition rate has been shown to vary in location and rate with discharge equilibrium and divertor geometry; it is a complex multi-step process dependent on C chemical erosion yield, sticking coefficients of hydrocarbons and plasma flux profiles. Models of every step of this process need improvement.

The tritium inventory, both in-vessel, and on site, will be a central operational issue for any BPX due to safety considerations and operational limits on the level of T inventory. The ITER specification for the fraction of injected T that can be retained in-vessel is 0.1%. The little tokamak tritium experience that exists implies much higher values, even after cleaning efforts. More extensive studies with D under a variety of divertor geometries and operating conditions have resulted in lower levels of D retention, but generally still more than an order of magnitude higher than the ITER guideline. Because of the uncertainties of extrapolating T retention rates from present all-C-wall experiments to a BPX, in which the surface area of C-clad PFCs will be a small fraction of all PFC surfaces, development of efficient T removal methods is required. Removal methods have been developed along various lines: photonic cleaning, oxidation and RF plasma conditioning techniques. In general such techniques have been demonstrated to remove T, but a T removal rate at the level required in ITER remains to be demonstrated. Experiments using these techniques both in well characterised laboratory conditions and in tokamak devices are highly desirable. Such experiments should also address

the effect on T removal rates introduced by different levels and types of mixed materials, as well as the efficacy of T removal from difficult to reach locations (e.g. tile gaps).

He and H exhaust was demonstrated in the IPB to be of a level needed to keep ITER He concentrations under an acceptable value. New experiments with ITB plasmas have shown that, although the situation is slightly worsened due to the improved impurity confinement, it is still within acceptable limits for current tokamaks. This bodes well for a BPX-like device.

The key neutral issues which remain to be addressed experimentally in conjunction with modelling are those related to BPX specific conditions : the effect of n-n and ion-neutral reactions on the divertor solution and the trapping of Lyman series radiation lines. These effects can already be seen to a lesser extent in present experiments than in a BPX and can have a large influence on the expected divertor conditions (detachment, ionization balance and neutral pressure) and He removal. Such studies should be the subject of future experimental/code validation studies for which the models are being presently developed.

Fuelling of current experiments and how it scales with plasma conditions is fairly well understood. Pellet injection from the inside edge of the torus seems the most appropriate tool to provide the required fuelling in ITER. Further information is needed on alternative techniques, such as supersonic gas and Compact Toroid injection. In addition, detailed modelling of well diagnosed fuelling experiments with edge parameters (plasma pressure, density and temperature) close to those expected at the edge of ITER would be necessary to make more accurate predictions of the fuelling efficiency.

In summary, ITER will itself be an experiment in edge physics and plasma-wall interactions whose detailed outcome has many uncertainties. However, we believe that, by focusing current experimental capabilities on preparing for ITER operation, we will be able to ensure that we have the operational tools and understanding of the underlying physics to avoid or deal with problems as they arise.

4.5. References.

[1] Goetz, J.A., et al., Phys Plasmas **6** (1990) 1899.

[2] Herrmann, A., Plasma Phys. and Control. Fusion **44** (2002) 883.

[3] Takenaga, H., et al., Fusion Sci. and Tech. **42** (2002) 327.

[4] Kukushkin, A.S., et al., Fusion Eng. Des. **65** (2003) 355.

[5] Reichle, R., et al., Proc. 18th EPS Conference on Contr. Fusion and Plasma Physics, Berlin, 1991, ECA Vol 15C, D27, III-105.

[6] Asakura, N., et al., Nucl. Fusion **39** (1999) 1983.

[7] Reichle, R., et al., Physica Scripta **T111** (2004) 107.

[8] Andrew P., et al., J. Nucl. Mater. **337-339** (2005) 99.

[9] DelaChambre E., et al., J. Nucl. Mater. **337-339** (2005) 1069.

[10] Hildebrandt, D., et al., J. Nucl. Mater. **337-339** (2005) 1064.

[11] Stangeby, P.C., "The Plasma Boundary of Magnetic Fusion Devices", Plasma Physics Series, IOP Publishing Ltd., Bristol, 2000.

[12] Riccardo, V., et al., Plasma Phys. and Control. Fusion **43** (2001) 881.

[13] Matthews, G.F., et al., J.Nucl. Mater. **290-293** (2001) 668.

[14] Herrmann, A., et al., J. Nucl. Mater. **313-316** (2003) 759.

[15] Leonard, A.W., et al., J. Nucl. Mater. **266-269** (1999) 109.

[16] Eich, T., et al., 28th EPS Conference on Contr. Fusion and Plasma Phys., Funchal, Portugal, 2001, ECA Vol. 25A (2001) 1809.

[17] Fundamenski, W., and Sipilä, S., Nucl. Fusion **44** (2004) 20.

[18] ITER Physics Basis Editors, Nucl. Fusion **39** (1999) 2137.

[19] Fundamenski, W., et al., J. Nucl. Mater. **337–339** (2005) 305.

[20] Kukushkin, A.S., et al., Nucl. Fusion **43** (2003) 716.

[21] Fundamenski, W., et al., Nucl. Fusion **45** (2005) 950.

[22] Kallenbach, A., et al., Plasma Phys. Control. and Fusion **46** (2004) 431.

[23] Kempenaars, M., et al, 30th EPS Conf. on Contr. Fusion and Plasma Physics, St. Petersburg, Russia, 2003, ECA Vol. 27A, P-1.56.

[24] Fundamenski, W., et al., J. Nucl. Mater. **313-316** (2003) 787.

[25] Chankin, A., J. Nucl. Mater. **241-243** (1997) 199.

[26] Sipila, S., et al., 30th EPS Conf. on Contr. Fusion and Plasma Physics, St. Petersburg, Russia, Vol. 27A, 2003, P-3.144.

[27] Pitts, R. A., et al., J. Nucl. Mater. **337-339** (2005) 146.

[28] Loarte, A., et al., J. Nucl. Mater. **266-269** (1999) 587.

[29] Kukushkin, A.S., et al., Nucl. Fusion **42** (2002) 187.

[30] Lasnier, C.J., et al., Nucl. Fusion **38** (1998) 1225.

[31] Eich, T., et al., J. Nucl. Mater. **337-339** (2005) 669.

[32] Schaffer, M.J., et al., Nucl. Fusion **37** (1997) 83.

[33] Rognlien, T.D., et al., J. Nucl. Mater. **266-269** (1999) 654.

[34] Borrass, K., J. Nucl. Mater. **290-293** (2001) 551.

[35] Schneider, R., et al., Contrib. Plasma Phys. **40** (2000) 328-333.

[36] Kim, J.W., "An analysis of the anomalous transport of the plasma edge in ASDEX Upgrade", Ph.D. Thesis, University of Muenchen (2002).

[37] Simonini, R., et al, Contrib. Plasma Phys. **34** (1994) 368.

[38] Itoh, S.I., and Itoh, K., Plasma Phys. and Control. Fusion **36** (1994) 1845.

[39] Connor, J.W., et al., Nucl. Fusion **39** (1999) 169.

[40] Harrison, M.F.A., et al., Nuclear Technology/Fusion **3** (1983) 432.

[41] Counsell, G.F., et al., J. Nucl. Mater. **266-269** (1999) 91.

[42] Erents, S.K., and Stangeby, P.C., Nucl. Fusion **38** (1998) 1637.

[43] Neuhauser, J., et al., Plasma Phys.and Control. Fusion **31** (1989) 1551.

[44] McCormick, G.K., and Pietrzyk, Z.A., J. Nucl. Mater. **162-164** (1989) 264.

[45] McCormick, G.K., et al., in Controlled Fusion and Plasma Physics (Proc. 20th Eur. Conf. Lisbon, 1993), European Physical Society, Geneva (1993) Vol. 2, 587.

[46] Bosch, H.S., et al., J. Nucl. Mater. **220-223** (1995) 558.

[47] Rowan, W.L., et al., J. Nucl. Mater. **220-222** (1995) 668.

[48] Fenstermacher, M.E., et al., J. Nucl. Mater. **220-222** (1995) 330.

[49] Boedo, J.A., et al., Phys. Plasmas **8** (2001) 4826.

[50] LaBombard, B., et al., Phys. Plasmas **2** (1995) 2242.

[51] LaBombard, B., et al., J. Nucl. Mat. **290-293** (2001) 995.

[52] Asakura, N., et al., J. Nucl. Mater. **241-243** (1997) 559.

[53] Erents, S.K., et al., J. Nucl. Mater. **241-243** (1997) 433.

[54] Boedo, J.A., et al., Rev. Sci. Instrum. **69** (1998) 2663.

[55] Pitts, R.A., et al., J. Nucl. Mater. **290-293** (2001) 940.

[56] Umansky, M.V., et al., Phys. Plasmas **5** (1998) 3373.

[57] Umansky, M.V., et al., Phys. Plasmas **6** (1999) 2791.

[58] LaBombard, B., et al., Nucl. Fusion **40** (2000) 2041.

[59] LaBombard, et al., J. Nucl. Mater. **241-243** (1997) 149.

[60] Shimizu, K., et al., J. Nucl. Mater. **196-198** (1992) 476.

[61] Tsui, H.Y.W., et al., J. Nucl. Mater. **220-222** (1995) 672.

[62] Pitcher, C.S., et al., Phys. Plasmas **7** (2000) 1894.

[63] Pitcher, C.S., et al., J. Nucl. Mater. **290-293** (2001) 812-819.

[64] Lipschultz, B., et al., Plasma Phys. and Control. Fusion **44** (2002) 733.

[65] Schneider, R., et al., J. Nuc. Mater. **266-269** (1999) 175.

[66] Bosch, H.S., et al., Plasma Phys. and Control. Fusion **41** (1999) A401.

[67] Kallenbach, A., et al., Nuclear Fusion **43** (2003) 573.

[68] Whyte, D.G., et al., Plasma Phys. and Control. Fusion **47** (2005) 1579.

[69] Loarte, A., Plasma Phys. and Control. Fusion **43** (2001) R183.

[70] Allen, S., et al., J. Nucl. Mater. **266-269** (1999) 168.

[71] Vlases, G.C., et al., J. Nucl. Mater. **266-269** (1999) 160.

[72] Lipschultz, B., et al., in Fusion Energy 2000 (Proc. 18th Int. Conf. Sorrento, 2000) (Vienna: IAEA) CD-ROM file EX5/6 and http://www.iwww.iaea.org/programmes/ripc/physics/fec2000/html/node1.htm.

[73] McCormick, G.K., et al., J. Nucl. Mater. **196-198** (1992) 264.

[74] LaBombard, B., et al., J. Nucl. Mater. **220-222** (1995) 976.

[75] McCormick, G.K., et al., J. Nucl. Mat. **266-269** (1999) 99.

[76] Suttrop, W., et al., J. Nucl. Mater. **266-269** (1999) 118.

[77] Neuhauser, J., et al., Plasma Phys. and Control. Fusion **44** (2002) 855.

[78] LaBombard, B., et al., in Fusion Energy 2002 (Proc. 19th Int. Conf. Lyon, 2002) (Vienna: IAEA) CD-ROM file EX/D2-1 and http://www.iaea.org/programmes/ripc/physics/fec2002/html/fec2002.htm.

[79] Kim, J.W., et al., J. Nucl. Mater. **290-293** (2001) 644.

[80] Greenwald, M., Plasma Phys. and Control. Fusion **44** (2002) 27.

[81] Whyte, D.G., Physica Scripta **T111** (2004) 34.

[82] Rudakov, L., et al., Plasma Phys. and Control. Fusion **44** (2002) 717.

[83] Boedo, J.A., et al., J. Nucl. Mater. **313-316** (2003) 813.

[84] Zweben, S.J., et al., Phys. Plasmas **9** (2002) 1981.

[85] Terry, J.L., et al., Phys. Plasmas **10** (2003) 1739.

[86] Boedo, J.A., et al., Phys. Plasmas **10** (2003) 1670.

[87] Hidalgo, C., et al., J. Nucl. Mater. **313-316** (2003) 863.

[88] Zweben, S.J., and Gould, R.W., Nucl. Fusion **25** (1985) 171.

[89] Endler, M., et al., Nucl. Fusion **35** (1995) 1307.

[90] Filippas, A.V., et al., Phys. Plasmas **2** (1995) 839.

[91] Nielsen, A.H., et al., Phys. Plasmas **3** (1996) 1530.

[92] Joseph, B.K., et al., Phys. Plasmas **4** (1997) 4292.

[93] Heller, M.V.A.P., et al., Phys. Plasmas **6** (1999) 846.

[94] Carreras, B.A., et al., Phys. Plasmas **6** (1999) 1885.

[95] Jha, R., et al., Phys. Plasmas **10** (2003) 699.

[96] Antar, G.Y., et al., Phys. Plasmas **10** (2003) 419.

[97] Zweben, S.J., and Medley, S.S., Phys. Fluids **1** (1989) 2058.

[98] LaBombard, B., and Lipschultz, B., Nucl. Fusion **27** (1987) 81.

[99] Tynan, G.R., et al., Phys. Rev. Lett. **68** (1992) 3032.

[100] Lipschultz, B., et al., in Controlled Fusion and Plasma Physics Proc. 30th Eur. Conf St. Petersburg, Russia, Vol. 27A, 2003, P-3.197.

[101] Lipschultz, B., et al., Plasma Phys. and Control. Fusion **47** (2005) 1559.

[102] Stangeby, P.C., J. Nucl. Mater. **121** (1984) 55.

[103] Stangeby, P.C., Phys. Plasmas **9** (2002) 3489.

[104] Janeschitz, G., et al., J. Nucl. Mater. **196-198** (1992) 380.

[105] Matthews, G.F., et al., J. Nucl. Mater. **196-198** (1992) 374.

[106] Lipschultz, B., et al., J. Nucl. Mater. **290-293** (2001) 286.

[107] Whyte, D. G., et al., Nucl. Fusion **41** (2001) 1243.

[108] Loarte, A., et al., in Controlled Fusion and Plasma Physics (Proc. 20th Eur. Conf. Lisbon, 1993), Vol.17C, Part II, European Physical Society, Geneva (1993) 555.

[109] Pitcher, C.S., et al., in Controlled Fusion and Plasma Physics (Proc. 20th Eur. Conf. Lisbon, 1993), Vol.17C, Part I, European Physical Society, Geneva (1993) 291.

[110] Asakura, N., et al., Phys. Rev. Lett. **84** (2000) 3093.

[111] Erents, S.K., et al., Plasma Phys. and Control. Fusion **42** (2000) 905.

[112] Asakura, N., et al., Plasma Phys. and Control. Fusion **44** (2002) 2101.

[113] Boedo, J.A., et al., J. Nucl. Mater. **266-269** (1999) 783.

[114] LaBombard, B., et al., Nucl. Fusion **44** (2004) 1047.

[115] Erents, S.K., et al., Plasma Phys. and Control. Fusion **46** (2004) 349.

[116] Hutchinson, I.H., Phys. Rev. **A37** (1988) 4358.

[117] Jablonski, D., et al., J. Nucl. Mater. **241-243** (1997) 782.

[118] LaBombard, B., et al., J. Nucl. Mater. **266-269** (1999) 571.

[119] Pitcher, C.S., et al., J. Nucl. Mater. **266-269** (1999) 1009.

[120] Isler, R.C., et al., J. Nucl. Mater. **266-269** (1999) 376.

[121] Stangeby, P.C., and Chankin, A.V., Nucl. Fusion **36** (1996) 839.

[122] Chankin, A.V., and Stangeby, P.C., Plasma Phys. and Control. Fusion **38** (1996) 1879.

[123] Porter, G.D., et al., J. Nucl. Mater. **313-316** (2003) 1085.

[124] Rozhansky, V.A., et al., Nucl. Fusion **41** (2001) 387.

[125] Bonnin, X. et al., J. Nucl. Mater. **313-316** (2003) 909.

[126] Chankin, A.V., et al., J. Nucl. Mater. **290-293** (2001) 518.

[127] Bonnin X., et al., J. Nucl. Mater. **337-339** (2005) 301.

[128] LaBombard, B., et al., Phys. Plasmas **8** (2001) 2107.

[129] Boswell, C.J., et al., J .Nucl. Mater. **290-293** (2001) 556.

[130] Boedo, J.A., et al., Phys. Plasmas **7** (2000) 1075.

[131] Asakura, N., et al., J. Nucl. Mater. **313-316** (2003) 820.

[132] Leonard, A.W., et al., Phys. Rev. Lett. **78** (1997) 4769.

[133] Hatayama, A., et al., Nucl. Fusion **40** (2000) 2009.

[134] ITER Technical Basis, ITER EDA Documentation Series No. 24, IAEA, Vienna 2002.

[135] Dumortier, P., et al., Plasma Phys. and Control. Fusion **44** (2002) 1845.

[136] Sakurai, S., et al., J. Nucl. Mater. **290-293** (2001) 1002.

[137] Kubo, H., et al., Nucl. Fusion **41** (2001) 227.

[138] Konoshima, S., et al., Plasma Phys. and Control. Fusion **43** (2001) 959.

[139] Konoshima, S., et al., J. Nucl. Mater. **313-316** (2003) 888.

[140] Takenaga, H., et al., Nucl. Fusion **45** (2005) 1618.

[141] Asakura, N., et al., Nucl. Fusion **44** (2004) 503.

[142] Matthews, G.F., J. Nucl. Mater. **337-339** (2005) 1.

[143] Kallenbach, A., et al., Plasma Phys. and Control. Fusion **38** (1996) 2097.

[144] Rapp, J., et al., Nucl. Fusion **44** (2004) 312.

[145] Matthews, G.F., et al., Nucl. Fusion **39** (1999) 19.

[146] Kubo, H., et al., J. Nucl. Mater. **313-316** (2003) 1197.

[147] Mertens, V., et al., Fusion Eng. Des. **66-68** (2003) 119.

[148] Lang, P.T., et al., Nucl. Fusion **43** (2003) 1110.

[149] Kallenbach, A., et al., J. Nucl. Mater. **290-293** (2001) 639.

[150] Puiatti, M., et al., Plasma Phys. and Control. Fusion **44** (2002) 1863.

[151] Rice, J.E., et al., Nucl. Fusion **42** (2002) 510.

[152] Neu, R., et al., J. Nucl. Mater. **313-316** (2003) 116.

[153] Dux, R., et al., Plasma Phys. and Control. Fusion **45** (2003) 1815.

[154] Takenaga, H., et al., Nucl. Fusion **43** (2003) 1235.

[155] Federici, G., et al., Plasma Phys. and Control. Fusion **45** (2003) 1523.

[156] Wuerz, H., et al., J. Nucl. Mater. **290-293** (2001) 1138.

[157] Pestchanyi, S.E., et al., Plasma Phys. and Control. Fusion **44** (2002) 845.

[158] Bazylev, B., et al., J. Nucl. Mater. **337-339** (2005) 766.

[159] Landman, I.S., et al., J. Nucl. Mater. **337-339** (2005) 761.

[160] Loarte, A., Physica Scripta **T111** (2004) 13.

[161] Federici, G., et al., J. Nucl. Mater. **337-339** (2005) 684.

[162] Eich, T., et al., J. Nucl. Mater. **313-316** (2003) 919.

[163] Fenstermacher, M., et al., Plasma Phys. and Control. Fusion **45** (2003) 1597.

[164] Loarte, A., et al., Phys. Plasmas **11** (2004) 2668.

[165] Loarte, A., et al., J. Nucl. Mater. **313-316** (2003) 962.

[166] Loarte, A., et al., Plasma Phys. and Contr. Fusion **45** (2003) 1549.

[167] Kirk, A., et al., J. Nucl. Mater. **313-316** (2003) 1081.

[168] Bergmann, A., Nucl. Fusion **42** (2002) 1162.

[169] Tskhakaya, D., et al., Proc. Workshop on Theory of Fusion Plasmas, Varenna, Italy, 2004.

[170] Jachmich, S., et al., Proc. 28th European Physical Society Conference on Plasma Physics and Controlled Fusion, Portugal, Vol. 25A, 2002, P-4.079.

[171] Pitts, R.A., et al., Nucl. Fusion **43** (2003) 1145.

[172] Loarte, A., et al., Plasma Phys. and Contr. Fusion **44** (2002) 1815.

[173] Leonard, A.W., et al., Plasma Phys. and Control. Fusion **44** (2002) 945.

[174] Urano, H., et al., Plasma Phys. and Contr. Fusion **45** (2003) 1571.

[175] Eich, T., et al., Phys. Rev. Lett. **91** (2003) 195003.

[176] Evans, T., et al., J. Nucl. Mater. **220-222** (1995) 235.

[177] Counsell, G.F., et al., Proc. 30th European Physical Society Conference on Plasma Physics and Controlled Fusion, St. Petersburg, Russia, Vol. 27A, 2003, P-3.202.

[178] Leonard, A.W., et al., J. Nucl. Mater. **241-243** (1997) 628.

[179] Asakura, N., et al., J. Nucl. Mater. **266-269** (1999) 182.

[180] Counsell, G.F., et al., Plasma Phys. and Control. Fusion **44** (2002) 827.

[181] Counsell, G.F., et al., Plasma Phys. and Control. Fusion **44** (2002) B23.

[182] Petrie, T.W., et al., J. Nucl. Mater. **313-316** (2003) 804.

[183] Connor, J.W., et al., Phys. Plasmas **5** (1998) 2687.

[184] Snyder, P.B., et al., Phys. Plasmas **6** (2002) 2037.

[185] Groth, M., et al., J. Nucl. Mater. **313-316** (2003) 1071.

[186] Leonard, A., et al., Phys. Plasmas **10** (2003) 1765.

[187] Zeng, L., et al., Plasma Phys. and Control. Fusion **46** (2004) 121.

[188] Herrmann, A., Plasma Phys. and Control. Fusion **46** (2004) 971.

[189] Nunes, I., et al., Nucl. Fusion **44** (2004) 883.

[190] Ghendrih, Ph., et al., J. Nucl. Mater. **313-316** (2003) 914.

[191] Gonçalves, B., et al., Plasma Phys. and Control. Fusion **45** (2003) 1627.

[192] Gill, R.D., et al., Nucl. Fusion **38** (1998) 1461.

[193] Chankin, A.V., et al., J. Nucl. Mater. **313-316** (2003) 828.

[194] Fundamenski, W., et al., Plasma Phys. and Control. Fusion **46** (2004) 233.

[195] Krasheninnikov, S.I., Phys. Lett. A **283** (2001) 368.

[196] D'Ippolito, D.A., et al., Phys. Plasmas **9** (2002) 222.

[197] Silva, C., et al., J. Nucl. Mater. **337-339** (2005) 722.

[198] Leonard, A.W., et al., J. Nucl. Mater. **313-316** (2003) 768.

[199] Janeschitz, G., et al., J. Nucl. Mater. **290-293** (2001) 1.

[200] Oyama, N., et al., Nucl. Fusion **44** (2004) 582.

[201] Wilson, H.R., et al., Phys. Rev. Lett. **92** (2004) 175006.

[202] Loarte, A., et al., Nucl. Fusion **38** (1998) 331.

[203] Schneider, R., et al., Fusion Energy 1996 (Proc. 16th Int. IAEA Conference, Montreal, 1996) Vol. 2, IAEA, Vienna (1997) 465.

[204] Monier-Garbet, P., et al., Proc. 30th European Physical Society Conference on Plasma Physics and Controlled Fusion, St. Petersburg, Russia, Vol. 27A, 2003, P-1.095.

[205] Loarte, A., et al., in Fusion Energy 2000 (Proc. 18th Int. Conf. Sorrentto, 2000) (Vienna: IAEA) CD-ROM file ITERP/11R and http://www.iaea.org/programmes/ripc/physics/fec2000/html/node1.htm.

[206] Wenzel, U., et al., Nucl. Fusion **39** (1999) 873.

[207] Uesugi, Y., et al., J. Nucl. Mater. **290-293** (2001) 1134.

[208] Ohno, N., et al., Nucl. Fusion **41** (2001) 1055.

[209] Takamura, S., et al., Plasma Sources and Sci. Technol. **11** (2002) A42.

[210] Uesugi, Y., et al., Proc. 29th European Physical Society Conference on Plasma Physics and Controlled Fusion, Montreux, Switzerland, Vol. 26B, 2002, P-1.087.

[211] JET Team (prepared by R. Monk), Nucl. Fusion **39** (1999) 1751.

[212] Bosch, H.S., et al., J. Nuc. Mater. **266-269** (1999) 462.

[213] Kawashima, H., et al., Nucl. Fusion **39** (1999) 1679.

[214] Niemczewski, A., et al., Nucl. Fusion **37** (1997) 151.

[215] Takenaga, H., et al., Nucl. Fusion **41** (2001) 1777.

[216] Maingi, R., et al., Nucl. Fusion **39** (1999) 1187.

[217] Guo, H.Y., et al., Nucl. Fusion **40** (2000) 379.

[218] Loarte, A., et al., Proc. 24th Eur. Conf. on Controlled Fusion and Plasma Physics (Berchtesgaden, Germany), 1997, Vol. 21A, part III, p. 1049.

[219] Petrie, T.W., et al., J. Nucl. Mater. **337-339** (2005) 216.

[220] Lisgo, S., et al., J. Nucl. Mater. **337-339** (2005) 139.

[221] Stotler, D., et al., J. Nucl. Mater. **290-293** (2001) 967.

[222] Kukushkin, A.S., et al., in Fusion Energy 2004 (Proc. 20th Int. Conf. Vilamoura, 2004) (Vienna: IAEA) CD-ROM file IT/P3-24 and http://www-naweb.iaea.org/napc/physics/fec/fec2004/datasets/index.html.

[223] Reiter, D., et al., Plasma. Phys. and Control. Fus. **44** (2002) 1723.

[224] Maggi, C.F., et al., Proc. 26th EPS Conf. on Contr. Fusion and Plasma Phys., Maastricht, 1999, ECA Vol. 23J (1999) 201.

[225] Tsitrone, E., et al., Plasma Phys. and Control. Fusion **44** (2002) 701.

[226] Rapp, J., et al., Proc. 30th Eur. Conf. on Controlled Fusion and Plasma Physics, St. Petersburg, Russia, Vol. 27A, 2003, P-1.160.

[227] Maingi, R., et al., Nucl. Fusion **44** (2004) 909.

[228] Horton, L.D., et al., Nucl. Fus. **39** (1999) 1.

[229] Reiter, D., et al., Nucl. Fusion **30** (1990) 2141.

[230] Sakasai, A., et al., J. Nucl. Mater. **266-269** (1999) 312.

[231] Stork, D., et al., Proceedings of the 26th EPS Conf. on Contr. Fusion and Plasma Physics, Maastricht, The Netherlands, ECA Vol. **23J** (1999) 205.

[232] Bosch, H.S., et al., J. Nuc. Mater. **290-293** (2001) 836.

[233] Sakasai, A., et al., J. Nucl. Mater. **290-293** (2001) 957.

[234] Zastrow, K.-D., et al., Proceedings of the 29th EPS Conf. on Contr. Fusion and Plasma Physics, Montreux, Switzerland, ECA Vol. **26B** (2002) O-5.02.

[235] Horton, L.D., et al., in Plasma Physics and Controlled Nuclear Fusion Research 1992 (Proc. 14th Int. Conf. Wuerzburg, 1992), Vol. 1, p. 423, IAEA, Vienna (1993).

[236] Zastrow, K.-D., et al., Nucl. Fusion **45** (2005) 163.

[237] Finken, K.-H., et al., Proceedings of the 28th EPS Conf. on Contr. Fusion and Plasma Physics, Funchal, Portugal, ECA Vol. **25A** (2001) 1793.

[238] Groth, M., et al., J. Nucl. Mater. **290-293** (2001) 867.

[239] Klepper, C.C., et al., Nucl. Fusion **33** (1993) 533.

[240] Groth, M., et al., Nucl. Fusion **42** (2002) 591.

[241] Goetz, J.A., et al., Nucl. Fusion **41** (2001) 1751.

[242] Wade, M.R., et al., Nucl. Fusion **38** (1998) 1839.

[243] Itami, K., et al, J. Nucl. Mater. **266-269** (1999) 1097.

[244] Goetz, J.A., et al., J. Nucl. Mater. **266-269** (1999) 354.

[245] Fichtmueller, M., et al., J. Nucl. Mater. **266-269** (1999) 330.

[246] Coster, D.P., et al., J. Nucl. Mater. **290-293** (2001) 845.

[247] Reiser, D., et al., J. Nucl. Mater. **290-293** (2001) 953.

[248] Hogan, J.T., et al., J. Nucl. Mater. **313-316** (2003).

[249] Chung, T., et al., J. Nucl. Mater. **337-339** (2005) 109.

[250] Abou-Gabal, H.H., and Emmert, G.A., Nucl. Fusion **31** (1991) 407.

[251] Bachmann, P., et al., J. Nucl. Mater. **196-198** (1992) 865.

[252] Kubo, H., et al., Plasma Phys. and Control. Fusion **41** (1999) 747.

[253] Kukushkin, A.S., et al., Plasma Phys. and Control. Fusion **44** (2002) 931.

[254] Lumma, D., et al., Phys. Plasmas **4** (1997) 2555.

[255] Isler, R.C., et al., Phys. Plasmas **4** (1997) 2989.

[256] McCracken, G.M., et al., Nucl. Fusion **38** (1998) 619.

[257] Terry, J.L., et al., Phys. Plasmas **5** (1998) 1759.

[258] Krasheninnikov, S.I., et al., J. Nucl.Mater. **241-243** (1997) 283.

[259] Reiter, D., et al., J. Nucl.Mater. **241-243** (1997) 342.

[260] Lipschultz, B., et al., Physics Plasmas **6** (1999) 1907.

[261] Lipschultz, B., et al., Phys. Rev. Lett. **81** (1998) 1007.

[262] Maggi, C.F., et al., J. Nucl. Mater. **266-269** (1999) 867.

[263] Hollmann, E.M., et al., Phys. Plasmas **9** (2002) 1226.

[264] Fantz, U., and Heger, B., Plasma Physics and Control. Fus. **40** (1998) 2023.

[265] Fantz, U., et al., Plasma Phys. and Control. Fusion **43** (2001) 907.

[266] Fantz, U., et al., J. Nucl. Mater. **313-316** (2003) 743.

[267] Fantz, U., et al., J. Nucl. Mater. **290-293** (2001) 367.

[268] Ohno, N., et al., Phys. Rev. Lett. **81** (1998) 818.

[269] Nishijima, D., et al., Plasma Phys. and Control. Fusion **44** (2002) 597.

[270] Tonegawa, A., et al., J. Nucl. Mater. **313-316** (2003) 1046.

[271] Coad, J.P., et al., J. Nucl. Mater. **290-293** (2001) 224.

[272] Brooks, J.N., et al., J. Nucl. Mater. **313-316** (2003) 424.

[273] Federici, G., et al., J. Nucl. Mater. **313-316** (2003) 11.

[274] Federici G., et al., Nucl. Fus. **41** (2001) 1967.

[275] Philipps, V., et al., Vacuum **67** (2002) 399.

[276] Roth, J., et al., Nucl. Fusion **44** (2004) L21.

[277] Thoma, A., et al., Plasma Phys. and Control. Fus. **39** (1997) 1487.

[278] Wampler,W.R., et al., J. Nucl. Mater. **266-269** (1999) 217.

[279] Naujoks, D., et al., Nucl. Fusion **36** (1996) 671.

[280] Gafert J., et al., J. Nucl. Mater. **266-269** (1999) 365.

[281] Fenstermacher, M. E., et al., Plasma Phys. and Control. Fusion **41** (1999) A345.

[282] Krieger, K., et al., J. Nucl. Mater. **313-316** (2003) 327.

[283] Kirschner, A., et al., J. Nucl. Mater. **290-293** (2001) 238.

[284] Krieger, K., et al., J. Nucl. Mater. **307-311** (2002) 139.

[285] Pütterich, T., et al., Plasma Phys. and Control. Fusion **45** (2003) 1873.

[286] Federici, G., et al., J. Nucl. Mater. **290-293** (2001) 260.

[287] Neu, R., et al., Fusion Sci. and Tech. **44** (2003) 692.

[288] Higashijima, S., et al., J. Nucl. Mater. **266-269** (1999) 1078.

[289] Isler, R. C., et al., J. Nucl. Mater. **313-316** (2003) 873.

[290] Lipschultz, B., et al., Nucl. Fusion **41** (2001) 585.

[291] Geier, A., et al., J. Nucl. Mater. **313-316** (2003) 1216.

[292] Krieger, K., et al., J. Nucl. Mater. **337-339** (2005) 10.

[293] Krieger, K., et al., J. Nucl. Mater. **241-243** (1997) 684.

[294] Brooks, J.N., and Whyte, D.G., Nucl. Fusion **39** (1999) 525.

[295] Whyte, D. G., J. Nucl. Mater. **266-269** (1999) 67.

[296] Coad, J.P., et al., J. Nucl. Mater. **313-316** (2003) 419.

[297] Whyte, D. G., et al., J. Nucl. Mater. **290-293** (2001) 356.

[298] McCracken, G.M., et al., Nucl. Fus. **39** (1999) 41.

[299] Neu, R., et al., J. Nucl. Mater. **241-243** (1997) 678.

[300] Groth, M., et al., J. Nucl. Mater. **337-339** (2005) 425.

[301] Strachan, J. D., et al., Nucl. Fusion **43** (2003) 922.

[302] West, W. P., et al., J. Nucl. Mater. **313-316** (2003) 1211.

[303] Neu, R, et al., J. Nucl. Mater. **290-293** (2001) 206.

[304] Krieger, K., et al., J. Nucl. Mater. **266-269** (1999) 207.

[305] West, W. P., et al., J. Nucl. Mater. **290-293** (2001) 783.

[306] Tsitrone, E., et al., J. Nucl. Mater. **290-293** (2001) 331.

[307] Mayer, M., et al., Physica Sripta **T111** (2004) 55.

[308] Rubel, M., et al., J. Nucl. Mater. **313-316** (2003) 321.

[309] Likonen, J., et al., Fusion Eng. Des. **66-68** (2003) 219.

[310] Vainonen-Ahlgren, E., et al., J. Nucl. Mater. **337-339** (2005) 55.

[311] Gotoh, Y., et al., J. Nucl. Mater. **313-316** (2003) 370.

[312] Field, A.R., et al., Nucl. Fusion **36** (1996) 119.

[313] Asakura, N., et al., in Fusion Energy 2002 (Proc. 19th Int. Conf. Lyon, 2002) (Vienna: IAEA) CD-ROM file EX/D1-3 and http://www.iaea.org/programmes/ripc/physics/fec2002/html/fec2002.htm.

[314] Ohya, K., et al., Jap. J. Appl. Phys. Part 1 **42** (2003) 5769.

[315] Matthews, G. F., et al., Proceedings of the 30th Europ. Conf. on Controlled Fusion and Plasma Physics, Saint Petersburg, Russia, Vol. 27A, 2003, P-3.198.

[316] Likonen, J., et al., J. Nucl. Mater. **337-339** (2005) 60.

[317] Esser, H.G., et al., Physica Scripta **T111** (2004) 129.

[318] Wade, M.R., et al., J. Nucl. Mater. **337-339** (2005) 737.

[319] Asakura, N., et al., J. Nucl. Mater. **337-339** (2005) 712.

[320] Wienhold, P., et al., J. Nucl. Mater. **313-316** (2003) 311.

[321] Kawakami, R., and Ohya K., Jap. J. Appl. Phys. Part 1 **42** (2003) 3623.

[322] Merola, M., et al., J. Nucl. Mater. **307–311** (2002) 1524.

[323] ITER Project Integration Document G-A0-GDRD-6-04-09-09-R0.2-version 1.0, 2005.

[324] Kakudate, S., and Shibanuma, K., Fus. Eng. and Design **65** (2003) 133.

[325] Tesini, A., et al., ITER IT, "Technical Memorandum on requirements for first wall shutdown in ITER", 2005, rev. 3.

[326] Matthews, G.F., et al., J. Nucl. Mater. **241-243** (1997) 450.

[327] Kallenbach, A., et al., Nucl. Fusion **39** (1999) 901.

[328] Polevoi, A.R., et al., in Fusion Energy 2004 (Proc. 20th Int. Conf. Vilamoura, 2004) (Vienna: IAEA) CD-ROM file IT/P3-28 and http://www-naweb.iaea.org/napc/physics/fec/fec2004/datasets/index.html.

[329] Janev, R.K., and Reiter, D., Phys. Plasmas **11** (2004) 780.

[330] Pugno, R., et al., 30th EPS Conference on Contr. Fusion and Plasma Phys., St. Petersburg, Russia, Vol. 27A, 2003, P-1.153.

[331] Stamp, M., et al., J. Nucl. Mater. **290-293** (2001) 321.

[332] Vietzke, E., et al., "Amorphous Hydrogen Films", Les Editions de Physique, Paris 1987, p. 351.

[333] Roth, J., et al., J. Nucl. Mater. **337-339** (2005) 970.

[334] Brooks, J.N., et al., J. Nucl. Mater. **266-269** (1999) 58.

[335] Wuerz, H., et al., J. Nucl. Mater. **307–311** (2002) 60.

[336] Landman, I.S., et al., Physica Scripta **T111** (2004) 206. [336] Landman, I.S., et al., Physica Scripta **T111** (2004) 206.

[337] Naujoks, D., et al., Physica Scripta **T111** (2004) 80.

[338] Rohde, V., et al., Physica Scripta, **T111** (2004) 49.

[339] von Seggern, J., et al., J. Nucl. Mater. **313–316** (2003) 439.

[340] Masaki, K., et al., J. Nucl. Mater. **337-339** (2005) 553.

[341] von Seggern, J., et al., Physica Scripta **T81** (1999) 31.

[342] Pegourie, B., et al., Physica Sripta **T111** (2004) 23.

[343] Hsu, W.S., et al., J. Vac. Science and Tech. **A7** (1989) 1065.

[344] Coad, J.P., et al., J. Nucl. Mater. **241-243** (1997) 408.

[345] Roth, J., et al., Fusion Eng. Design **37** (1997) 465.

[346] Thomas, P.R., et al., J. Nucl. Mater. **176-177** (1990) 3.

[347] Campbell, D.J., et al., J. Nucl. Mater. **241-243** (1997) 379.

[348] Anderl, R. A., et al., J. Nucl. Mater. **273** (1999) 1.

[349] Causey, R.A., and Walsh, D.S., J. Nucl. Mater. **254** (1998) 84.

[350] Mayer, M., J. Nucl. Mater. **240** (1997) 164.

[351] Baldwin, M.J., et al., J. Nucl. Mater. **337-339** (2005) 590.

[352] Doerner, R.P., et al., J. Nucl. Mater. **290-293** (2001)166.

[353] Doerner, R.P., et al., J. Appl. Phys. **95** (2004) 4471.

[354] Whyte, D.G., and Davis, J.W., J. Nucl. Mater. **337-339** (2005) 560.

[355] Loarte, A., et al., J. Nucl. Mater. **337-339** (2005) 816.

[356] Lingertat, J., et al., J. Nucl. Mater. **241-243** (1997) 402.

[357] Philipps, V., et al., Plasma Phys. and Control. Fusion **42** (2000) B293.

[358] Yoshida, N., J. Nucl. Mater. **266–269** (1999) 206.

[359] Ciotti, M., et al., J. Nucl. Mater. **196-198** (1992) 725.

[360] Hutchinson, I.H., et al., Phys. Plasmas **1** (1994) 1511.

[361] Pospieszczyk, A., et al., J. Nucl. Mater. **290-293** (2001) 947.

[362] Neu, R., et al., Plasma Phys. and Control. Fusion **38** (1997) A165.

[363] Neu, R., et al., Nucl. Fusion **45** (2005) 209.

[364] May, M., et al., Plasma Phys. and Control. Fusion **41** (1999) 45.

[365] Apicella, M., et al., J. Nucl. Mater. **313-316** (2003) 269.

[366] Dux, R., et al., J. Nucl. Mater. **313- 316** (2003) 1150.

[367] Rapp, J., et al., Plasma Phys. and Control. Fusion **39** (1997) 1615.

[368] Apicella, M., et al., Nucl. Fusion **37** (1997) 381.

[369] Neu, R., et al., in Fusion Energy 2004 (Proc. 20th Int. Conf.nf. Vilamoura, 2004) (Vienna: IAEA) CD-ROM file EX/10-5 and http://www-naweb.iaea.org/napc/physics/fec/fec2004/datasets/index.html.

[370] Koch, R., et al., Fusion Eng. Des. **26** (1995) 103.

[371] Neu, R., et al., Plasma Phys. and Control. Fusion **44** (2002) 811.

[372] Stober, J., et al., Nucl. Fusion **43** (2003) 1265.

[373] Dux, R., et al., in Fusion Energy 2004 (Proc. 20th Int. Conf. Vilamoura, 2004) (Vienna: IAEA) CD-ROM file EXP6-14 and http://www-naweb.iaea.org/napc/physics/fec/fec2004/datasets/index.html.

[374] Maddaluno G., et al., J. Nucl. Mater. **241-243** (1997) 908.

[375] Loarte, A., et al., in Fusion Energy 2004 (Proc. 20th Int. Conf. Vilamoura, 2004) (Vienna: IAEA) CD-ROM file IT/P3-34 and http://www-naweb.iaea.org/napc/physics/fec/fec2004/datasets/index.html.

[376] Landman, I.S., and Würz, H., J. Nucl. Mater. **313-316** (2003) 77.

[377] Pappas, D., et al., J. Nucl. Mater. **266-269** (1999) 635.

[378] Verbeek, H., et al., Proc. of the 24th EPS Conference on Controlled Fusion and Plasma Physics, Berchtesgaden, 1997, Vol 21A, part IV, p. 1457.

[379] Rohde, V., et al., in Fusioon Energy 2002 (Proc. 19th Int. Conf. Lyon, 2002) (Vienna: IAEA) CD-ROM file EX/D1-4 and http://www.iaea.org/programmes/ripc/physics/fec2002/html/fec2002.htm.

[380] Causey, R.A., J. Nucl. Mater. **300** (2002) 91.

[381] Ogorodnikova, O., et al., J. Nucl. Mater. **313-316** (2003) 469.

[382] Rubel, M., et al., J. Nucl. Mater. **307-311** (2002) 111.

[383] Ueda, Y., et al., Nucl. Fusion **44** (2004) 62.

[384] Venhaus, T., et al., J. Nucl. Mater. **290-293** (2001) 505.

[385] Wang, W., et al., J. Nucl. Mater. **299** (2001) 124.

[386] Nishijima, D., et al., Nucl. Fus. **45** (2005) 669.

[387] Nishijima, D., et al., J. Nucl. Mater. **329-333** (2004) 1029.

[388] Jotaki, E., et al., Fusion Eng. Des. **36** (1997) 447.

[389] Nachtrieb, R.T., et al., J. Nucl. Mater. **266-269** (1999) 896.

[390] Gauthier, E., et al., J. Nucl. Mater. **241-243** (1997) 553.

[391] Esser, H.G., et al., J. Nucl. Mater. **241-243** (1997) 861.

[392] Xie, J.K., et al., J. Nucl. Mater. **290-293** (2001) 1155.

[393] Brakel, D., et al., J. Nucl. Mater. **290-293** (2001) 1160.

[394] de la Cal, E. and Gauthier, E., Plasma Phys. and Control. Fusion **47** (2005) 197.

[395] Hu, J.S., et al., "Plasma Phys. and Control. Fusion **47** (2005) 1271.

[396] Linsmeier, Ch., et al., J. Nucl. Mater. **290-293** (2001) 25.

[397] Goldstrass, P., and Linsmeier, Ch., J. Nucl. Mater. **290-293** (2001) 71.

[398] Okamoto, H., and Tanner, L. E., in "Phase Diagrams of Binary Tungsten Alloys", Eds. Naidu, S. V. and Rao, P., Indian Institue of Metals, Calcutta 1991.

[399] Doerner, R.P., et al., in Fusion Energy 2004 (Proc. 20th Int. Conf. Vilamoura, 2004) (Vienna: IAEA) CD-ROM file IT/P3-18 and http://www-naweb.iaea.org/napc/physics/fec/fec2004/datasets/index.html.

[400] Doerner, R.P., et al., J. Nucl. Mater. **342** (2005) 63.

[401] Wiltner, A., and Linsmeier, Ch., J. Nucl. Mater. **337-339** (2005) 951.

[402] Schmid, K., and Roth, J., J. Nucl. Mater. **313-316** (2003) 302.

[403] Roth, J., et al., J. Nucl. Mater. **250** (1997) 23.

[404] Schmid, K., and Roth, J., J. Nucl. Mater. **290-293** (2001) 96.

[405] Schmid, K., et al., J. Nucl. Mater. **337-339** (2005) 862.

[406] Goldstrass, P., et al., J. Nucl. Mater. **266-269** (1999) 581.

[407] Balden, M., et al., J. Nucl. Mater. **337-339** (2005) 980.

[408] Davis, J.W., and Haasz, A.A., J. Nucl. Mater. **255** (1998) 214.

[409] Poon, M., et al., J. Nucl. Mater. **283-287** (2000) 1062.

[410] Davis, J.W., and Haasz, A.A., J. Nucl. Mater. **266-269** (1999) 478.

[411] Davis, J.W., et al., J. Nucl. Mater. **290-293** (2002) 66.

[412] Barabash, V., et al., J. Nucl. Mater. **313-316** (2003) 42.

[413] Skinner, C. H., et al., J. Vac. Sci. Technol. **A14** (1996) 3267.

[414] Mueller, D., et al., Fus. Tech. **30** (1996) 840.

[415] Andrew, P., et al., Fusion Eng. Des. **47** (1999) 233.

[416] Peacock, A.T., et al., Fusion Eng. Des. **49-50** (2000) 745.

[417] Haasz, A.A. and Davis, J.W., "Hydrogen Retention in and Removal from Carbon Materials," Springer Series on Chem. Physics, Vol. 78, Springer-Verlag, Berlin, 2005.

[418] Bekris, N., et al., J. Nucl. Mater. **307-311** (2002) 1649.

[419] Skinner, C.H., et al., J. Nucl. Mater. **290-293** (2001) 486.

[420] Mueller, D., et al., Proc. 17th IEEE/NPSS Symp. Fus. Eng., (San Diego, USA, 1997) Ed. IEEE, Piscataway New Jersey, IEEE 97CH36131, Vol. 1 (1998) 279.

[421] Bekris, N., et al., J. Nucl. Mater. **313-316** (2003) 501.

[422] Philipps, V., et al., in Fusion Energy 2004 (Proc. 20th Int. Conf. Vilamoura, 2004) (Vienna: IAEA) CD-ROM file EX/10-1 and http://www-naweb.iaea.org/napc/physics/fec/fec2004/datasets/index.html.

[423] Mayer, M., et al., J. Nucl. Mater. **337-339** (2005) 119.

[424] Rohde, V., et al., J. Nucl. Mater. **337-339** (2005) 847.

[425] Tanabe, T., Kyushu University, 2004, private communication.

[426] Hirohata, Y., et al., J. Nucl. Mater. **337-339** (2005) 609.

[427] Bucalossi, J., et al., 28th EPS Conference on Contr. Fusion and Plasma Phys., Funchal, Portugal, 2001, ECA Vol. 25A (2001) 1629.

[428] Mertens,V., et al., 30th EPS Conference on Contr. Fusion and Plasma Phys., St. Petersburg, Russia, Vol. 27A, 2003, P-1.128.

[429] Loarer, T., et al., in Fusion Energy 2004 (Proc. 20th Int. Conf. Vilamoura, 2004) (Vienna: IAEA) CD-ROM file EX/P5-22 and http://www-naweb.iaea.org/napc/physics/fec/fec2004/datasets/index.html.

[430] von Seggern, J., et al., Physica Scripta , **T111** (2004) 118.

[431] Federici, G., et al., J. Nucl. Mater. **337-339** (2005) 40.

[432] Wienhold, P., et al., J. Nucl. Mater. **290-293** (2001) 362.

[433] Kirschner, A., et al., J. Nucl. Mater. **328** (2004) 62.

[434] Esser, H.G., et al., J. Nucl. Mater. **337-339** (2005) 84.

[435] Ehrhardt, A.B., and Langer, W.D., "Collisional Processes of Hydrocarbons in Hydrogen Plasmas", PPPL-2477, Princeton University, 1987.

[436] Janev, R.K., and Reiter, D., Collision Processes of Hydrocarbon Species in Hydrogen Plasmas, Jül-3966, 2002, ISSN 0944-2952.

[437] Alman, D.A., and Ruzic, D.N., J. Nucl. Mater. **313-316** (2003) 182.

[438] Eckstein, W., "Computer Simulation of Ion-Solid Interactions", Springer-Verlag, Berlin 1991.

[439] Eckstein.W., "Calculated Sputtering, Reflection and Range Values", MPI-Garching Report, IPP 9/132 (June 2002).

[440] Kirschner, A., et al., Plasma Phys. and Control. Fusion **45** (2003) 309.

[441] Tabarés, F.L., et al., Plasma Phys. and Control. Fusion **46** (2004) B381.

[442] Rubel, M., et al., Physica Scripta, **T111** (2004) 112.

[443] Litnovsky, A., et al., J. Nucl. Mater. **337-339** (2005) 917.

[444] Doerner, R.P., et al., Physica Sripta, **T111** (2004) 75.

[445] Schleußner, D., et al., J. Nucl. Mater. **266-269** (1999) 1296.

[446] McCarthy, K.A., et al., Fusion Eng. and Des. **42** (1998) 45.

[447] Piet, S. J., et al., Fusion Engineering (Proc. 17th IEEE/NPSS Symp. San Diego, 1997), IEEE, Piscataway, New Jersey, IEEE 97CH36131, Vol. 1 167 (1998).

[448] Rubel, M., et al., Nucl. Fusion **41** (2001) 1087.

[449] Bader, A., et al., Rev. Sci. Instrum. **75** (2004) 370.

[450] Counsell, G. F., and Wu, C. H., Physica Scripta **T91** (2001) 70.

[451] Skinner, C.H., et al., Physica Scripta. **T111** (2004) 92.

[452] Skinner, C.H., et al., J. Nucl. Mater. **313-316** (2003) 496.

[453] Haasz, A.A., et al., J. Vac. Sci. Technol. **A14** (1996) 184.

[454] Alberici, S., et al., J. Nucl. Mater. **266-269** (1999) 754.

[455] Haasz, A.A. and Davis, J.W., J. Nucl. Mater. **256** (1998) 65.

[456] Davis J. W., and Haasz A. A., Physica Scripta, **T91** (2001) 33.

[457] Philipps, V., et al., J. Nucl. Mater. **266-269** (1999) 386.

[458] Moormann, R., et al., Fusion Eng. Des. **49-50** (2000) 295.

[459] Lyssoivan, et al., Proc. 2nd Europhysics Topical Conf. on RF Heating and Current Drive of Fusion Devices, Brussels, Europhysics Conf. Abstracts ECA Vol. 22A (1998) 85.

[460] Xiao, B., et al., J. Nucl. Mater. **313-316** (2003) 163.

[461] Borrass, K., et al., Nuclear Fusion **39** (1999) 843.

[462] Kallenbach, A., et al., Nuclear Fusion **42** (2002) 1184.

[463] Mahdavi, M.A., et al., Nucl. Fusion **42** (2002) 52.

[464] Kallenbach, A., et al., J. Nucl. Mater. **337-339** (2005) 381.

[465] Porter, G.D., et al., Physics of Plasmas **5** (1998) 1410.

[466] Mahdavi, M.A., et al., Phys. Plasmas **10** (2003) 3984.

[467] Borrass, K., et al., Nucl. Fusion **37** (1997) 523.

[468] Krasheninnikov, S.I., et al., J. Nucl. Mater. **266-269** (1999) 251.

[469] Stober, J., et al., Nucl. Fusion **41** (2001) 1123.

[470] Saibene, G., et al., Plasma Phys. and Control. Fusion **44** (2002) 1769.

[471] Yao, L., et al., Nucl. Fusion, **38** (1998), 631.

[472] Yao, L., et al., Nucl. Fusion **41** (2001) 817.

[473] Gao, X., et al., Nucl. Fusion **40** (2000) 1875.

[474] Baldzuhn, J., et al., Proc. 30th Europ. Conf. Controlled Fusion and Plasma Physics, Saint Petersburg, Russia, Vol. 27A, 2003, P-4.166.

[475] Jiafu, D., et al., Plasma Phys. and Control. Fusion **44** (2002), 371.

[476] Bucalossi, J., et al., et al., in Fusion Energy 2002 (Proc. 19th Int. Conf. Lyon, 2002) (Vienna: IAEA) CD-ROM file EX/P4-04 and http://www.iaea.org/programmes/ripc/physics/fec2002/html/fec2002.htm.

[477] Loarer, T., et al., Proceedings of the 30th Europ. Conf. on Controlled Fusion and Plasma Physics, Saint Petersburg, Russia, Vol. 27A, 2003, P-1.161.

[478] Tsitrone, E., et al., Proceedings of the 30th Europ. Conf. Controlled Fusion and Plasma Physics, Saint Petersburg, Russia, Vol. 27A, 2003, O-2.5A.

[479] Lang, P.T., et al., Proc. 30th Europ. Conf. on Controlled Fusion and Plasma Physics, Saint Petersburg, Russia, Vol. 27A, 2003, P-1.129.

[480] Lang, P.T., et al., in Fusion Energy 2004 (Proc. 20th Int. Conf. Vilamoura, 2004) (Vienna: IAEA) CD-ROM file EX2/6 and http://www-naweb.iaea.org/napc/physics/fec/fec2004/datasets/index.html.

[481] Baylor, L.R., et al., J. Nucl. Mater. **313-316** (2003) 530.

[482] Lang, P.T., et. al., Phys. Rev. Lett. **79** (1997) 1487.

[483] Müller, H.W., et al., Phys. Rev. Lett. **83** (1999) 2199.

[484] Pégourié, B., et al., J. Nucl. Mater. **313-316** (2003), 539.

[485] Baylor, L.R., et al., Nucl. Fusion **37** (1997) 445.

[486] Lang, P.T., et al., Nucl. Fusion **41** (2001) 1107.

[487] Rozhansky, V.A., et al., Plasma Phys. and Control. Fusion **37** (1995) 399.

[488] Parks, P.B., et al., Physics of Plasmas **7** (2000) 1968.

[489] Baylor, L.R., et al., J. Nucl. Mater. **266-269** (1999) 457.

[490] Jones, T.T.C., et al., Contr. Fusion and Plasma Physics Vol. 24B (Proc. 27th EPS Conf., Budapest, 2000) paper OR04.

[491] Takenaga, H., et al., Phys. Plasmas **8** (2001) 2217.

[492] Kubo, H., et al., Phys. Plasmas **9** (2002) 2127.

[493] Geraud, A., et al., Fusion Technology, (Proc. 20th SOFT Conf.) Vol. 2 (1998), 942.

[494] Andelfinger, C., et al., Rev. Sci. Instrum. **64** (1993) 983.

[495] Geraud, A., et al., Fusion Eng. Des. **69** (2003) 5.

[496] Geraud, A., et al., J. Nucl. Mater. **337-339** (2005) 485.

[497] Watson, M.J., and Milnes, J., EFDA Task Final Report TW2-TTFD-VD25.

[498] Polevoi, A.R., et al., Nucl. Fusion **43** (2003) 1072.

[499] Polevoi, A.R., and Shimada, M., Plasma Phys. and Control. Fusion **43** (2001) 1525.

[500] Raman, R., et al., Nucl. Fusion **37** (1997) 967.

[501] Ogawa, T., et al., J. Nucl. Mater., **290-293** (2001) 454.

[502] Loarte, A., et al., J. Nucl. Mater. **266–269** (1999) 1123.

[503] Igitkhanov, Yu., et al., Proc. 21st EPS Conference on Contr. Fusion and Plasma Phys., Montpellier, France, 1994, ECA Vol. 18B (1994) 766.

[504] Kukushkin, A.S., and Runov, A.M., Contrib. Plasma Phys. **34** (1994) 204.

[505] Neuhauser, J., et al., Proc. 26th EPS Conf. Contr. Fusion Plasma Phys., Maastricht, 1999. Paper P4.040.

[506] Kukushkin, A.S., et al., M., Contrib. Plasma Phys. **40** (2000) 233.

[507] Pacher, H.D., et al., J. Nucl. Mater. **266–269** (1999) 1172.

[508] Taroni, A., et al., Controlled Fusion and Plasma Phys. (Proc. 22th Eur. Conf. Bournemouth, 1995), ECA vol. 19C, Part IV, European Physical Society, Geneva (1995) 297.

[509] Wesson, J., "Tokamaks". Oxford University Press, Oxford, 1997.

[510] Cohen, R., and Ryutov, D.D., Contrib. Plasma Phys. **44** (2004) 111.

[511] Kukushkin, A.S., et al., Proc. 26th EPS Conf. on Contr. Fusion and Plasma Phys., Maastricht, 1999, ECA Vol. 23J (1999) 1545.

[512] Kukushkin, A.S., et al., J. Nucl. Mater. **337–339** (2005) 50.

[513] Kukushkin, A.S., et al., Proc. 30th EPS Conference on Contr. Fusion and Plasma Phys., St. Petersburg, Russia, Vol. 27A, 2003, P-3.195.

[514] Kirschner, A., et al., J. Nucl. Mater. **313- 316** (2003) 444.

[515] Kukushkin, A.S., et al., Nucl. Fusion **45** (2005) 608.

[516] Kukushkin, A.S., et al., J. Nucl. Mater. **290–293** (2001) 887.

[517] Pacher, H.D., et al., J. Nucl. Mater. **313–316** (2003) 657.

[518] Coster, D.P., et al., in Fusion Energy 2002 (Proc. 19th Int. Conf. Lyon, 2002) (Vienna: IAEA) CD-ROM file TH/P2-13 and http://www.iaea.org/programmes/ripc/physics/fec2002/html/fec2002.htm.

[519] Monk, R.D., et al., Proc. 24th EPS Conf. Contr. Fusion Plasma Phys., Berchtesgaden, 1997, ECA Vol. 21A, p. 117.

[520] Pacher, G.W., et al., Nucl. Fusion **43** (2003) 188.

[521] Mukhovatov, V., et al., Nucl. Fusion **43** (2003) 942.

[522] Pacher, G.W., et al., Plasma Phys. and Control. Fusion **46** (2004) A257.

[523] Rozhansky, V.A., et al., J. Nucl. Mater. **313-316** (2003) 1141.

[524] Wiesen, S., et al., Proc. 30th EPS Conf. Contr. Fusion and Plasma Phys., St. Petersburg, Russia, Vol. 27A, 2003, P-3.194.

[525] LaBombard, B., et al., J. Nucl. Mat. **313–316** (2003) 995.

[526] Smick, N., et al., J. Nucl. Mater. **337–339** (2005) 281.

[527] Kirnev, G.S., et al., J. Nucl. Mater. **337–339** (2005) 271.

[528] Coster, D.P., et al., J. Nucl. Mater. **337– 339** (2005) 366.

[529] Heikkinen, J.A., et al., J. Computational Phys. **173** (2001) 527.

[530] Kurki-Suonio, T., et al., Nucl. Fusion **42** (2002) 725.

[531] Fundamenski, W., et al., Plasma Phys. and Contr. Fusion **44** (2002) 761.

[532] Hassanein, A., and Konkashbaev, I., J. Nucl. Mater. **273** (1999) 326.

[533] Hassanein, A., Fusion Eng. Des. **60** (2002) 527.

[534] Wuerz, H., et al., Fusion Sci. and Tech. **40** (2001) 191.

[535] Hassanein, A., and Konkashbaev, I., J. Nucl. Mater. **313–316** (2003) 664.

[536] Pestchanyi, S.E., et al., Proc. 30th EPS Conference on Contr. Fusion and Plasma Phys., St. Petersburg, Russia, Vol. 27A, 2003, P-2.164.

[537] Adams, M. L., et al., J. Quant. Spectrosc. Radiat. Transf. **71** (2001)117.

[538] Lovegrove, T., et al., Proc. 22nd Eur. Phys. Soc. Conf., Bournemouth, UK, ECA Vol. 19C III-301 (1995).

[539] Reiter, D., et al., J. Nucl. Mater. **313-316** (2003) 845.

[540] Krasheninnikov, S. I., et al., Contrib. Plasma Phys. **28** (1988) 443.

[541] Behringer, K., "Escape factors for line emission and population calculation", MPI-Garching Report, IPP 10/11 (1998).

[542] Marchand, R., et al., Phys. Fluids B **4** (1992) 924.

[543] Wan, A. S., et al., J. Nucl. Mater. **220-222** (1995) 1102.

[544] Adams, M. L., et al., Contrib. Plasma Phys. **42** (2002) 395.

[545] Scott, H.A., and Adams, L.A., Contrib. Plasma Phys **44** (2004) 51.

[546] Reiter, D., et al., "The EIRENE code", http://www.eirene.de, (2004).

[547] Adams, M.L., and Scott, H. A., Contrib. Plasma Phys. **44** (2004) 262.

[548] Reiter, D., et al., Fusion Sci. Tech. **47** (2005) 172.

[549] Fantz, U., et al., J. Nucl. Mater. **266-269** (1999) 490.

[550] Sawada, K., and Fujimoto, T., J. Appl. Phys. **78** (1995) 2913.

[551] Pigarov, A.Yu., Physica Scripta **T96** (2002) 16.

[552] Kubo, H., et al., J. Nucl. Mater. **337–339** (2005) 161.

[553] Pitts, R.A., et al., in Fusion Energy 2000 (Proc. 18th Int. Conf. Sorrento, 2000) (Vienna: IAEA) CD-ROM file EXP4/23 and http://www.iaea.org/programmes/ripc/physics/fec2000/html/node1.htm.

[554] Wischmeier, M., et al., Contrib. Plasma Phys. **44** (2004) 268.

[555] Janev, R.K., Kato, T., and Wang, J.G., Phys. Plasmas **7** (2000) 4364.

[556] Janev, R.K., et al., "Collision Processes in Low-Temperature Hydrogen Plasmas", Report Forschungszentrum Jülich, JUEL 4105, (Dec. 2003).

[557] Lisgo, S., et al., J. Nucl. Mater. **313-316** (2003) 1089.

[558] Cambe, A., et al., J. Nucl. Mater. **313-316** (2003) 364.

[559] Kirschner, A., et al., Proc. 30th EPS Conf. on Contr. Fusion and Plasma Phys., St. Petersburg, Russia, 2003, ECA Vol. 27A, P-3.196 (2003).

[560] Ohya, K., et al., J. Nucl. Mater. **313-316** (2003) 568.

[561] Hyodo, I., et al., J. Nucl. Mater. **313-316** (2003) 1183.

[562] Stangeby, P.C., and Elder, J.D., "Simulating Net Erosion Near the Inside Target of JET Using the DIVIMP Code", Tritium Retention Meeting, JET, 10 March 1999.

[563] Coster, D.P., et al., J. Nucl. Mater. **313–316** (2003) 868.

[564] Alman, D.A., et al., Phys. Plasmas **7** (2000) 1421.

[565] Janev, R.K., Wang, J.G., and Kato, T., NIFS-DATA-64 (2001).

[566] Janev, R.K., and Reiter, D., J. Nucl. Mater. **313-316** (2003) 1202.

[567] Traskelin, P., et al., J. Nucl. Mater. **313-316** (2003) 52.

[568] Salonen, E., et al., J. Nucl. Mater. **313-316** (2003) 404.

[569] Pappas, D., "Study of Molybdenum Sources and Screening in the Alcator C- mod Tokamak", PHD Thesis, MIT (2000), published as PSFC Report PFC/RR-00-6.

[570] Kawakami, R., and Ohya, K., J. Nucl. Mater. **313-316** (2003) 107.

[571] Strachan, J.D., et al., Nucl. Fusion **44** (2004) 772.

[572] Stangeby, P.C., et al., J. Nucl. Mater. **313-316** (2003) 883.

[573] Coster, D.P., et al., Plasma Phys. Control. Fusion **44** (2002) 979.

[574] Wootton, A.J., et al., Phys. Fluids B **2** (1990) 2879.

[575] Hidalgo, C., et al., Fusion Energy 1996 (Proc. 16th Int. Conf. Montreal, 1996), IAEA, Vienna 1997, Vol. 1, p. 617.

[576] Antar, G.Y., et al., Phys. Plasmas **8** (2001) 1612.

[577] Connor, J.W., and Helander, P., Plasma Phys. Control. Fusion **41** (1999) 251.

[578] Nedospasov, A.V., et al., Sov. J. Plasma Phys. **15** (1989) 659.

[579] Garbet, X., et al., Nucl. Fusion **31** (1991) 967.

[580] Beyer, P., and Spatschek, K.H., Phys. Plasmas **3** (1996) 995.

[581] Xu, X.Q., and Cohen, R.H., Contrib. Plasma Phys. **36** (1998) 158.

[582] Berk, H.L., et al., Phys. Fluids B **5** (1991) 1336.

[583] Ribeiro, T., and Scott, B., Plasma Phys. and Control. Fusion **47** (2005) 1657.

[584] Krasheninnikov, S.I., et al., in Fusion Energy 22002 (Proc. 19th Int. Conf. Lyon, 2002) (Vienna: IAEA) CD-ROM file TH/4-1 and http://www.iaea.org/programmes/ripc/physics/fec2002/html/fec2002.htm.

[585] Xu, X.Q., et al., Nucl. Fusion **40** (2000) 731.

[586] Xu, X.Q., et al., Contrib. Plasma Phys. **44** (2004) 105.

[587] McKee, G.R., et al., Phys. Plasmas **10** (2003) 1712.

[588] Mazurenko, A., et al., Phys. Rev. Lett., **89** (2002) 225004-1.

[589] Rognlien, T.D., et al., Contrib. Plasma Phys. **44** (2004) 188.

[590] Xu, X.Q., et al., Phys. Plasmas **10** (2003) 1773.

[591] Sarazin, Y., and Ghendrih, Ph., Phys. Plasmas **5** (1998) 4214.

[592] Garbet, X., et al., Nucl. Fusion **39** (1999) 2063.

[593] Bian, N., et al., Phys. Plasmas **43** (2003) 1382.

[594] Ghendrih, Ph., et al., Nucl. Fusion **43** (2003)1013.

[595] Garcia, O., et al., Phys. Rev. Lett. **92** (2004) 165003.

[596] Sarazin, Y., et al., Phys. Plasmas **7** (2000) 1085.

[597] Garbet, X., et al., in Plasma Physics and Controllled Nuclear Fusion Research 1988 (Proc. 12th. Int. Conf. Nice, 1988), Vol. 2, p.163, IAEA, Vienna (1989).

[598] Sarazin, Y., et al., J. Nucl. Mater. **313-316** (2003) 796.

[599] Falchetto, G.L., et al., in Fusion Energy 2004 (Proc. 20th Int. Conf. Vilamoura, 2004) (Vienna: IAEA) CD-ROM file TH/1-3Rd and http://www-naweb.iaea.org/napc/physics/fec/fec2004/datasets/index.html.

[600] Lin, Z., et al., Science **281** (1998) 1835.

[601] Diamond, P.H., and Hahm, T.S., Phys. Plasmas **2** (1995) 3640.

[602] Ghendrih, Ph., et al., in Fusion Energy 2004 (Proc. 20th Int. Conf. Vilamoura, 2004) (Vienna: IAEA) CD-ROM file TH/1-3Ra and http://www-naweb.iaea.org/napc/physics/fec/fec2004/datasets/index.html.

[603] Ghendrih, Ph., et al., J. Nucl. Mater. **337–339** (2005) 347.

[604] Aydemir, A.Y., Phys. Plasmas **12** (2005) 062503.

[605] Peng, Y.K.M., et al., in Plasma Physics and Controlled Nuclear Fuusion Research 1994 (Proc. 15th Int. Conf. Seville, 1994), Vol. 2, p.643, IAEA, Vienna (1995).

[606] Hidalgo, C., Euratom-CIEMAT association, private communication, 2003.